Kinematic Design of 6-DOF Decoupled Parallel Manipulators

Jin Yan

School of Mechanical & Aerospace Engineering

A thesis submitted to the Nanyang Technological University
in fulfilment of the requirement for the degree of
Doctor of Philosophy

2007

Acknowledgment

I am very grateful to my advisor, Professor Chen I-Ming, for his continuous interest, intellectual guidance, unlimited patience and constant encouragement during this research. His creative vision and broad knowledge play an important part in the fulfillment of this work.

I would like to thank my senior, Dr. Yang Guilin, for his constructive advice given to me. Dr Yang is always there to give me a helping hand and share with me his ideas in problem solving.

Deepest gratitude is expressed to my parents and my wife who are constantly giving me their unconditional love and care. Deepest gratitude is also extended to my younger brother, my parents in-law and my grand parents.

I would like to thank Prof. Lye Sun Woh, Prof. Gerald Seet, and Prof. Li Qing, for their valuable comments during my confirmation examination. I would also like to thank Prof. Yeo Song Huat, for his valuable advice and encouragement.

I would also like to thank Prof. Gerald Seet, Mr. Lim Eng Cheng, Ms. Agnes Tan, Mr. Yow Kim San and Ms. Toh Yen Mei for providing me an excellent research environment at the Robotics Research Center (RRC). In addition, I would like to extend my gratitude to my friends, namely Dr. Chen Weihai, Dr. Xing Shusong, Dr. Anjan Kumar Dash, Dr. Theingi, Dr. Pham Huy Hoang, Mr. Lim Chee Kian, Mr. Yan Liang, Mr. Pham Cong Bang, Mr. Mustafa Shabbir Kurbanhusen, Ms. Tang Xueyan, Mr. Edwin HL Ho, Mr. Teo Tat Joo Daniel, Ms. Wang Xin, Ms. Wang Pin, etc.

Lastly, I would also like to acknowledge the financial support that I have received during the research from Nanyang Technological University. This project is partially supported by Ministry of Education, Singapore, under ARC project RG6/02.

Abstract

Parallel manipulators (PMs) have many advantages comparing with the serial counterparts, such as high payload capacity, high speed and acceleration, high accuracy and high stiffness. However, usual PMs, like the Stewart platform, suffer from the problems of difficult forward kinematics, coupled motion, and small workspace so as to make motion planning and control difficult in applications. Kinematically decoupled PMs are the best candidates to cope with these drawbacks while keeping the advantages of general PMs. This thesis focuses on issues related to kinematic design of 6-DOF decoupled PMs, including structure synthesis, displacement and singularity models, workspace design, dimension optimization, statics and stiffness models, and constraint errors. The main contributions of this thesis lie in the design methodology on structure synthesis, workspace determination, and constraint error evaluation for decoupled PMs. The decoupled PMs are classified according to the motion of the end-effector. A systematic approach is proposed for structure synthesis of two classes of 6-DOF decoupled PMs. As a result, the two classes of 6-DOF decoupled PMs are obtained, in which seven structures are new. A finite-partition approach for parametrical and proportional partition of the rigid motion group $SE(3)$ is introduced based on its topology. The partition approach makes the numerical computation of the 6-D manipulator workspace possible. Based on this finite-partition approach, two global performance indices and three optimal points are defined on the 6-D workspace for design optimization and task realization of PMs. Several design examples show that this approach is effective. Due to the special geometric requirements on the joint arrangement for decoupled motion, a method to evaluate the effect of constraint errors on the decoupling characteristics of PMs is proposed. Through this approach, the importance of design constraints can be objectively described and used as guidelines during fabrication and assembly. In summary, important aspects of decoupled PM design have been established. The design methodology is illustrated by case studies on the design of the two classes of 6-DOF decoupled PMs.

Contents

List of Figures

List of Tables

List of Symbols

J_x	Forward Jacobian matrix
J_θ	Inverse Jacobian matrix
θ_{ij}	Displacement of the j^{th} joint of the i^{th}limb
$\hat{\mathbf{\$}}_{ij}$	Unit screw of the j^{th} joint of the i^{th} limb
$\boldsymbol{s}_{ij}$	Direction vector of $\hat{\mathbf{\$}}_{ij}$
$\hat{\mathbf{\$}}_{O'}$	Instantaneous twist of the end-effector
$\hat{\mathbf{\$}}_{irj}$	The j^{th} reciprocal screw of the i^{th} limb
$T_{OO'}$	End-effector pose, $T_{OO'} \in SE(3)$
$SO(3)$	Special orthogonal group
$SE(3)$	Special Euclidean group
W	Six dimensional workspace
W_p	Reachable position workspace, $W_p \subseteq \Re^3$
W_R	Reachable orientation workspace, $W_R \subseteq SO(3)$
$\boldsymbol{p}$	Position vector
$W_R(\boldsymbol{p})$	Orientation workspace at position $\boldsymbol{p}$
$W_p(R)$	Position workspace under orientation R
W_C	the position workspace envelope, $W_C \subset \mathbb{R}^3$ and $W_C \supseteq W_p$
m	Number of division along one dimension of the cube homomorphic to $\mathbb{R}^3$
n	Number of hemispherical shells dividing the solid hemisphere
$\sigma_{min}(J)$	Minimum eigenvalue of the Jacobian matrix
$\sigma_{max}(J)$	Maximum eigenvalue of the Jacobian matrix
C_I	Condition index
$\boldsymbol{p}_G$	Global optimal position, $\boldsymbol{p}_G = \{\boldsymbol{p} : max\ W_R(\boldsymbol{p}) \subseteq SO(3)\}$
R_G	Global optimal orientation, $R_G = \{R : max\ W_p(R) \subseteq \Re^3\}$
W_r	Ratio of workspace volume to the whole calculated space volume
t	Time

$\Delta\boldsymbol{\theta}$	Infinitesimal actuator input displacement
$\Delta\boldsymbol{X}$	Infinitesimal end-effector output displacement
$\boldsymbol{F}$	Force vector of end-effector outputs
$\boldsymbol{\tau}$	Force (or torque) vector of actuator inputs
ρ_{max}	Stroke of linear actuators of SA-PM
ρ_{pmax}	Passive prismatic joint distant end
ρ_{pmin}	Passive prismatic joint close end
ρ_a	Stroke of linear actuators of the 3RPPS PM
ν	Ratio of the moving platform radius and base radius
ξ	Ratio of the capability of rotary actuator to linear actuator
χ	Spring constants related to actuators, $\chi = diag[k_1, k_2, \ldots, k_n]$
K	Stiffness matrix
K_r	Torsional stiffness matrix
K_l	Translational stiffness matrix
$\delta\hat{t}_i$	Error matrix, $\delta\hat{t}_i \in se(3)$
δt_i	A twist representing the geometry errors
$\boldsymbol{\delta p}$	Position error
$\hat{\mathbf{\$}}_i^n$	Twist to represent nominal pose of the i^{th} joint axis

List of Abbreviations

PM	Parallel manipulator
DOF	Degree of freedom
GD	Group decoupling
GCI	Global condition index
GIP	Global isotropy point
ZP	Zero pitch
IP	Infinite pitch
3T3R	3-DOF translation and 3-DOF rotation
3P3S	3-DOF planar motion and 3-DOF spatial motion
SA-PM	Selectively actuated parallel manipulator
CL	Characteristic length

Chapter 1

Introduction

1.1 Motivation

A parallel manipulator (PM) is a closed-loop kinematic chain mechanism whose end-effector is linked to the base by several independent kinematic chains. Over the past two decades, parallel manipulators have attracted a lot of interest from university to industry. Generally speaking, the parallel manipulators may give higher payload capacity, higher speed and acceleration, higher static and dynamic accuracy and higher stiffness than what is possible with the industrial robots of serial structure used today.

The earliest parallel manipulator is probably the Gough platform invented by Gough in 1947, which allows the positioning and the orientation of a moving platform so as to test tire wear and tear (Fig. 1.1). Stewart [99] designed a parallel manipulator (Fig. 1.2) for use as a flight simulator in 1965. The researchers in the field of mechanisms and robotics were attracted by the parallel manipulators in 1980s. Till now, the commercialized PMs are mainly based on three types of parallel manipulator structures, i.e., Stewart platform structure [99], Delta robot structure [17] and Tricept robot structure [88]. Based on the Stewart platform structure, Hexel Corporation has developed the R series robots (Fig. 1.3(a)) for bio-medical applications, and P series robots (Fig. 1.3(b)) for industrial applications, such as welding, deburring and milling.

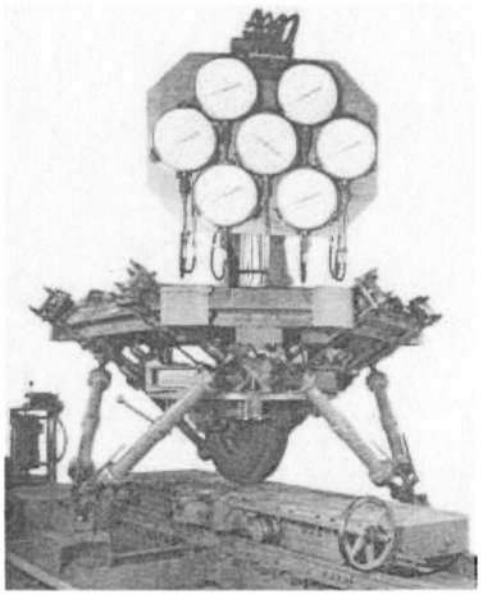

Figure 1.1: Gough platform (adapted from http://www.parallemic.org/Reviews/Review007.html)

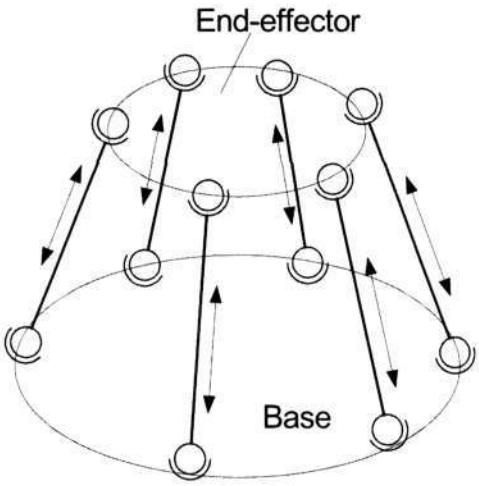

Figure 1.2: Stewart platform

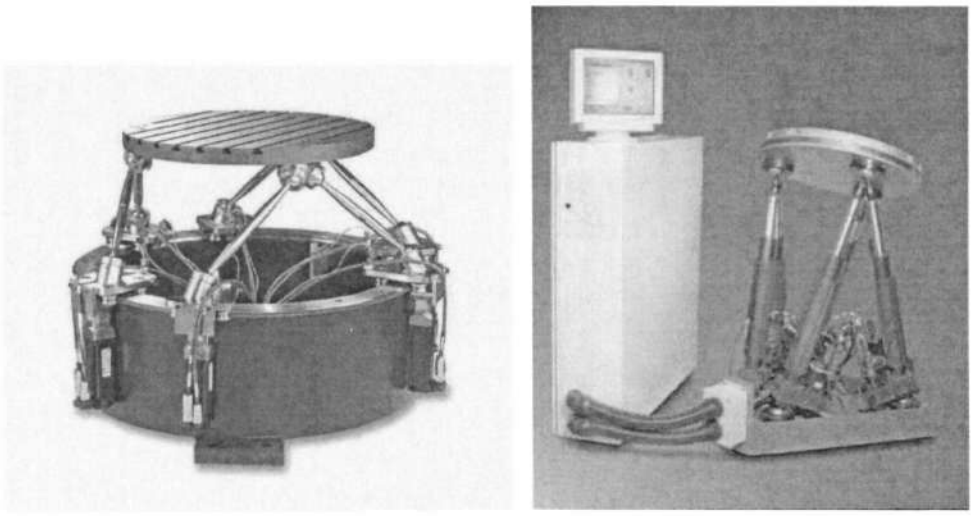

(a) R series

(b) P series

Figure 1.3: Applications of the Stewart platform by Hexel Corporation (adapted from Hexel Corporation)

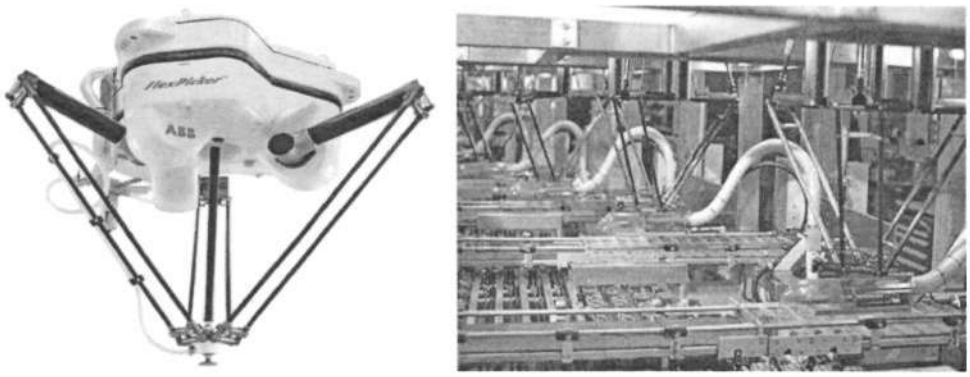

(a) IRB340 Flex Picker (adapted from ABB Flexible Automation)

(b) Demaurex's Line-Placer installation (adapted from Demaurex)

Figure 1.4: Applications of the Delta robot

In 1999, the ABB Flexible Automation introduced the IRB340 Flex Picker as shown in Fig. 1.4(a). The Flex Picker is an extension work on Delta Robots [17]. It is equipped with an integrated vacuum system capable of rapid pick-and-place of objects. There are many applications related to Delta robots in the industry and one of them is used as Line-Placer as shown in Fig. 1.4(b). SMT Tricept Corporation introduced the Tricept 600 series for the line assembly and manufacture of automobile (Fig. 1.5).

Other applications can be found in [1, 2, 10, 13, 22, 30, 34, 39, 40, 47, 70]. As there is only several types of parallel mechanism structures available, the attention of researchers moves to propose new types of structures [21, 30, 32, 33, 38, 58, 60, 104], and study the approaches for structure synthesis of PMs with lower mobility (less than six) recently [21, 38, 43, 60, 62, 64, 72, 103].

However, most of the PMs with lower mobility are overconstrained PMs when assembly errors are considered [78]. Therefore, these PMs cannot be assembled without joint clearance which imposes negative impacts on the accuracy of the end-effector. In addition, for PMs with less than six DOFs, kinematic errors may not even be recovered through calibration. Parenti-Castelli and Di Gregorio studied the error effects on the kinematic performance of PMs with three DOFs [35, 90], and found that some errors satisfying

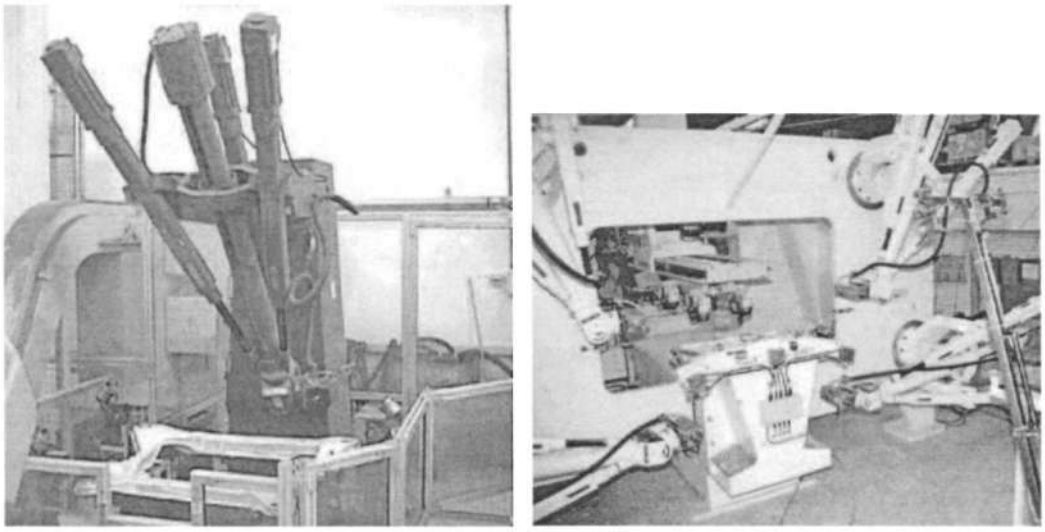

(a) Tricept 600

(b) Machining of bumpers 5 tricepts working in one cell

Figure 1.5: Applications of the Tricept robot by SMT Tricept Corporation (adapted from SMT Tricept Corporation)

the DOF requirements of the end-effector can be calibrated while other errors cannot be calibrated.

Another trend in PM design is to study these 6-DOF PMs with decoupled motion structure [5, 49, 50, 52, 54, 55, 57, 113, 115], which can overcome the problem of assembly and calibration, and simplify the kinematic analysis, motion planing and control. Usual PMs, like the Stewart platform, suffer from the disadvantages of difficult forward kinematics, coupled motion, and small workspace, so that the motion planing and control become very complicated and difficult to be implemented in real application.

Decoupled motion means that some motion DOFs are independent to the other motion DOFs. For example, 6-DOF decoupled translation and rotation means that the 3-DOF translations are independent to the 3-DOF rotations. A decoupled PM refers to a PM whose end-effector has decoupled motion, so that specific motion axes of the end-effector can be controlled by the designated actuators independently. Taking the 6-DOF decoupled PM with decoupled translation and rotation for example [55], the 3-DOF translation

is controlled by three linear actuators, and the 3-DOF rotation is controlled by three rotary actuators. In this case, the manipulator Jacobian can be reduced from a single 6×6 matrix to two 3×3 matrices. The position and orientation of the end-effector can be calculated separately. Therefore, the displacement calculation, singularity analysis, workspace evaluation, statics analysis, motion planning and control are significantly simplified. Generally speaking, the 6-DOF decoupled PMs have following advantages:

- High payload capacity, low moment of inertia, high stiffness, high speed and acceleration capacity
- Decoupled motion characteristics, selectively actuated for different tasks
- Closed-form solutions for both inverse and forward displacements
- Simplified kinematic analysis, motion planning and control scheme
- Ease for implementing calibration and compensation

In the literature, Innocenti [49] proposed a 6-DOF PM with decoupled translation and rotation, in which three links share a common ball joint so that the position of the end-effector is only controlled by these three links. Lallemand et al. [67] introduced a 6-DOF decoupled 2-Delta PM in which the external Delta robot is in charging for the translation of the end-effector, while the internal Delta robot is for controlling the orientation of the end-effector through one limb that allows free translation but no rotation. Shim et al. [98] mentioned a decoupled 3-PRPS 6-DOF PM in which the two prismatic joint of each limb are actuators. Lee and Park [71] introduced a 6-DOF decoupled PM which makes use of two PMs and a central axis. The orientation and the position of the end-effector are independently controlled by the two PMs. Comparing with the corresponding Stewart platform, the decoupled PM performs a larger workspace with less singularity. Zabalza et al. [115] proposed a 6-DOF PM which decouples the 3-DOF planar motion and the other 3-DOF spatial motion by using three modified Scott's mechanisms. Yang et al. [110]

proposed a 6-DOF 3-RPRS decoupled PM, in which the three planar motion DOFs and the other three motion DOFs are independently controlled.

Current design of decoupled PMs mainly depends on the intuition and intelligence of the designer, and there is no clear classification and systematic approach for synthesizing decoupled PMs. There could be some other novel types of decoupled parallel mechanism structures having good performance neglected. Therefore, the focus of this thesis is to address the systematic design of PMs leading to new types of decoupled PM structures, and performance evaluation of these PM structures.

1.2 Design Problems of Parallel Manipulators

Engineering design of PMs is a very broad topic. Figure 1.6 indicates the overview of the kinematic design issues for parallel manipulators discussed in this thesis. Structure synthesis is the beginning in a manipulator design. All the other design issues should be based on the parallel manipulator structure. Kinematic model is to find the relationship between the output pose of the end-effector and the input displacement of the actuators. It is the basis for various analyses of the PM, such as singularity, statics and error analyses. Singularity analysis is very important. It is usually used to determine the workspace of PMs. As a PM has limited workspace, workspace evaluation and optimization are essential to design a PM optimally. Statics and stiffness are also necessary for evaluating the statics properties of PMs, such as maximal output force and accuracy. For the decoupled PMs, constraint error evaluation are also dispensable for objectively describing the error effects so as to provide guidelines for fabrication and assembly. In this section, the current state-of-arts of these design issues are introduced.

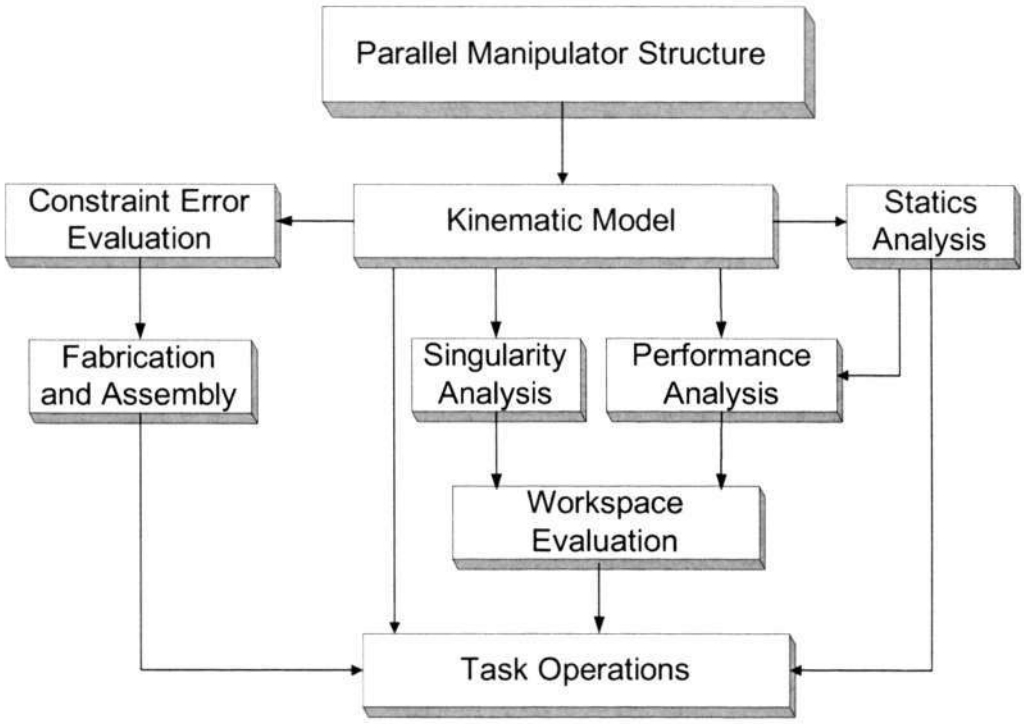

Figure 1.6: Kinematic design issues discussed in this thesis

1.2.1 Structure Synthesis

The initial step in manipulator design is structure synthesis, which is to determine the topological structure properties such as degrees of freedom (DOFs), the number and type of links, the number and type of joints, the number of independent loops, and the interconnections between links and joints. This part of the work is most difficult because it comes from the creativity of the designer and mostly depends on their intuitiveness, intelligence and experiences. Generally speaking, current parallel manipulators are designed in a case-by-case manner. It is difficult to find a generic approach to synthesize any type of manipulators. In order to reduce the complexity of type synthesis of PMs, the PMs are often classified by their end-effector mobility. In this way, some parallel manipulator with less mobility (less than 6) can be synthesized in a systematic way [21, 37, 38, 43, 62, 72]. However, there are no clear classification of decoupled PMs, and no systematic approaches for synthesizing PMs with decoupled motion.

1.2.2 Kinematic Models

With given manipulator structures, a designer needs to identify the kinematic properties of the manipulators, such as instantaneous kinematic modeling, singularity conditions, and displacement solution.

Instantaneous kinematics is to establish the relationships between the instantaneous motion of the active joints and that of the end-effector, which is necessary for analyzing the motion and control of robotic manipulators. Singularities refer to particular manipulator configurations in which the end-effector gains or losses one or more degrees of freedom. Jacobian matrix analysis is an effective approach for checking the singularities of PMs. The singularity loci will directly determine the workspace of a manipulator. Sometimes it also helps the designer to identify the isotropy characteristics of a PM.

Kinematics (displacement) analysis is to find the relationship between the position (pose) of the end-effector and the displacements of the actuators. It is the basis of workspace analysis, dimensional optimization, motion planing and control. For parallel manipulators, displacement analysis is classified into: 1) forward displacement analysis, in which it is to find the end-effector pose with given displacements of actuators, and 2) inverse displacement analysis, in which the displacements of actuators is to be found with given end-effector pose. For a serial manipulator, the forward displacement is straight forward but the inverse displacement is difficult due to multiple solutions. For the parallel manipulators, the inverse displacement is easy because it can be obtained once the platform pose is determined. And yet the forward displacement is generally very complicated as it requires solving higher order nonlinear equations.

1.2.3 Workspace Evaluation and Dimension Optimization

Workspace analysis and optimization are important in a manipulator design. As PMs have a much smaller workspace than that of a serial counterpart, the size and quality of

workspace become important performance indices. Solution to this problem is critical in the design and motion planing of the manipulator. Therefore, physical geometry parameters of the links, joints, base and the moving platform should be optimized for maximizing the workspace performance.

Determination of workspace of the general parallel manipulators is still a challenging problems, due to following reasons. 1) As the complete workspace of a 6-DOF manipulator is embedded into a 6-dimensional space, there is no possible way to represent it graphically in a human-readable way. Most of the literatures only considered the 3-D workspaces, which are subspaces of the complete 6-D workspace. Therefore, the global properties of the 6-D complete workspace cannot be evaluated properly. 2) There is no suitable way for us to integrate the 6-D workspace volume along its boundary, as the forward kinematic problem is difficult to obtaine in closed-form. The 3-D reachable workspace volume is thus often used to describe the workspace in the literature. 3) Restricted by the workspace computation, to our knowledge, there are no global performance indices for the optimal design in the complete 6-D workspace. 4) The workspace depends on constraints introduced by joint-angle limitations, link-length limitations, and leg-interference. Most of the literature does not consider the actual physical constraints in the workspace analysis.

1.2.4 Statics and Stiffness Modeling

Statics force analysis is of practical importance in evaluating the force transmission through the manipulator joints and links. For a manipulator design, it is essential to specify the peak force and moments that the end-effector can perform, which is an important measure to select a machine for some certain tasks. Stiffness is an important index to evaluate robot performance for a specific task in which the end-effector exerts some force and moments on its environment. This force and moments will lead to the deflection of the mechanism so that the end-effector will be deflected away from the desired pose. Therefore, the stiffness will give an immediate impact to the position accuracy of

a manipulator. Some control algorithms make use of the stiffness characteristics for accurately controlling a robot manipulator. The overall stiffness of a manipulator depends on several factors, including the mechanical structure, the dimensions and the materials of the links, the actuators and the controller. Especially when the links or joints have more compliance, the stiffness of the manipulator becomes the major concern of the accuracy. Computation time is critical in control, so that the simple stiffness model is usually required.

1.2.5 Error Evaluation

Parallel manipulators featuring decoupled motion usually need to satisfy some critical geometrical constraints, for example, the axes of revolute (R) joints intersecting at one common point and the moving direction of the passive prismatic (P) joint being perpendicular to the related actuator axis [55], the axis of the rotary actuator aligning with the moving direction of the prismatic actuator in each limb, and the axes of passive R-joint and rotary actuator being parallel [113]. When manufacturing tolerances and assembly errors are considered, the actual manipulator motion may not be decoupled as stated in the design. Although these manufacturing errors may be compensated through the kinematic calibration [86, 107, 111, 116], it is still not possible to know the effects of the errors on the manipulator kinematics. Hence, it is difficult for engineers to identify the source of the geometrical errors and minimize them in the initial manufacturing stage. For PMs with less than six DOFs, kinematic errors may not even be recovered through calibration.

1.3 Proposed Approaches

To reduce the complexity in the generic problem of type synthesis of 6-DOF decoupled PMs, the decoupled PMs are classified, and the concept of *Group Decoupling* (GD) is

introduced. An idea of sharing sub-chain composed by only passive joints is disclosed. A systematic approach based on this idea is proposed for structure synthesis of 3-limb symmetrical 6-DOF PMs with 3-3 decoupled motion, i.e., 3-DOF translation and 3-DOF rotation are independently controlled, or 3-DOF planner motion and the other 3-DOF spatial motion are independently controlled. A search space including serial limb chains with at least one zero-pitch wrench is developed, which reduces great effort in type synthesis. Two classes of 3-3 decoupled parallel manipulators are obtained, in which seven novel structures are obtained.

A finite-partition approach of the rigid motion group $SE(3)$ is proposed for workspace evaluation. It is known that the Special Orthogonal group $SO(3)$ is homeomorphic to a solid ball D^3 with antipodal points identified while the geometry of $\mathbb{R}^3$ can be regarded as a cube. Furthermore the solid ball and the cube can be parametrically and proportionally partitioned into a number of elements. Therefore, the basis volume elements of $\mathbb{R}^3$ and $SO(3)$ can be obtained. The product of two basis volume elements of $\mathbb{R}^3$ and $SO(3)$ respectively will produce a basis volume element of $SE(3)$. By this way, the integration of the complete 6-D workspace volume is transformed into the simple summation of the basis volume elements of $SE(3)$. Based on this finite-partition method, two global performance indices, i.e., Workspace volume ratio(W_r) and Global condition index (GCI), and three optimal points, i.e., Global optimal position ($\boldsymbol{p}_G$), Global optimal orientation (R_G) and Global isotropy point (GIP), are defined in the 6-D workspace. With the help of the two indices, two dimension optimization algorithms are effectively implemented for the two classes of PMs respectively. The optimal points of the two classes of PMs are obtained. They are useful for specifying the performance of a certain design, which is illustrated by two classes of decoupled PMs in this thesis.

A new approach for analyzing the constraint error effects on decoupling characteristics of PMs is proposed. Three basic types of constraint errors are identified. Through this approach, the dominating errors and the guidelines for design, fabrication and assembly

can be obtained. In addition, this approach can also be used for those PMs with less mobility (less than six DOFs).

The remaining chapters of this thesis are organized as follows. Chapter 2 presents the structure synthesis of 6-DOF 3-3 decoupled parallel manipulators. Chapter 3 addresses instantaneous kinematics and singularity analysis. Chapter 4 gives the displacement algorithm for the 3-3 decoupled PMs. Chapter 5 addresses workspace evaluation through a finite-partition approach of $SE(3)$. Chapter 6 address statics and stiffness analysis. Chapter 7 study constraint error. Chapter 8 concludes the work.

Chapter 2

Structure Synthesis

Generally speaking, designing a mechanism is a two-step process, i.e., structure synthesis and dimensional synthesis [81]. Structure synthesis refers to the determination of structural properties such as degrees of freedom, the number and type of links, the number and type of joints, the number of independent loops, the nature of motion (planar and spatial), and the interconnections between links and joints. This step is difficult because it comes from the originality and mostly depends on the experience and intelligence of the designer. Dimensional synthesis is to determine the parameters of the mechanism to satisfy the performance requirements based on the given mechanism structure.

In this chapter, a systematic approach is proposed to synthesize symmetrical non-redundant 6-DOF PMs with 3-3 decoupled motion, i.e., 3-DOF translation and 3-DOF rotation are independently controlled, or 3-DOF planner motion and the other 3-DOF spatial motion are independently controlled. In this approach, the end-effector mobility requirements are analyzed first to obtain the wrench constraints associated with each limb kinematic chain based on the decoupled motion requirements. Then the limb sub-chain with only passive joints are enumerated based on a search space which includes all the limbs with at least one zero-pitch wrench. The type and geometry of actuators are determined subsequently by using the line geometry method [21, 43, 62]. An exhaustive enumeration of 3-3 decoupled 6-DOF PMs are obtained.

This chapter is organized as follows. Section 2.1 introduced the background on the structure synthesis of PMs. Section 2.3 studies the type synthesis of limbs with at least one zero-pitch wrench in finite motion. The concept of Group Decoupling (GD) is proposed in Section 2.4. A procedure for synthesizing 3-limb symmetrical non-redundant 6-DOF PMs with 3-3 GD is proposed in Section 2.5. Section 2.6 introduces the structure synthesis of 6-DOF PMs with decoupled translation and rotation. Section 2.7 studies the structure synthesis of 6-DOF PMs with decoupled 3-DOF planner motion and the other 3-DOF spatial motion.

2.1 Introduction

In the literature, most of the PMs have identical limbs to simplify the design and fabrication [30, 33, 55, 67, 85, 105, 115]. Tsai introduced an enumeration scheme based on the Grübler criterion to guide synthesis of PMs with 2 to 6 DOFs [103]. However, this approach can only synthesize PMs with certain number of DOFs but not PMs with certain motion. For the structure synthesis of PMs with lower DOFs, there are two major methods: constraint synthesis approach [20, 21, 43, 44, 62, 63] based on screw theory, and Lie sub-group approach [37, 38, 72] based on the algebraic properties of a Lie group of the Euclidean displacement set.

In screw-based method [43], the standard base of the mechanism twist system is obtained according to the mobility requirement of the end-effector, and then is treated as the standard base of the limb twist system. Subsequently, some other necessary twists are added to obtain the limb twist system. The process of adding other twists mainly depends on the experiences of the designer. Then, all the limbs are connected with the base and the mobile platform according to the geometrical conditions. Lastly, it requires to check if the PMs can work in finite motion as this approach is based on the instantaneous kinematics. Hence, some PMs obtained in this manner may be infeasible for finite motion.

In Lie subset method [37], a set of operators is used to describe all possible finite displacements, and each kind of motion is represented by a set of operators. A mechanical bond is represented by the set of allowed displacements of one body with respect to the other. A serial arrangement of kinematic pairs becomes the composition of mechanical bonds, and a parallel arrangement of kinematic pairs is represented by the intersection of mechanical bonds. The first step in type synthesis is to get a mechanical generator of a limb according to the motion characteristics of the end-effector. Second is to analysis the mechanical generator to obtain a feasible configuration for a limb. Third is to combine several limbs to form the PMs. And last, checking finite motion on the mechanism is required. Similar to the screw-based method, the second step of this approach very much depends on the experiences of the designer.

2.2 Concepts of Screw, Twist and Wrench

A screw is associated with a line in the three-dimensional space and a scalar called pitch, and has the form as

$$\$ = \begin{bmatrix} \boldsymbol{s}, \\ \boldsymbol{r} \times \boldsymbol{s} + \lambda \boldsymbol{s} \end{bmatrix}, \tag{2.1}$$

where $\boldsymbol{s}$ is a 3×1 vector pointing the direction of the screw axis. $\boldsymbol{r}$ is the position vector is the position vector of any point on the screw axis with respect to a reference frame, and λ is the pitch of the screw. Specially, the screw is called a unit screw when $\boldsymbol{s}$ is a unit vector. According to Chasles's theorem: Any displacement of a rigid body can be effected by a single rotation about a unique axis combined with a unique translation parallel to that axis, so any displacement can be described as a "screw displacement", where the unique rotation axis, which is also the translation direction, is referred to as the *screw axis* of the displacement. Screw theory is a way to study velocities and forces in three-dimensional space, combining both rotational and translational parts. When a screw is used to describe the motion state of a rigid body, it is often called a *twist*. When a screw is used to describe the force or moment, it is called a *wrench*.

A screw is called a zero-pitch screw if its pitch equals to zero. It is defined as

$$\$ = \begin{bmatrix} \boldsymbol{s} \\ \boldsymbol{r} \times \boldsymbol{s} \end{bmatrix}. \tag{2.2}$$

It represents pure rotation in a twist motion or pure force in a wrench action and is associated with a revolute joint.

A screw is called infinite-pitch screw if its pitch is an infinity. The screw is defined as

$$\$ = \begin{bmatrix} 0 \\ \boldsymbol{s} \end{bmatrix}. \tag{2.3}$$

It represents pure translation in a twist motion or pure moment in a wrench action and is associated with a prismatic joint whose joint axis direction is in $\boldsymbol{s}$.

Two screws $\$_1=[\boldsymbol{s_1}, \boldsymbol{u_1}]^T$ and $\$_2=[\boldsymbol{s_2}, \boldsymbol{u_2}]^T$ are said to be reciprocal if we have

$$\boldsymbol{s_1} \cdot \boldsymbol{u_2} + \boldsymbol{s_2} \cdot \boldsymbol{u_1} = 0 \tag{2.4}$$

Its physical interpretation is the rate of work done by a wrench $\$_1$ acting on a rigid body having a twist $\$_2$ motion vanishes.

A screw system is a set of linear combination of independent screws. The order of a screw system, n_s, is equal to the number of basis (independent) screws in the system. Generally speaking, a serial chain with n_s revolute joints forms a n_s-system in finite motion if all the joints in their initial position are linear independent. An m_s order screw system is associated with a reciprocal $(6 - m_s)$ screw system. The twist system of a kinematic connection represents all motions permitted by that connection in a given position. The wrench system of the connection represents all constraints that can be transmitted by the connection. The twist system and the wrench system of the connection are uniquely related by reciprocity. For a parallel manipulator, the end-effector is constrained by several limbs, i.e., its DOF is determined by the combination of all the contact wrenches. Hence, the combination of all the wrench systems under different geometrical conditions may result in different kinematic DOF of the end-effector.

2.3 Type Synthesis of Limbs with at least One Zero-Pitch Wrench in Finite Motion

As Lee et al. mentioned that the wrenches associated with each limb constraining the end-effector are mostly of zero-pitch (ZP) [69]. In other words, those limbs with ZP wrench (constraint) are very useful for synthesizing PMs. In this section, the concept that the geometrical relationship between two mutually reciprocal screws can be held in finite motion is applied to synthesize serial limb chains with at least one ZP wrench in finite motion. Tsai has formulated the geometrical relationship between the screws and reciprocal screws associated with some kinematic pairs as follows [102].

- If two ZP screws are reciprocal, they must be in-parallel or intersecting to each other.
- If a ZP screw and a infinite pitch (IP) screw are mutually reciprocal, they must be perpendicular to each other.

Based on the line geometry, limb types with at least one ZP reciprocal screw in finite motion are constructed by increasing the number of kinematic pairs one by one, as shown in Fig. 2.1. In this figure, only rotary (R) and prismatic (P) joints are considered because any other types of joints can be regarded as the combination of these two joints. Each line represents a screw associated with an R-joint or a P-joint. In order to avoid redundancy, all the screws associated with each pair in a limb are independent in finite motion. Note that $\bar{\mathrm{R}}$ represents one of the intersecting R-joints, and $\underline{\mathrm{R}}$ represents one of the parallel R-joints. Other geometrical conditions are described in the figure. In order to meet these geometrical conditions in finite motion, the kinematic pairs associated with these screws with certain geometrical requirements must be adjacent.

Type		Line geometry	Pose of at least one zero-pitch reciprocal screw
2R	a	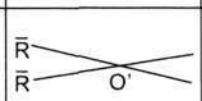	Passing through point O' or in the plane determined by the two Rs
	b	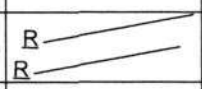	Intersecting or parallel to both
	c	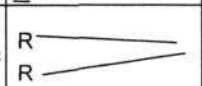	Intersecting one and parallel to the other, or intersecting both
3R	a	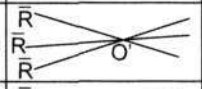	Passing through the point O'
	b	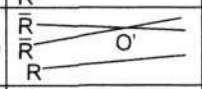	Passing through the point O' and parallel to R
	c	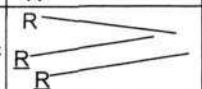	Parallel to R and intersecting with R
	d		Parallel to R
4R	a	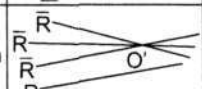	Passing through the point O' and parallel to R
	b	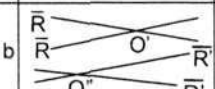	Passing through the two points O' and O"
	c	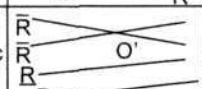	Passing through the point O' and parallel to R
	d	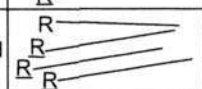	Parallel to R and intersecting R
5R	a	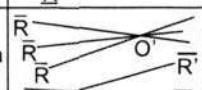	Passing through the two points O' and O"
	b	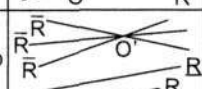	Passing through the point O' and parallel to R
	c	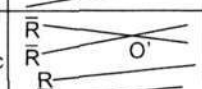	Passing through the point O' and parallel to R

Type		Line geometry	Other geometrical conditions	Pose of at least one zero-pitch reciprocal screw
1R1P	a			Perpendicular to P and intersecting R
	b	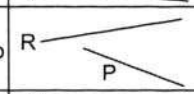	P and R perpendicular	Perpendicular to P and intersecting R, or parallel to R
2P				Perpendicular to the two Ps
2R1P	a	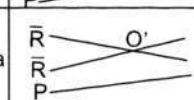		Passing through the point O' and perpendicular to P, or perpendicular to P and intersecting with two Rs
	b	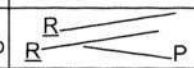	P and R perpendicular	Parallel to R
	c	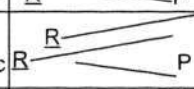		Perpendicular to P and intersecting with the two R
2R2P	a	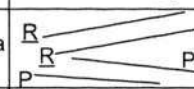	Two Ps perpendicular to R	Parallel to R
	b	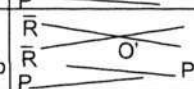		Perpendicular to the two Ps and passing through point O'
3R1P	a		P and R perpendicular	Parallel to R and intersecting to R
	b	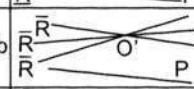		Perpendicular to P and passing through point O'
	c	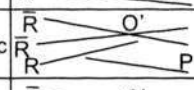	P and R perpendicular	Parallel to R and passing through point O'
	d	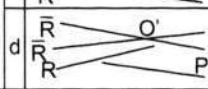		Passing through point O' and intersecting to R and perpendicular to P
3R2P	a	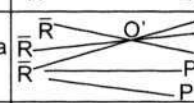		Perpendicular to the two Ps and passing through point O'
	b	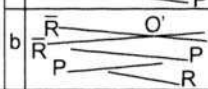	Two Ps perpendicular to R	Parallel to R and passing through point O'
4R1P	a	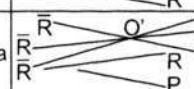	P and R perpendicular	Parallel to R and passing through point O'
	b	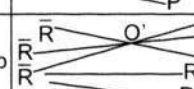		Passing through point O' and intersecting to R and perpendicular to P
	c	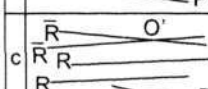	P and R perpendicular	Parallel to R and passing through point O'

Figure 2.1: Limb types with at least one zero-pitch reciprocal screw

2.4 Concept of Group Decoupling

Jin and Yang [50] classified the kinematic decoupling into two types, i.e., complete coupling (each independent output is controlled by only one input) and partial decoupling (neither complete decoupling nor complete coupling). However, the definition of partial decoupling is too broad and almost all decoupled PMs can be classified in this category of PMs. Here, a new classification method for kinematically decoupled PMs is proposed. Taking 6-DOF PMs for example, let x, y and z represent the output position (translation axis) of the end-effector in Cartesian coordinate, α, β and γ represent the output orientation (rotation axis) of the end-effector about the x, y and z axes respectively, and θ_1, θ_2, θ_3, θ_4, θ_5 and θ_6 are the six input displacements of actuators, the classification is defined as follows.

- **Complete Coupling**: Complete coupling means that each of the output axes has contribution from all input axes. The kinematic relationships between input and output variables can be written as

$$(x, y, z, \alpha, \beta, \gamma) = f(\theta_1, \theta_2, \theta_3, \theta_4, \theta_5, \theta_6). \tag{2.5}$$

- **Group Decoupling (GD)**: Group decoupling means that the 6-DOF output motion of the end-effector can be divided into two or more motion groups (such as 1-5, 2-4, 3-3 in Table 2.1), and the different motion groups are controlled by different actuators following certain order. Table 2.1 shows the different types of GD. Note that x, y and z in this table are set to represent a position, and α, β, and γ are set to represent an orientation. Taking a 3-3 GD PM with decoupled translation and rotation for example, the kinematic relationships between outputs and inputs can be written as

$$\begin{cases} (\alpha, \beta, \gamma) = f(\theta_1, \theta_2, \theta_3) \\ (x, y, z) = g(\theta_1, \theta_2, \theta_3, \theta_4, \theta_5, \theta_6) \end{cases}. \tag{2.6}$$

Equation (2.6) shows that the 3-DOF rotations are determined by three actuators

Table 2.1: Enumeration of motion groups of decoupled parallel manipulators

Type	Groups
1-5	$(x),\ (y,\ z,\ \alpha,\ \beta,\ \gamma)$
	$(\alpha),\ (x,\ y,\ z,\ \beta,\ \gamma)$
2-4	$(x,\ y),\ (z,\ \alpha,\ \beta,\ \gamma)$
	$(\alpha,\ \beta),\ (x,\ y,\ z,\ \gamma)$
	$(x,\ \alpha),\ (y,\ z,\ \beta,\ \gamma)$
3-3	$(x,\ y,\ z),\ (\alpha,\ \beta,\ \gamma)$
	$(x,\ y,\ \alpha),\ (z,\ \beta,\ \gamma)$
1-2-3	$(x),\ (y,\ z),\ (\alpha,\ \beta,\ \gamma)$
	$(\alpha),\ (\beta,\ \gamma),\ (x,\ y,\ z)$
	$(x),\ (\alpha,\ \beta),\ (y,\ z,\ \gamma)$
	$(\alpha),\ (x,\ y),\ (z,\ \beta,\ \gamma)$
1-1-1-3	$(x),\ (y),\ (z),\ (\alpha,\ \beta,\ \gamma)$
	$(\alpha),\ (\beta),\ (\gamma),\ (x,\ y,\ z)$
	$(x),\ (\alpha),\ (\beta),\ (y,\ z,\ \gamma)$
	$(\alpha),\ (x),\ (y),\ (z,\ \beta,\ \gamma)$
2-2-2	$(x,\ \alpha),\ (y,\ \beta),\ (z,\ \gamma)$
	$(x,\ y),\ (\alpha,\ \beta),\ (z,\ \gamma)$
1-1-2-2	$(x),\ (y),\ (z\ \alpha),\ (\beta,\ \gamma)$
	$(x),\ (\alpha),\ (y,\ z),\ (\beta,\ \gamma)$
	$(x),\ (\alpha),\ (y,\ \beta),\ (z,\ \gamma)$
	$(\alpha),\ (\beta),\ (x,\ y),\ (z,\ \gamma)$
1-1-1-1-2	$(x),\ (y),\ (z)\ (\alpha),\ (\beta,\ \gamma)$
	$(x,\ y),\ (z),\ (\alpha),\ (\beta),\ (\gamma)$
	$(x,\ \alpha),\ (y),\ (z),\ (\beta),\ (\gamma)$

Note: x, y, z equivalent; $\alpha,\ \beta,\ \gamma$ equivalent

$(\theta_1,\ \theta_2,\ \theta_3)$, while the position is determined by the other three actuators $(\theta_4,\ \theta_5,\ \theta_6)$, so that motion decoupling can be obtained.

- **Complete Decoupling**: Complete decoupling means that each independent output axis is controlled by only one input axis. The kinematic relationships of a 6-DOF PMs with complete decoupling between outputs and inputs can be written as

$$\begin{cases} x = f_1(\theta_1) \\ y = f_2(\theta_2) \\ z = f_3(\theta_3) \\ \alpha = f_4(\theta_4) \\ \beta = f_5(\theta_5) \\ \gamma = f_6(\theta_6) \end{cases}. \tag{2.7}$$

In this section, we study type synthesis of 3-limb symmetrical 6-DOF PMs with 3-3 GD, in which the sub-chain with only passive joints will be shared by the two motion groups. From perspective of rigid body motion [43], the 6-DOF 3-3 GD motion can be divided in two categories, i.e., 3-DOF translation in combination with 3-DOF rotation (3T3R), and 3-DOF planar motion in combination with the other 3-DOF spatial motion (3P3S).

2.5 Structure Synthesis of 3-limb 6-DOF PMs with 3-3 GD

Structure synthesis is the starting point of the design of a PM. As there is no systematic approach for synthesizing PMs with decoupled motion. A procedure is proposed for structure synthesis of 3-limb symmetrical 6-DOF 3-3 Decoupled PMs as follows.

- **STEP 1**: Based on decoupled motion requirements, the wrench system of the moving platform is analyzed, and the limb wrench system is obtained according to the symmetrical property.
- **STEP 2**: Inspect the search space (see Fig. 2.1) for 4-system limbs with the desired wrench system obtained from STEP 1, and enumerate all the limb sub-chains with only passive kinematic pairs.
- **STEP 3**: Determine the type of actuators and geometry in each limb obtained from STEP 2 based on the line geometry method.
- **STEP 4**: Construct the 3-limb 6-DOF PMs using the serial limb chains obtained in STEP 3 while following the geometrical requirements from STEP 1.

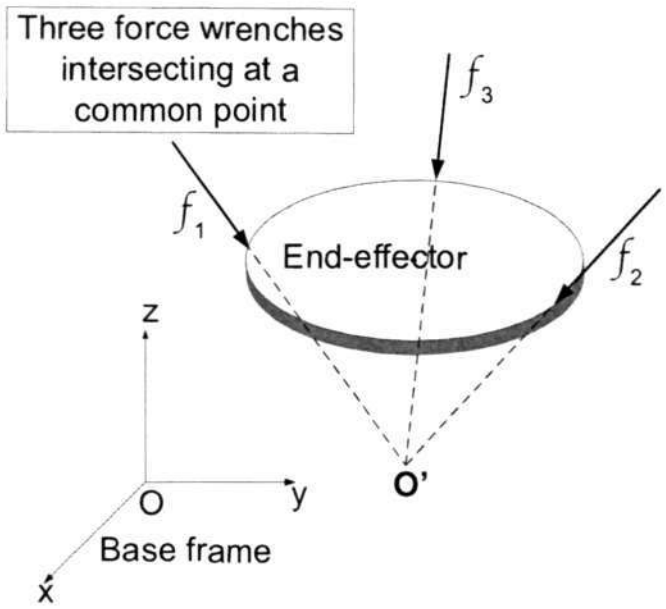

Figure 2.2: Wrench system for 3-DOF translation

2.6 Structure Synthesis of PMs with Decoupled Translation and Rotation

2.6.1 Wrench System Analysis

The 3-limb symmetrical structure requirement determines that each limb has two 1-DOF actuators [103]. To avoid over-constraint [61] and redundancy, the connectivity [103] of each limb should be six and all the joints in each limb should be independent in finite motion. The objective here is to synthesize 6-DOF PMs with decoupled translation and rotation. In other words, when the three actuators related to rotation are locked, the end-effector will have only translations. When the three actuators related to translation are locked, the end-effector will have only rotations. According to the statics analysis [43], three force wrenches (f_1, f_2 and f_3 in Fig. 2.2) are required to constrain the end-effector for three translational DOFs, and three moment wrenches (n_1, n_2 and n_3 in Fig. 2.3) are required for three rotational DOFs of the end-effector. The three force wrenches must form a 3-system, so that geometrically the three forces cannot share one common plane. The three moment wrenches must also form a 3-system. The geometric condition

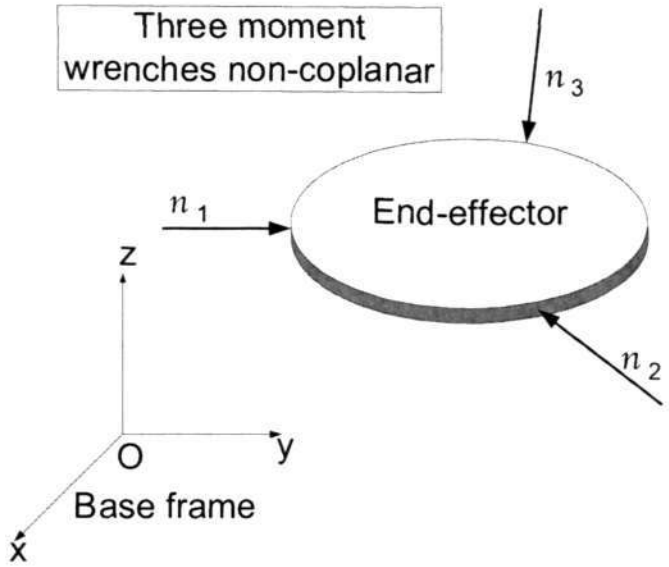

Figure 2.3: Wrench system for 3-DOF rotation

requires that any two moments cannot be in parallel, and the three moments cannot share a common plane. Without loss of generality, f_1 and n_1 are regarded to be associated with limb 1 according to the symmetrical property. Hence, one force wrench and one moment wrench are required for each limb due to the symmetrical property. Note that the three forces need to intersect at one common point which can move along with the end-effector.

2.6.2 Synthesis of Limb Sub-chains with Only Passive Joints

As each limb has two 1-DOF actuators, for the non-redundant mechanism, each limb serial chain with only passive joints should form a 4-system. All the screws associated with the passive joints should be reciprocal to one force wrench and one moment wrench. Inspecting those limbs of the 4-system in Fig. 2.1, those who can provide an IP wrench can be of type 4R(c), 2R2P(b), 3R1P(C) and 3R1P(d). Based on the geometrical constraints of these limb types, four configurations of limbs are constructed as shown in Fig. 2.4.

2.6.3 Determination of Type and Geometry of Actuators

This step is to add the two actuators to the obtained sub-chains. In other words, two active joint screws are required to connect the sub-chain to form a limb of 6-system. Specially, each one of the two active joint screws are to be reciprocal to one of the two wrenches respectively. For design purpose, all the actuators are preferred to be mounted on or close to the base, so that only the first two positions of each limb serial chain (numbering from the base to the end-effector) are considered for mounting the actuators.

Adding two active joint screws based on the line geometry (note that the maximal number of independent screw axes in parallel is three), only the limb sub-chain shown in Fig. 2.4(b) can be expanded to two feasible serial limb chains which provides a ZP wrench and an IP wrench as shown in Fig. 2.5.

2.6.4 Enumeration of Feasible Mechanisms

With the feasible limbs obtained in Fig. 2.5, the desired decoupled PMs are enumerated as shown in Fig. 2.6 based on the geometrical requirements obtained in Step 1 by symmetrically connecting three identical limbs between the base and the end-effector. Note that the axes of the two actuators in each limb may not be aligned.

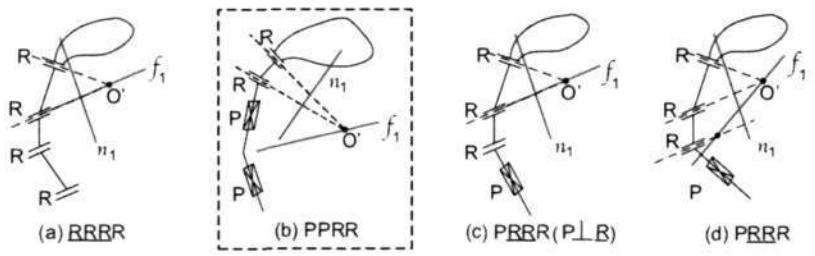

Figure 2.4: Limb sub-chains with only passive joints

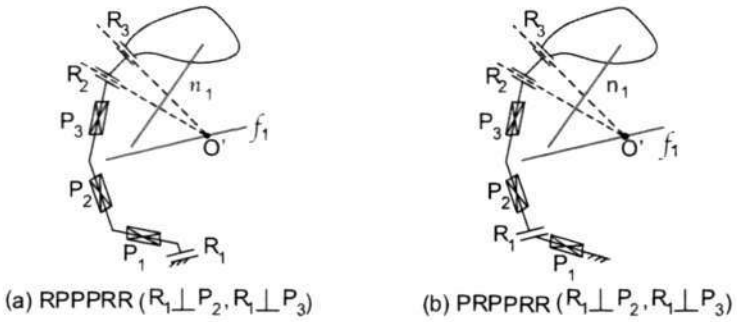

Figure 2.5: Feasible limbs for 3T3R PMs

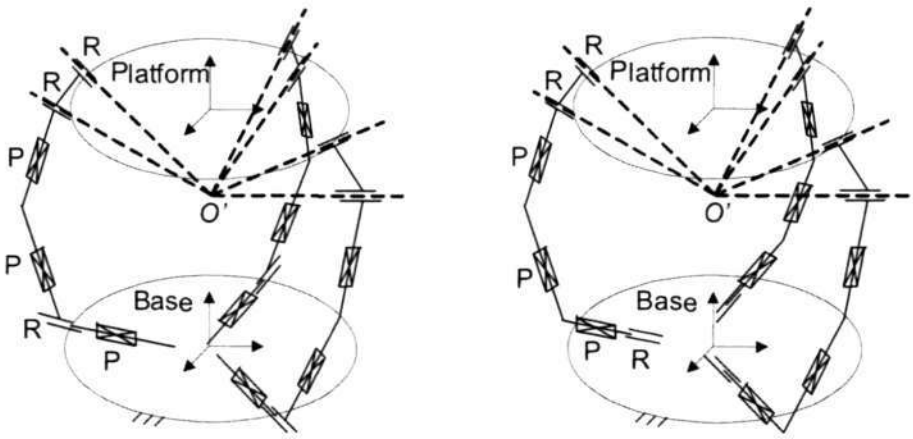

Figure 2.6: Parallel mechanisms with decoupled translation and rotation

2.7 Structure Synthesis of 3P3S PMs

In this section, we study the structure synthesis of 3P3S PMs, which have decoupled 3-DOF planar motion and 3-DOF spatial motion.

2.7.1 Wrench System Analysis

For 3-DOF planar motion (two translations along the horizontal plane and one rotation about a vertical axis), three forces in parallel are required to constrain the end-effector, as shown in Fig.2.7. Note that the three force wrenches must form a 3-system. This implies that the three forces cannot share one common plane. In other words, the three forces

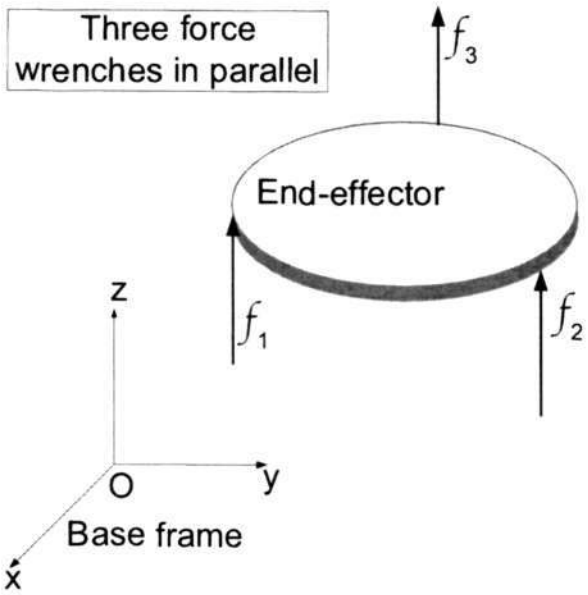

Figure 2.7: Wrench system for 3-DOF planar motion

must be independent of each other.

For 3-DOF spatial motion (two rotations about the axes parallel to the horizontal plane, and one translation along the vertical direction), three other forces are required for constraining the end-effector, as shown in Fig. 2.8. In order to keep the three forces a 3-system, the geometrical arrangements of the forces must satisfy:

- the three forces are coplanar;
- any two of the three forces are not in parallel;
- the three forces do not intersect at a common point.

For symmetry, each limb should be associated with two force wrenches, i.e., one along the vertical direction and the other parallel to the horizontal plane. Without loss of generality, f_1 and f_4 are taken to be associated with limb 1. Note that the two force wrenches associated with a limb are mutually perpendicular.

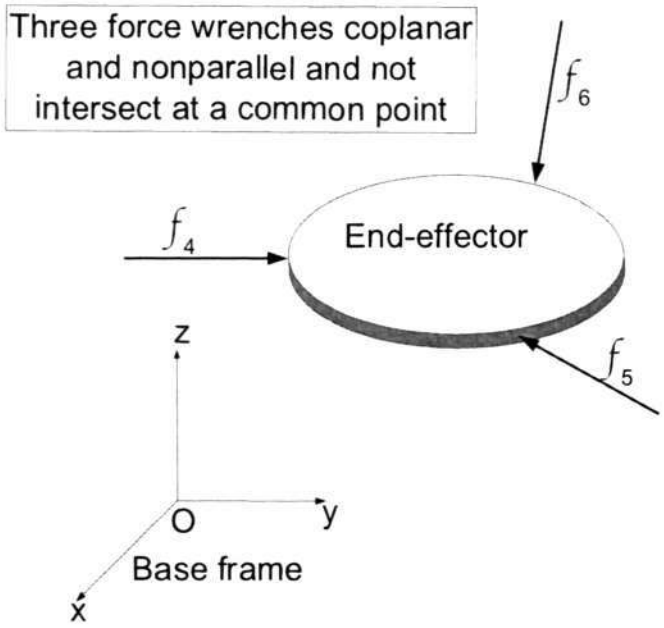

Figure 2.8: Wrench system for 3-DOF spatial motion

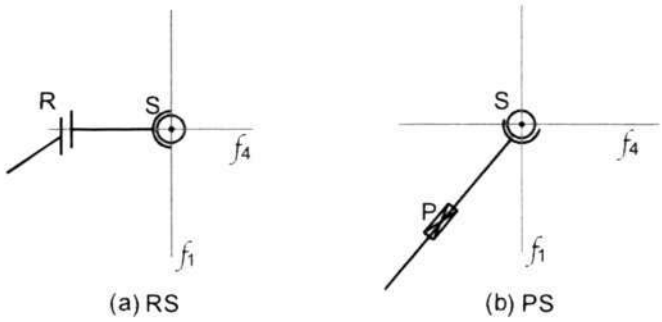

Figure 2.9: Limb sub-chains with only passive joints

2.7.2 Synthesis of Limb Sub-chains with Only Passive Joints

As the wrench system associated with each limb forms a 2-system, the order of sub-chain with only passive joints should be four. Checking those limbs of 4-order in Fig. 2.1, only type 4R(a) and 3R1P(b) can satisfy the wrench requirements. Based on the geometrical constraints, two sub-chain configurations are constructed as shown in Fig. 2.9. Note that a spherical joint (S) is used to represent three R-joints intersecting at one common point in Fig. 2.9.

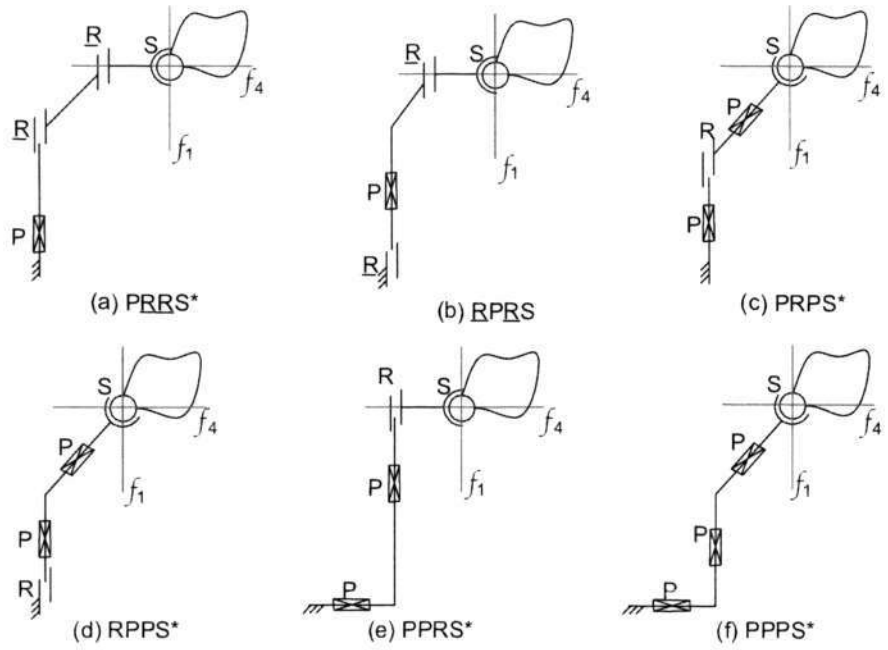

Figure 2.10: Feasible limbs for 3P3S PMs

2.7.3 Determination of Type and Geometry of Actuators

Based on the line geometry, two actuators are added into these sub-chains shown in Fig. 2.9. The feasible limb serial chains are enumerated as shown in Fig. 2.10.

2.7.4 Enumeration of Feasible Mechanisms

Based on the geometrical requirements of the platform wrench system obtained in Section 2.7.1, the desired decoupled PMs can be enumerated by symmetrically connecting three identical limbs between the base and end-effector as shown in Fig. 2.11.

A modular PM [112] is constructed based on the 3-PRRS structure. However, the decoupling motion characteristics has not been disclosed. Yang et al. [110] studied the decoupling characteristics of the 3-RPRS structure. Shim et al. [98] mentioned a decoupled 3-PRPS 6-DOF PM in which the two prismatic joints of each limb are actuators. Hence, from the perspective of decoupled motion, these structures in Fig. 2.11(a, c, d, e, f) are new.

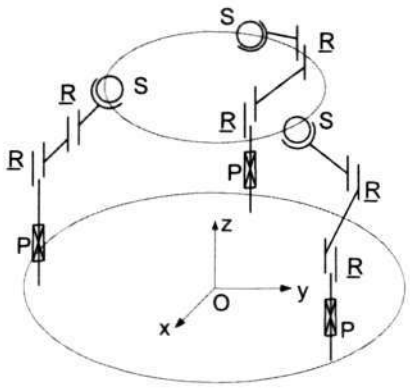

(a) 3-P<u>RR</u>S*

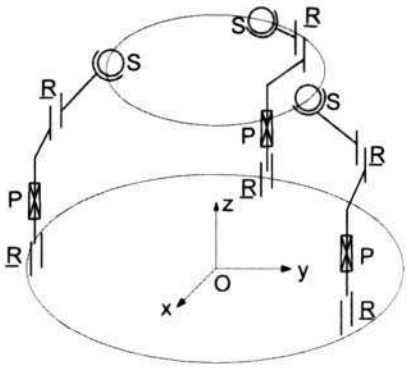

(b) 3-<u>R</u>P<u>R</u>S

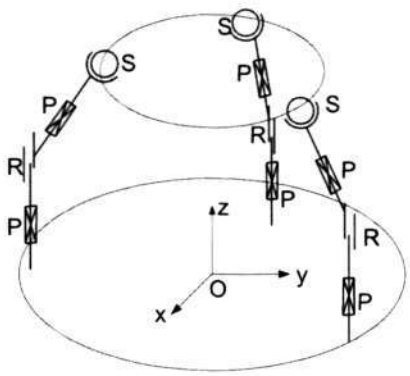

(c) 3-PRPS*

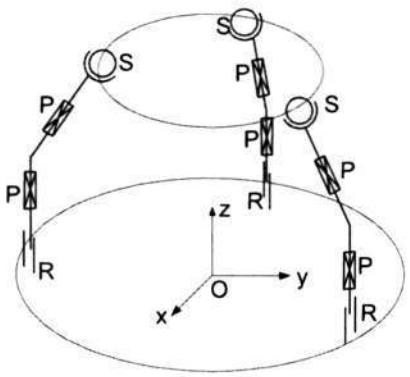

(d) 3-RPPS*

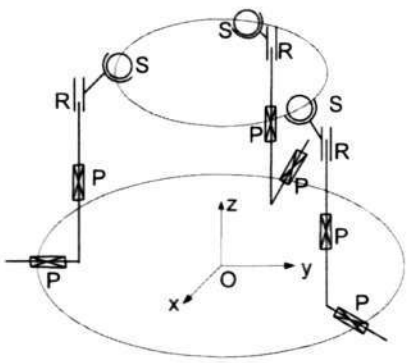

(e) 3-PPRS*

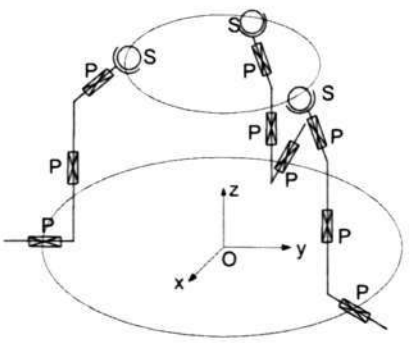

(f) 3-PPPS*

Figure 2.11: Parallel mechanisms with decoupled 3-DOF planar motion and 3-DOF spatial motion (*new structure)

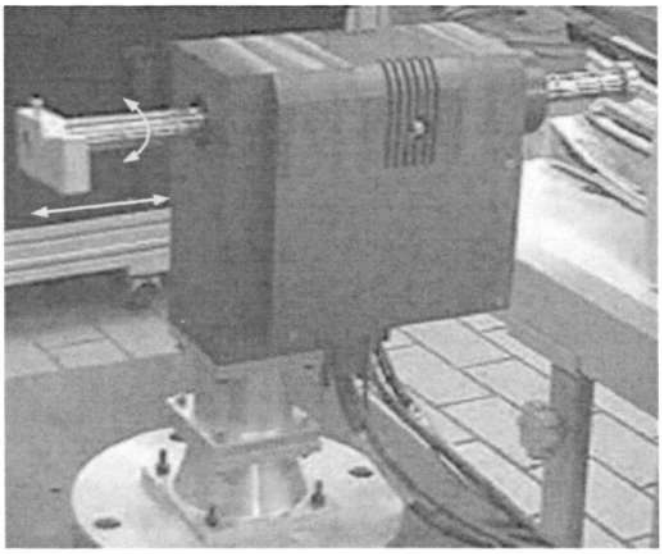

Figure 2.12: The 2-DOF actuator module [76]

Remark (2-DOF Drive Unit): Analyzing the PMs obtained in Sections 2.6 and 2.7, we find that most of the PMs (Fig. 2.6(a), 2.6(b), 2.11(a), 2.11(b), 2.11(c) and 2.11(d)) may employ one linear actuator and one rotary actuator along the same axis. For implementation of these PMs with all actuators mounted on the base, we have developed a 2-DOF actuator module that combines a pure rotation and a pure translation on a single shaft as shown in Fig. 2.12 [76]. Two DC servo motors (SilverMax) are used as the driving units through two timing belts. The Ball-Screw Spline mechanism (THK) is used to provide the combination of rotation and translation on a single compact design. The ball-screw spline mechanism can achieve three modes of motion (rotational, linear and spiral) on a single shaft by rotating or stopping the ball-screw and spline nuts through the motion coordination of the two motors.

2.8 Summary

The PMs with decoupled motion are classified, and the concept of Group Decoupling is introduced. An idea of sharing sub-chain composed by only passive joints is introduced. A systematic approach based on this idea is proposed for structure synthesis of 3-limb

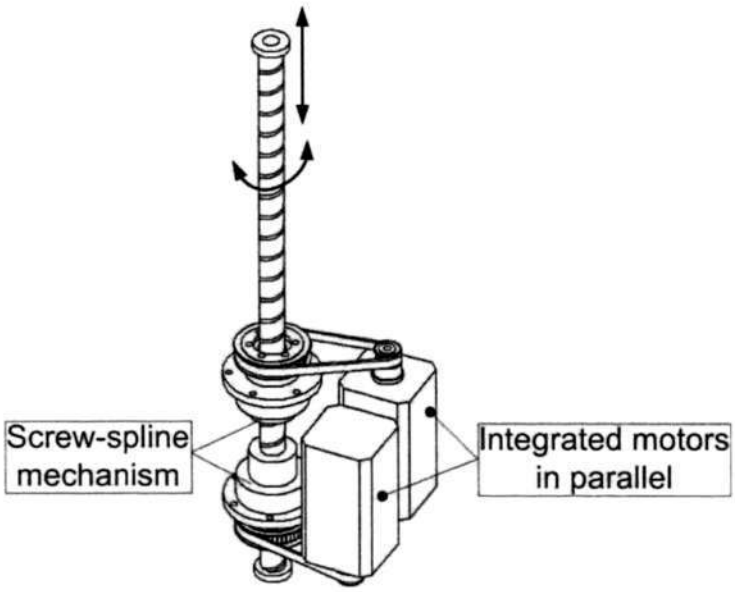

Figure 2.13: Internal structure of 2-DOF actuator [76]

symmetrical 6-DOF PMs with 3-3 decoupled motion. A search space including serial limb chains with at least one zero-pitch wrench is developed, which saves effort of a designer on structure synthesis. This search space is useful not only for synthesizing decoupled PMs but also synthesis of PMs with lower DOFs. Two classes of 3-3 decoupled parallel manipulators are obtained, in which seven novel structures are obtained. For ease of implementation of these PMs, a 2-DOF actuator which can provide both linear and rotary motions along the same axis is newly developed.

Chapter 3

Instantaneous Kinematics and Singularity Analysis

Instantaneous kinematics is to establish the relationships between the instantaneous motion of the active joints to that of the end-effector. This relationship is very important in analyzing the motion and control of robotic manipulators. In this chapter, we will derive the instantaneous kinematics and singularity conditions of the decoupled PMs obtained in the previous chapter.

This chapter is organized as follows. Section 3.2.1 briefly reviews the significant research results in instantaneous kinematics and singularity analysis of PMs. Section 3.2 introduced the instantaneous kinematics and singularity analysis of the 3T3R PMs. The instantaneous kinematics and singularity conditions of the 3P3S PMs are derived in Section 3.3.

3.1 Introduction

A number of researchers have studied the instantaneous kinematics of PMs [6, 66, 84]. Mohamed and Duffy [84] proposed the concept of partial twists for instantaneous kinematic analysis, in which the instantaneous motion of the end-effector is expressed only in terms of the twists of actuators. Kumar [66] derived the instantaneous kinematics of

PMs using an approach based on reciprocal screw. Angeles [6] proposed the concept of screw system annihilators to systematically formulate instantaneous kinematics.

One of the early work of singularity analysis is that of Gosselin and Angeles [26]. In this work, the relationship between the input joint rates ($\dot{\boldsymbol{\theta}}$) and the output moving platform velocity ($\dot{\mathbf{x}}$) of a PM is

$$J_x\dot{\mathbf{x}} = J_\theta\dot{\boldsymbol{\theta}}. \tag{3.1}$$

Three different types of singularities can be identified, i.e., forward singularity (J_x is singular), inverse singularity (J_θ is singular) and combined singularity (J_x and J_θ are simultaneously singular). J_x and J_θ are the manipulator forward and inverse Jacobian matrices respectively.

A number of methods based on screw theory and line geometry have been proposed for analyzing the singularities of closed-chain manipulators. Hunt [45] laid down a geometrical framework for applying screw theory to singularity analysis and presented the concept of stationary and uncertainty configurations. Kumar [66] formulated the instantaneous kinematic relationship of closed-chains by using the concept of screw reciprocity. In this work, the singularity conditions due to the actuator location were also discussed. Merlet [79] showed that all the singularities of the Stewart type of parallel manipulators can be analytically enumerated by using line geometry method. Collins [18] proposed an approach for determining the singularities of parallel manipulators by using screw theory and Clifford algebras.

Park and Kim [91] proposed a coordinate invariant differential geometric analysis of singularities of closed-loop chains. In this geometric framework, both redundant and non-redundant systems, including the case of redundant actuation, are treated in a uniform manner.

Liu et al. [73] presented a mathematical tool for singularity analysis by using the language of differential forms. In this work, various singularities, and their relationship with the

kinematic parameters and the configuration space were studied in a general approach, and the effects of redundant actuation on singularities were also considered.

Yang et al. [111] proposed a novel method for singularity analysis of a class of three-legged parallel manipulators, in which a spherical joint was used to connected to the moving platform in each leg. Based on the instantaneous velocities of passive joints, the forward singular conditions were realized by analyzing a 3×3 matrix associated with passive joint velocities. The inverse singularities of each leg is determined by one 3×3 matrix, so totally three 3×3 matrices are obtained for all three legs. Therefore, the complexity of singularity analysis is significantly reduced because only the four 3×3 matrices need to be analyzed.

3.2 Analysis on PMs with Decoupled Translation and Rotation

3.2.1 Description of 3T3R PMs

As shown in Fig. 3.1, this class of PMs is constructed with a moving platform and a base connected by three identical serial chains in parallel. Each of the three actuators is mounted on the base, followed by P, P, R, R passive joints. Note that the three actuator axes are not in parallel to one plane and any two of them are not in parallel. Each actuator has two DOFs, i.e., one linear translation DOF along the driving axis and a rotary DOF along the same axis. Other geometrical requirements include: 1) the two passive P-joint axes are perpendicular to the actuator axis in each limb; 2) the last two passive R-joints in every limb must intersect at one common point O', which is the rotation center of the end-effector.

As shown in Section 2.6, when the PM is driven by the three rotary actuator motions, the end-effector of the manipulator will produce only a 3-DOF rotary motion (spherical motion). When the actuation becomes three linear motions, the end-effector produces

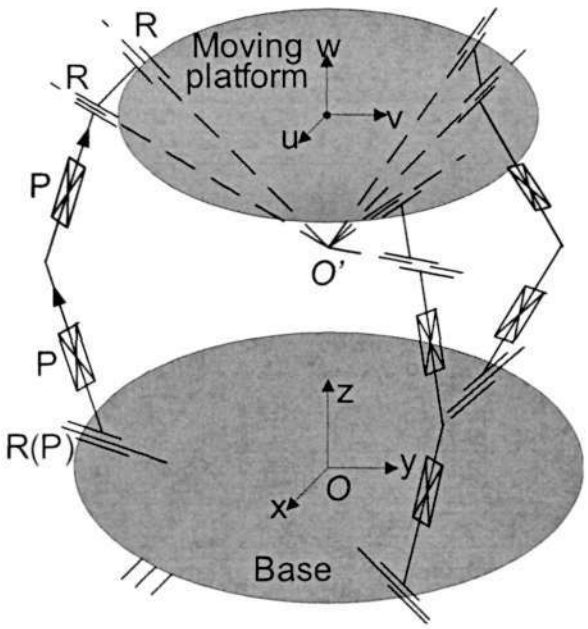

Figure 3.1: Schematic description of the 3T3R PMs

only 3-DOF spatial translation. With all 6-DOF actuation, the end-effector will produce general 6-DOF spatial motion with decoupled translation and rotation. With different actuator motions, the manipulator may produce different types of movements. Hence, we term this manipulator a *Selectively Actuated Parallel manipulator*, or simply an *SA-PM*. To verify its feasibility, a Lego model (Fig. 3.2) and a CAD model (Fig. 3.3) of the PM are constructed. As Lego parts are made of plastics, the constructed PM model may have compliance so that it is only suitable for preliminary idea development and verification. Note that in this Lego model, the actuator was represented as the R(P) cylindrical joint at the base instead of the real one.

3.2.2 Instantaneous Kinematics of SA-PM

In this section, the instantaneous kinematics is formulated, which shows that the decoupling characteristics can be directly identified by using *hybrid velocity representation* [87].

Kinematic decoupling means that the motion of the end-effector along different motion

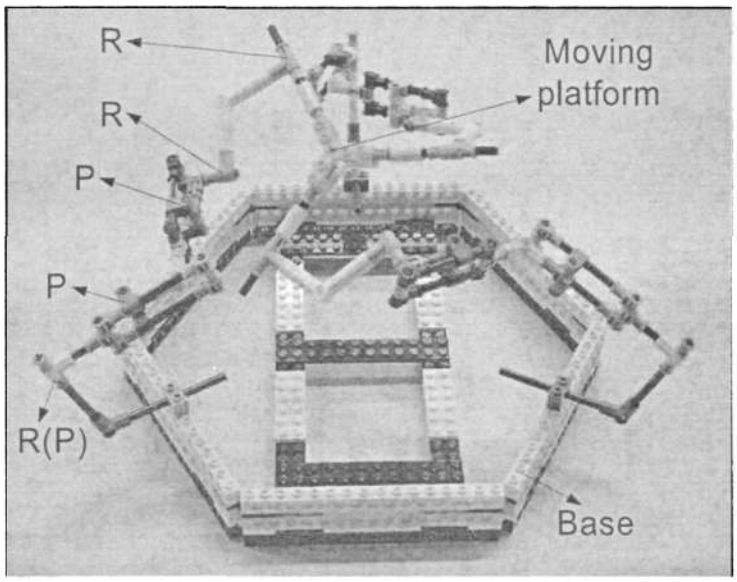

Figure 3.2: Lego model of the SA-PM (View point is located at upper 45 degree in front.)

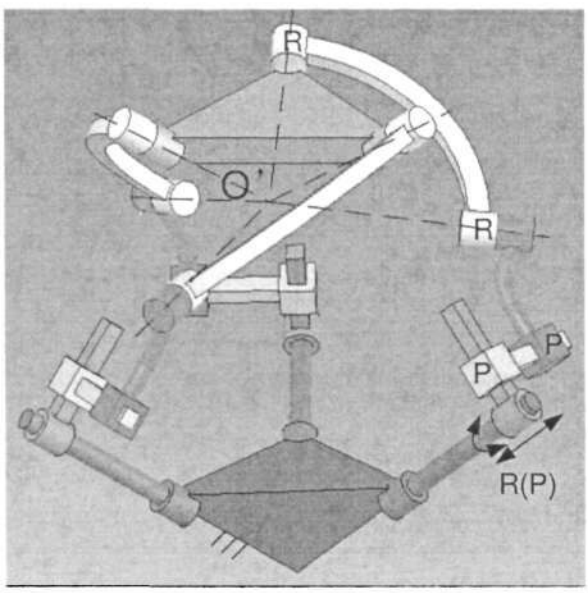

Figure 3.3: CAD Model of SA-PM

axes will be controlled by the respective actuators. For the SA-PM, the velocity decoupling allows end-effector velocity $(\boldsymbol{w}, \boldsymbol{v})$ to be written as the following function of actuator rates,

$$\begin{cases} \boldsymbol{w} = w(\dot{\theta}_{11}, \dot{\theta}_{21}, \dot{\theta}_{31}) \\ \boldsymbol{v} = v(\dot{\theta}_{11}, \dot{\theta}_{21}, \dot{\theta}_{31}, \dot{\theta}_{12}, \dot{\theta}_{22}, \dot{\theta}_{32}) \end{cases}, \tag{3.2}$$

where $\dot{\theta}_{i1}$, $\dot{\theta}_{i2}$ represent rotational and translational velocities of the 2-DOF actuator in the i^{th} limb respectively. Note that $\boldsymbol{v}$ in eqn.(3.2) represents the linear velocity of a point which belongs to the body and is coincident with the origin of the reference system. As point O' is the rotation center of the end-effector, the origin of the reference frame can also be located at O', then the end-effector velocity can be reduced to the following expression

$$\begin{cases} \boldsymbol{w} = w(\dot{\theta}_{11}, \dot{\theta}_{21}, \dot{\theta}_{31}) \\ \boldsymbol{v} = v'(\dot{\theta}_{12}, \dot{\theta}_{22}, \dot{\theta}_{32}) \end{cases}. \tag{3.3}$$

Hence, the rotary velocity and translational velocity of the end-effector can always be determined by the rotary velocity and linear velocity of the actuator respectively. In this way, motion decoupling can be directly identified and evaluated when the manufacturing and assembly errors are considered [51]. The velocity of the end-effector is called *hybrid velocity* [87] representing the velocity of the rigid body relative to the frame attached to the origin of the rigid body with its orientation fixed relative to the inertial frame. Figure 3.4 shows the ith limb of the PM, three Cartesian coordinate systems are fixed to the PM respectively, i.e., the reference frame $\{O' - xyz\}$, the base frame $\{O - xyz\}$ and the end-effector frame $\{O' - uvw\}$. Note that the two origins of the wrist frame and the end-effector frame are coincident, and the coordinate axes of the base frame and the wrist frame are always in parallel. All joint screws are expressed with respect to the wrist frame. Let $s_{i,j}$ be a unit vector along the jth joint axis of the ith limb. Then the six unit joint screws of a limb can be written as:

$$\hat{\$}_{i1} = \begin{bmatrix} \boldsymbol{s}_{i1} \\ \boldsymbol{O'A}_{i1} \times \boldsymbol{s}_{i1} \end{bmatrix}, \quad i\text{=1,2,3 (for rotary actuator);}$$

$$\hat{\$}_{i2} = \begin{bmatrix} 0 \\ \boldsymbol{s}_{i1} \end{bmatrix}, \quad i\text{=1,2,3 (for linear actuator);}$$

$$\hat{\$}_{i3} = \begin{bmatrix} 0 \\ \boldsymbol{s}_{i3} \end{bmatrix}, \quad \hat{\$}_{i4} = \begin{bmatrix} 0 \\ \boldsymbol{s}_{i4} \end{bmatrix}, \quad i\text{=1,2,3;}$$

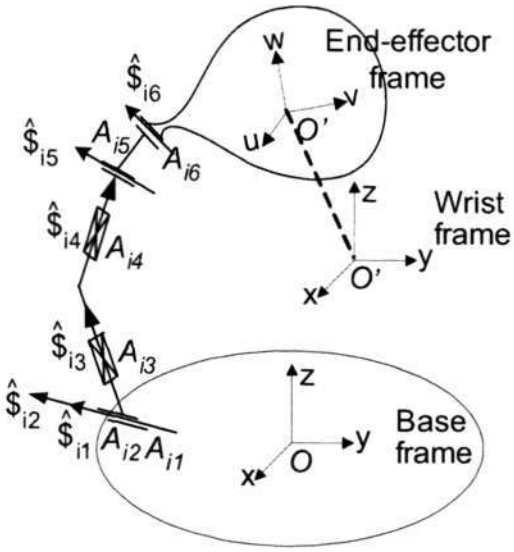

Figure 3.4: The ith limb of SA-PM

$$\hat{\$}_{i5} = \begin{bmatrix} \boldsymbol{s}_{i5} \\ \boldsymbol{O'A}_{i5} \times \boldsymbol{s}_{i5} \end{bmatrix}, \quad \hat{\$}_{i6} = \begin{bmatrix} \boldsymbol{s}_{i6} \\ \boldsymbol{O'A}_{i6} \times \boldsymbol{s}_{i6} \end{bmatrix}, \quad i=1,2,3.$$

The instantaneous twist $\$_{O'}$ of the end-effector can be expressed as

$$\$_{O'} = \dot{\theta}_{i1}\hat{\$}_{i1} + \dot{\theta}_{i2}\hat{\$}_{i2} + \dot{\theta}_{i3}\hat{\$}_{i3} + \dot{\theta}_{i4}\hat{\$}_{i4} + \dot{\theta}_{i5}\hat{\$}_{i5} + \dot{\theta}_{i6}\hat{\$}_{i6}, \quad i=1,2,3, \tag{3.4}$$

where $\dot{\theta}_{ij}$ represents the joint rates of limb i, i.e., $\dot{\theta}_{i1}$, $\dot{\theta}_{i2}$ represent rotary and the linear velocities of the 2-DOF actuator respectively, and $\dot{\theta}_{i3}$, $\dot{\theta}_{i4}$ represent the linear velocities of the two passive prismatic joints, and $\dot{\theta}_{i5}$, $\dot{\theta}_{i6}$ represent the rotary velocities of corresponding joints.

According to structure synthesis, the screw that is reciprocal to all the passive joint screws but not reciprocal to the first active joint should be

$$\$_{ir1} = \begin{bmatrix} 0 \\ \boldsymbol{s}_{i5} \times \boldsymbol{s}_{i6} \end{bmatrix} \quad i=1,2,3. \tag{3.5}$$

Note that $\$_{ir1}$ is invalid if the plane determined by $\hat{\$}_{i5}$ and $\hat{\$}_{i6}$ is parallel to $\hat{\$}_{i1}$ due to the reciprocality to the actuator. This configuration in which the plane determined by $\hat{\$}_{i5}$ and $\hat{\$}_{i6}$ is parallel to $\hat{\$}_{i1}$, is an inverse singular configuration because the three screws associated with R-joints in the limb are dependent as shown in eqn. 3.9. As a result, the platform will lose one DOF because one more constraint will be imposed on the moving platform.

Another screw that is reciprocal to all the passive joint screws but not reciprocal to the second active joint should be:

$$\hat{\$}_{ir2} = \begin{bmatrix} \boldsymbol{s}_{i1} \\ \mathbf{0} \end{bmatrix} \qquad i=1,2,3. \tag{3.6}$$

Taking the orthogonal product of both sides of instantaneous kinematics eqn. (3.4) with $\$_{ir1}$ and $\$_{ir2}$, we have

$$J_x \dot{\mathbf{x}} = J_\theta \dot{\boldsymbol{\theta}}, \tag{3.7}$$

where $J_x = \begin{bmatrix} A & 0 \\ 0 & C \end{bmatrix}$, $J_\theta = \begin{bmatrix} D & 0 \\ 0 & I \end{bmatrix}$,

$A = [\, \boldsymbol{s}_{15} \times \boldsymbol{s}_{16} \quad \boldsymbol{s}_{25} \times \boldsymbol{s}_{26} \quad \boldsymbol{s}_{35} \times \boldsymbol{s}_{36} \,]^T$,

$C = [\, \boldsymbol{s}_{11} \quad \boldsymbol{s}_{21} \quad \boldsymbol{s}_{31} \,]^T$,

$D = diag\,[(\boldsymbol{s}_{15} \times \boldsymbol{s}_{16}) \cdot \boldsymbol{s}_{11}, (\boldsymbol{s}_{25} \times \boldsymbol{s}_{26}) \cdot \boldsymbol{s}_{21}, (\boldsymbol{s}_{35} \times \boldsymbol{s}_{36}) \cdot \boldsymbol{s}_{31}]$,

$\dot{\mathbf{x}} = [\boldsymbol{w}, \boldsymbol{v}]^T$, $\dot{\boldsymbol{\theta}} = \left[\dot{\theta}_{11}, \dot{\theta}_{21}, \dot{\theta}_{31}; \dot{\theta}_{12}, \dot{\theta}_{22}, \dot{\theta}_{32}\right]^T$. A, C, D are all 3×3 sub-matrices, and I is a 3×3 identity matrix.

Expanding eqn.(3.7), we have

$$\begin{cases} A\boldsymbol{w} = D\dot{\boldsymbol{\theta}}_1 \\ C\boldsymbol{v} = \dot{\boldsymbol{\theta}}_2 \end{cases}. \tag{3.8}$$

where $\dot{\boldsymbol{\theta}}_1 = \left[\dot{\theta}_{11}, \dot{\theta}_{21}, \dot{\theta}_{31}\right]$ and $\dot{\boldsymbol{\theta}}_2 = \left[\dot{\theta}_{12}, \dot{\theta}_{22}, \dot{\theta}_{32}\right]$.

Equation (3.8) obviously shows that the angular velocity is controlled by the three rotary elements of the actuators, and the linear velocity of the end-effector is determined by the linear elements of the three actuators. In other words, the translation and orientation movement of the end-effector is decoupled.

3.2.3 Singularity Analysis of SA-PM

Inverse Singularity

The inverse singularity occurs in the manipulator configuration when the moving platform loses one or more degrees of freedom instantaneously. The actuator velocities cannot be determined by the given moving platform velocity. In other words, the moving platform

will be constrained by more wrenches instantaneously in the inverse singular configuration. As each limb has three R-joints and three independent P-joints, the inverse singularity occurs when the three R-joints are dependent. Based on the geometry, the condition of inverse kinematic singularity is

$$(\boldsymbol{s}_{i5} \times \boldsymbol{s}_{i6}) \cdot \boldsymbol{s}_{i1} = 0. \tag{3.9}$$

The geometric explanation is that the three R-joints share one common plane when singularity occurs. As a result, the platform will lose one or more DOFs in this configuration.

Forward Singularity

Forward singularity occurs when the moving platform gains one or more degrees of freedom instantaneously. In this configuration, the moving platform can move even though all actuators are locked. The condition of forward kinematic singularity is

$$det(J_x) = det(A) \cdot det(C) = 0. \tag{3.10}$$

Equation (3.10) can be further expanded into

$$[(\boldsymbol{s}_{15} \times \boldsymbol{s}_{16}) \times (\boldsymbol{s}_{25} \times \boldsymbol{s}_{26})] \cdot (\boldsymbol{s}_{35} \times \boldsymbol{s}_{36}) = 0, \tag{3.11}$$

or

$$(\boldsymbol{s}_{11} \times \boldsymbol{s}_{21}) \cdot \boldsymbol{s}_{31} = 0. \tag{3.12}$$

Obviously, the left-hand side of eqn. (3.11) is equivalent to the volume of the tetrahedron formed by the three vectors, $(\boldsymbol{s}_{15} \times \boldsymbol{s}_{16}), (\boldsymbol{s}_{25} \times \boldsymbol{s}_{26})$ and $(\boldsymbol{s}_{35} \times \boldsymbol{s}_{36})$. When the volume of the tetrahedron vanishes, the forward singularity will occur. As a result, two geometrical conditions can be readily identified:

- Any two of the three vectors are parallel. Due to the six passive R-joints intersecting at the common point O', the forward singularity occurs when four R-joints in any two limbs are coplanar. This singular configuration is illustrated by the Lego model of Fig. 3.5.

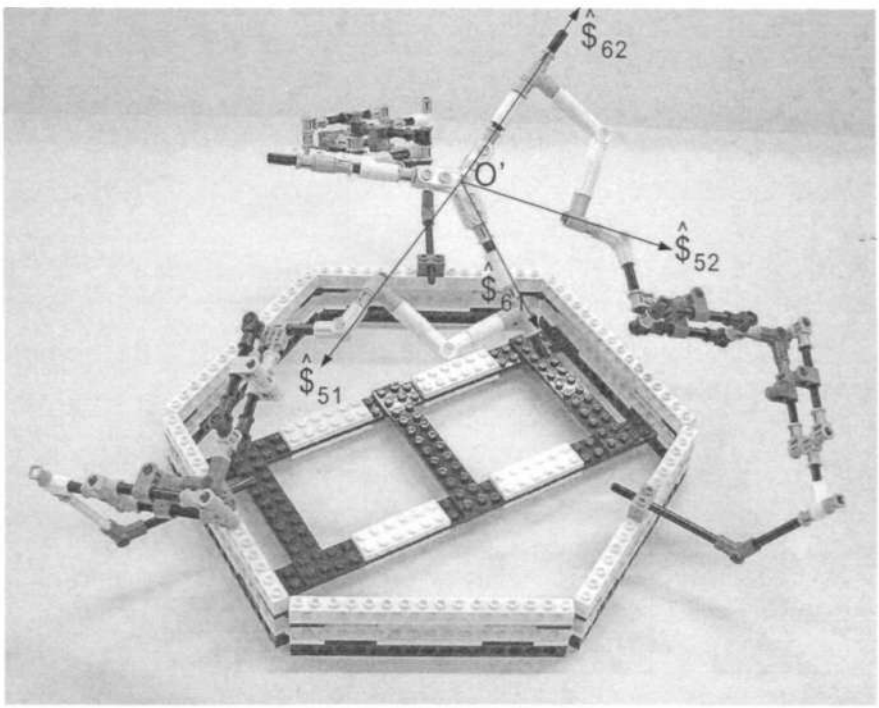

Figure 3.5: Forward singular configuration I (Four R-joints in a plane)

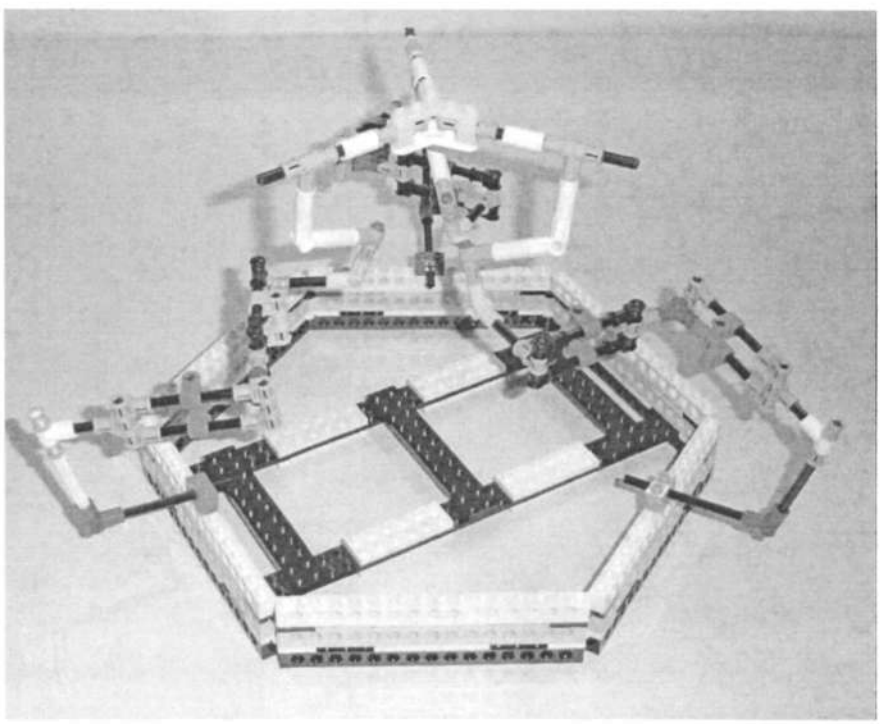

Figure 3.6: Forward singular configuration (Π Three planes determined by $\boldsymbol{s}_{i5}$ and $\boldsymbol{s}_{i6}$ perpendicular to a common plane)

- All the three vectors are parallel to the same plane. In other words, the forward singularity occurs if the three plane determined by $\boldsymbol{s}_{i5}$ and $\boldsymbol{s}_{i6}$ $(i = 1, 2, 3)$ are perpendicular to a common plane. The configuration can be recognized easily using the Lego model as shown in Fig. 3.6. In this configuration, the rotation about the normal of the common plane cannot be controlled.

Similarly, the left-hand side of eqn. (3.12) is equivalent to the volume of the tetrahedron formed by the three vectors, $\boldsymbol{s}_{11}, \boldsymbol{s}_{21}$ and $\boldsymbol{s}_{31}$. Due to the geometrical conditions of the structure, such forward singularities will never occur because the volume of the tetrahedron will never be equal to zero.

Combined Singularity

Solving eqn. (3.9) and eqn. (3.10) together, the combined singularity occurs in two situations: 1) four passive R-joints of any two limbs are in one plane which is parallel to the two actuator driving axes of the two limbs; 2) the six passive R-joints share one plane, and all the actuator driving axes are parallel to this plane. Because all actuator axes are not parallel to the same plane, the second situation is impossible. As combined singularity depends on the mechanism dimensions that the first situation can be avoided by choosing appropriate dimensions in the design stage.

Note that the PM will have only 3-DOF translation when only the three linear actuators is used to drive (refer to eqn. (3.8)). Specially, as each row of matrix C is the unit vector of the axis of the actuator, we can obtain the isotropic mechanism if the three actuator axes are mounted mutually orthogonal, i.e., the condition number of the Jacobian matrix is 1. Furthermore, if the base coordinate frame is fixed such that vectors $\boldsymbol{s}_{11}, \boldsymbol{s}_{21}$ and $\boldsymbol{s}_{31}$ are aligned with the $x-$, $y-$ and $z-$axes of the base coordinate system, the Jacobian matrix becomes the identity matrix. No computation is required for the forward displacement analysis, inverse displacement analysis and the associated velocity analysis. Each of the translation components along the $x-$, $y-$ and $z-$axes of the moving platform

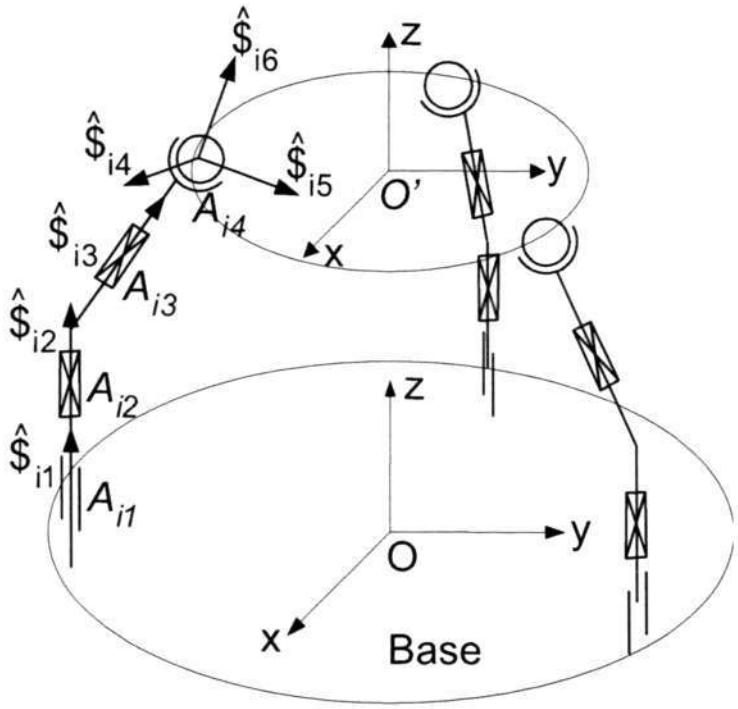

Figure 3.7: Schematic description of the 3-RPPS PM

is independently controlled by its corresponding actuator.

3.3 Analysis on 3P3S PMs

3.3.1 Instantaneous Kinematics

As shown in Section 2.7, each limb is associated with two force wrenches, f_1 and f_2, which are reciprocal to the two actuators respectively. Based on eqn. (3.4), the instantaneous kinematic equation can be formulated directly by orthogonally multiplying the corresponding reciprocal screw six times for the three limbs. In following part, we will take the 3-RPPS structure as an example for formulating the instantaneous kinematic equation.

As shown in Fig. 3.7, two Cartesian coordinate systems are fixed on the base and the moving platform respectively. All the joint screws are expressed with respect to the base

frame $\{O-xyz\}$. Let $s_{i,j}$ be a unit vector along the jth joint axis of the ith limb, and $A_{i,j}$ $(i=1,2,3; j=1,2,3,4)$ represents the joint center of the jth joint of the ith limb. Assume the coordinates of $A_{i,j}$ are (x_{ij}, y_{ij}, z_{ij}) with respect to the base frame. Specially, we have $l_{i1}=0$ and $l_{i3}=l_{i4}$. Then the six unit joint screws of a limb can be written as:

$$\begin{aligned}
\hat{\$}_{i1} &= [0 \quad 0 \quad 1 \quad y_{i1} \quad -x_{i1} \quad 0]^T, \\
\hat{\$}_{i2} &= [0 \quad 0 \quad 0 \quad 0 \quad 0 \quad 1]^T, \\
\hat{\$}_{i3} &= [0 \quad 0 \quad 0 \quad x_{i4}-x_{i3} \quad y_{i4}-y_{i3} \quad 0]^T, \\
\hat{\$}_{i4} &= [0 \quad 0 \quad 1 \quad y_{i4} \quad -x_{i4} \quad 0]^T, \\
\hat{\$}_{i5} &= [0 \quad 1 \quad 0 \quad -z_{i4} \quad 0 \quad x_{i4}]^T, \\
\hat{\$}_{i6} &= [1 \quad 0 \quad 0 \quad 0 \quad z_{i4} \quad -y_{i4}]^T, \qquad i=1,2,3.
\end{aligned} \tag{3.13}$$

The instantaneous twist $\$_{O'}$ of the end-effector can be expressed as

$$\$_{O'} = \dot{\theta}_{i1}\hat{\$}_{i1} + \dot{\theta}_{i2}\hat{\$}_{i2} + \dot{\theta}_{i3}\hat{\$}_{i3} + \dot{\theta}_{i4}\hat{\$}_{i4} + \dot{\theta}_{i5}\hat{\$}_{i5} + \dot{\theta}_{i6}\hat{\$}_{i6}, \qquad i=1,2,3, \tag{3.14}$$

where $\dot{\theta}_{ij}$ represents the joint rates of limb i, i.e., $\dot{\theta}_{i1}$, $\dot{\theta}_{i2}$ represent rotary and the linear velocities of the 2-DOF actuator respectively, and $\dot{\theta}_{i3}$, $\dot{\theta}_{i4}$ represent the linear velocities of the two passive prismatic joints, and $\dot{\theta}_{i5}$, $\dot{\theta}_{i6}$ represent the rotary velocities of corresponding joints.

According to structure synthesis, the screw that is reciprocal to all the passive joint screws but not reciprocal to the first active joint is

$$\$_{ir1} = \begin{bmatrix} \boldsymbol{s_z} \times \boldsymbol{A_{i3}A_{i4}} \\ \boldsymbol{OA_{i4}} \times (\boldsymbol{s_z} \times \boldsymbol{A_{i3}A_{i4}}) \end{bmatrix} = \begin{bmatrix} y_{i3}-y_{i4} \\ x_{i4}-x_{i3} \\ 0 \\ z_{i4}(x_{i3}-x_{i4}) \\ z_{i4}(y_{i3}-y_{i4}) \\ x_{i4}(x_{i4}-x_{i3}) - y_{i4}(y_{i3}-y_{i4}) \end{bmatrix} \qquad i=1,2,3, \tag{3.15}$$

where $\boldsymbol{s_z} = [0 \quad 0 \quad 1]^T$. Another screw that is reciprocal to all the passive joint screws

but not reciprocal to the second active joint is:

$$\$_{ir2} = \begin{bmatrix} \boldsymbol{s_z} \\ \boldsymbol{OA_{i4}} \times \boldsymbol{s_z} \end{bmatrix} = \begin{bmatrix} 0 \\ 0 \\ 1 \\ y_{i4} \\ -x_{i4} \\ 0 \end{bmatrix}. \tag{3.16}$$

Taking the orthogonal product of both sides of instantaneous kinematics eqn. (3.14) with $\$_{ir1}$ and $\$_{ir2}$, we have

$$J_x \dot{\mathbf{x}} = J_\theta \dot{\boldsymbol{\theta}}, \tag{3.17}$$

where

$$J_x = \begin{bmatrix} y_{13}-y_{14} & x_{14}-x_{13} & 0 & z_{14}(x_{13}-x_{14}) & z_{14}(y_{13}-y_{14}) & x_{14}(x_{14}-x_{13})-y_{14}(y_{13}-y_{14}) \\ y_{23}-y_{24} & x_{24}-x_{23} & 0 & z_{24}(x_{23}-x_{24}) & z_{24}(y_{23}-y_{24}) & x_{24}(x_{24}-x_{23})-y_{24}(y_{23}-y_{24}) \\ y_{33}-y_{34} & x_{34}-x_{33} & 0 & z_{34}(x_{33}-x_{34}) & z_{34}(y_{33}-y_{34}) & x_{34}(x_{34}-x_{33})-y_{34}(y_{33}-y_{34}) \\ 0 & 0 & 1 & y_{14} & -x_{14} & 0 \\ 0 & 0 & 1 & y_{24} & -x_{24} & 0 \\ 0 & 0 & 1 & y_{34} & -x_{34} & 0 \end{bmatrix},$$

$J_\theta = diag\,[A_1, A_2, A_3, 1, 1, 1]$

$A_i = (y_{i1} - y_{i4})(y_{i3} - y_{i4}) + (x_{i4} - x_{i1})(x_{i4} - x_{i3}),\ (i = 1, 2, 3)$

$\dot{\mathbf{x}} = [v_x, v_y, v_z; w_x, w_y, w_z]^T,\ \dot{\boldsymbol{\theta}} = \left[\dot{\theta}_{11}, \dot{\theta}_{21}, \dot{\theta}_{31}; \dot{\theta}_{12}, \dot{\theta}_{22}, \dot{\theta}_{32}\right]^T.$

Equation (3.17) can be expanded into two equations as follows:

$$J_A \cdot \begin{bmatrix} v_z \\ w_x \\ w_y \end{bmatrix} = \begin{bmatrix} \dot{\theta}_{12} \\ \dot{\theta}_{22} \\ \dot{\theta}_{32} \end{bmatrix} \tag{3.18}$$

and

$$J_B \cdot \begin{bmatrix} v_x \\ v_y \\ w_x \\ w_y \\ w_z \end{bmatrix} = J_C \cdot \begin{bmatrix} \dot{\theta}_{11} \\ \dot{\theta}_{21} \\ \dot{\theta}_{31} \end{bmatrix} \tag{3.19}$$

where

$$J_A = \begin{bmatrix} 1 & y_{14} & -x_{14} \\ 1 & y_{24} & -x_{24} \\ 1 & y_{34} & -x_{34} \end{bmatrix},$$

$$J_B = \begin{bmatrix} y_{13}-y_{14} & x_{14}-x_{13} & z_{14}(x_{13}-x_{14}) & z_{14}(y_{13}-y_{14}) & x_{14}(x_{14}-x_{13})-y_{14}(y_{13}-y_{14}) \\ y_{23}-y_{24} & x_{24}-x_{23} & z_{24}(x_{23}-x_{24}) & z_{24}(y_{23}-y_{24}) & x_{24}(x_{24}-x_{23})-y_{24}(y_{23}-y_{24}) \\ y_{33}-y_{34} & x_{34}-x_{33} & z_{34}(x_{33}-x_{34}) & z_{34}(y_{33}-y_{34}) & x_{34}(x_{34}-x_{33})-y_{34}(y_{33}-y_{34}) \end{bmatrix},$$

$J_C = diag\,[A_1, A_2, A_3].$

From eqn. (3.18) and eqn. (3.19), the motion decoupling can be directly identified, i.e., the 3-DOF spatial motion (two rotations w_x and w_y, and one translation v_z) is controlled

by the three prismatic actuators, and the 3-DOF planar motion (two translations v_x and v_y, and one rotation w_z) is controlled by the three rotary actuators.

3.3.2 Singularity Analysis

Inverse Singularity

For these 3P3S-PM structures, inverse singularity occurs when the twist-system of a limb degenerates (the order is less than six). Based on the line geometry, the inverse singularities can be directly identified as shown in Fig. 3.8. For the 3-P$\underline{\text{RR}}$S structure, the inverse singularities occur if and only if the two links $\boldsymbol{A}_{i2}\boldsymbol{A}_{i3}$ and $\boldsymbol{A}_{i3}\boldsymbol{A}_{i4}$ in limb i are in parallel as shown in Fig. 3.8(a). Geometrically, this singularity condition corresponds to the fully stretched or folded configurations. For the 3-$\underline{\text{R}}$P$\underline{\text{R}}$S structures, the inverse singularity conditions are the same as that of the 3-P$\underline{\text{RR}}$S. For the 3-PPRS structure, the inverse singularity occurs when the link $\boldsymbol{A}_{i3}\boldsymbol{A}_{i4}$ is perpendicular to the actuator axis $\$_{i1}$, as shown in Fig. 3.8(c). For structures of types (c), (d) and (f) in Fig. 2.11, there is no inverse singularity. Thus, we can conclude that the inverse singularity of these 3P3S PMs depends on the location of the passive R-joint. If there is a passive R-joint connecting to the spherical joint, the inverse singularities exist. Otherwise, there is no inverse singularity.

Forward Singularity

The forward singularity occurs when the moving platform gains one or more degrees of freedom instantaneously. In other words, the wrench system to constrain the moving platform degenerates (the order is less that six for 3P3S-PMs). Kinematically, it also means that the moving platform will still possess infinitesimal motion in certain directions. The conditions of forward kinematic singularity is

$$det(J_x) = 0. \tag{3.20}$$

As shown in the forward Jacobian matrix J_x, each row of J_x represents a wrench associated with a limb. In fact, the forward Jacobian matrix of a 6-DOF PM is composed of the six

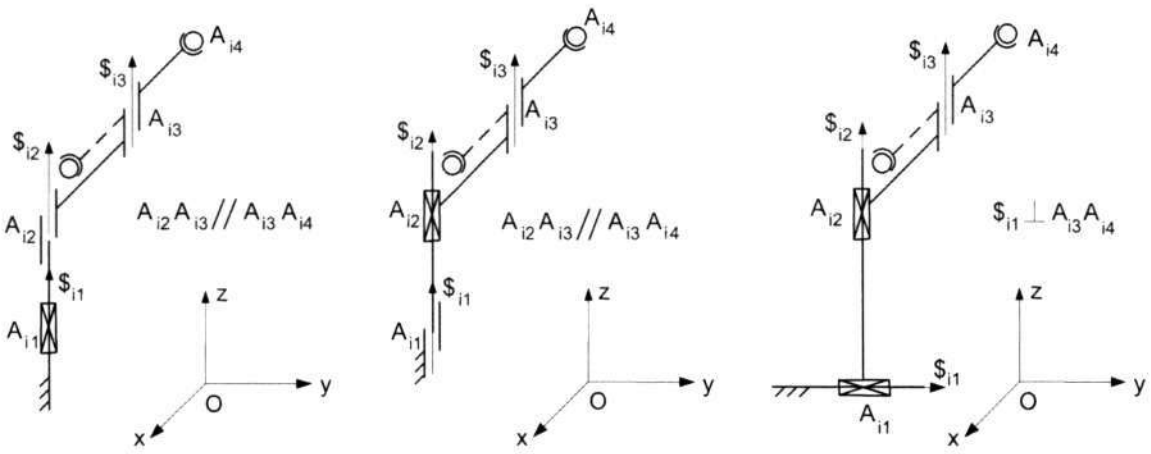

(a) 3-PRRS (b) 3-RPRS (c) 3-PPRS

Figure 3.8: Inverse singularity of PMs with decoupled 3-DOF planar motion and 3-DOF spatial motion

related wrenches (reciprocal screws). Each reciprocal screw can be regarded as a straight line in the Cartesian space. For the 3P3S PMs, the six reciprocal screws can be divided into two independent groups: one group including three lines parallel to the horizontal plane ($\$_{1r1}$, $\$_{2r1}$ and $\$_{3r1}$ for 3-RPPS PM), and the other group including three lines parallel to the vertical direction ($\$_{1r2}, \$_{2r2}$, and $\$_{3r2}$ for 3-RPPS PM). The forward singularity occurs when the order of the two groups reduces. Based on line geometry, the forward singular configuration can be enumerated directly. Taking the 3-RPPS PM for example, the forward singularity occurs if the three lines in group 2 share one common plane, i.e., the plane determined by points A_{14}, A_{24} and A_{34} is perpendicular to the horizontal plane. For the three lines in group 1, the forward singular configurations occur if and only if the three lines are parallel to each other or intersect at one common point. With the three lines in parallel as shown in Fig. 3.9(a), the moving platform will produce an infinitesimal translation along the line direction even though all actuators are locked. With the three lines intersection at a common point as shown in Fig. 3.9(b), the moving platform can produce rotations about that point even though all actuators are locked. Note that the singular configurations in Fig. 3.9 are projected onto the horizontal plane (the base plane).

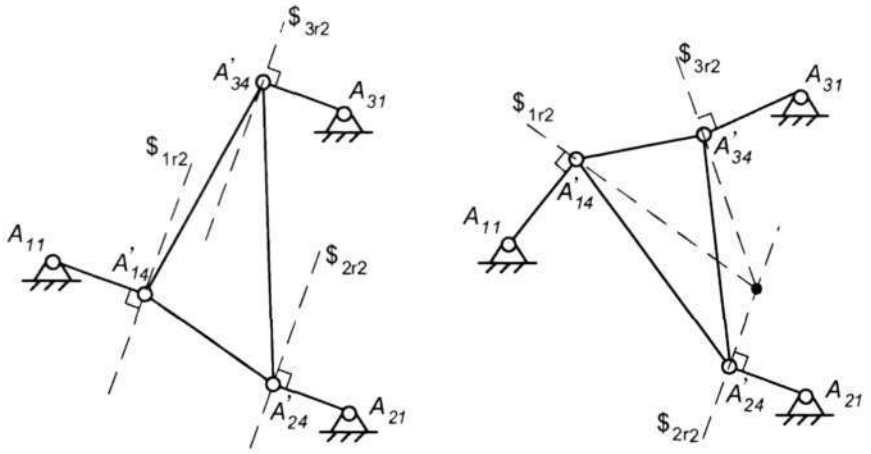

Figure 3.9: Forward singularities of the 3-RPPS PM

Combined Singularity

As no inverse singularity exists for the 3-RPPS PM, it has no combined singularity.

3.4 Summary

Both instantaneous kinematics and singularity conditions are analyzed for the SA-PM and 3P3S PMs. The instantaneous kinematics shows that the decoupling characteristics can be directly identified by the Jacobian matrix. Due to motion decoupling, the two Jacobian matrices (both inverse and forward Jacobian matrices) of rank six can be converted into four Jacobian matrices of rank three. The complexity of instantaneous kinematics and singularity analysis is significantly reduced. The inverse singularities, forward singularities and combined singularities are obtained for both the SA-PM and the 3P3S PMs. As a result, the SA-PM is an isotropic mechanism when the three actuators are mutually orthogonal and operating in linear motion. Singularity conditions of the SA-PM in complete six DOF motion are the same as the SA-PM in pure spherical motion. The inverse singularity depends on the location of the passive R-joint for these 3P3S PMs. The forward singularity conditions of 3P3S PMs are obtained. The results prove that the

decoupled motion structure can significantly simplify the instantaneous kinematics and singularity analysis.

Chapter 4

Inverse and Forward Kinematics

Kinematics (displacement) analysis is to find the relationship between the position (pose) of the end-effector and the displacements of the actuator. It is very important for robot design and analysis, and is the basis for workspace analysis, dimensional optimization, motion planing and control.

For parallel manipulators, displacement analysis is classified into two types, i.e., forward displacement analysis, in which it is to find the end-effector pose with given displacements of actuators, and inverse displacement analysis, in which the displacements of actuators is to be found with given end-effector pose. For a serial manipulator, the forward displacement is straight forward and the inverse displacement is difficult due to the multiple solutions. For the parallel manipulators, the inverse displacement is easy because it can be obtained once the platform pose is determined. And yet the forward displacement is generally very complicated as it requires solving higher order nonlinear equations. In this chapter, a decomposition method is applied to calculate displacements of the SA-PM because it has decoupled translation and orientation. For the 3P3S PMs, as the rotation of the end-effector about x- and y- axes will have influence on the planar motion (refer to eqn. (3.19)), the decomposition method is not suitable. Therefore, a projective method [110] is applied for the displacement analysis. As a result, closed-form solutions are obtained for both inverse and forward displacement of the SA-PM and the 3P3S PMs.

This chapter is organized as follows. Section 4.1 introduce the significant research on the displacement analysis of PMs. The algorithms of both inverse and forward displacement for the SA-PM and the 3P3S PMs are studied in Section 4.2 and Section 4.3 respectively.

4.1 Introduction

It is well known that forward kinematics of PMs is a difficult problem due to the highly non-linear equations and multiple solutions. A number of approaches for displacement analysis have been proposed in the literature [11, 16, 46, 48, 82, 89, 95, 108, 112, 114].

Wang and Chen [108] proposed a numerical approach to calculate the kinematics of general PMs. A two-step scheme is employed in this approach, i.e., structure analysis and displacement analysis. The structure information is firstly identified by using graph theory and the Depth First Search algorithm, which is used as the inputs of the second step. The displacement analysis is realized by an algorithm combining the cyclic coordinate descent method and Newton-Raphson method so that it is insensitive to the initial guess and has rapid convergence rate. However, only one solution can be obtained each time.

Raghavan [95] showed a numerical approach to solve the forward kinematics of the Stewart platform of general geometry. In this approach, a polynomial continuation technique is employed with random complex-valued parameters. As a result, there are 40 configurations for forward kinematics of the general Stewart platform.

Husty [46] presented an algorithm to solving the forward kinematics of fully parallel manipulators, which leaded to a 40th order polynomial equation of unique variable. However, the 40th order polynomial equation is computationally expensive and difficult to be implemented in real time.

Yang and Geng [114] proposed a forward kinematics algorithm for a class of hexapod manipulators, in which the shapes of the moving platform and the base are linearly

related. Based on this assumption, the algorithm can obtain closed-form solutions in a very rapid way which is suitable for real-time applications. As a result, at most eight solutions exist for the forward kinematics of this type of PMs.

Yang et al. [112] introduced two forward displacement algorithms based on the local POE formula for a class of 3-limb 6-DOF modular PMs, in which each limb had three main joint and a spherical joint supporting to the moving platform. However, only one solution can be obtained each time, and the numerical approach is sensitive to the initial approximation.

Some other researchers studied the forward kinematics of PMs with the help of additional sensors [11, 16, 89], by which the difficulty is significantly reduced so that the kinematic algorithm is suitable for the real-time applications.

4.2 Displacement Analysis of SA-PM

4.2.1 Frames of Reference and Vector Representation

According to singularity analysis, the base frame $\{O - xyz\}$ and the platform frame $\{O' - x'y'z'\}$ are redefined to simplify the kinematic model as shown in Fig. 4.1. The coordinates of the base frame $\{O - xyz\}$ are along three actuator axes respectively and point to the first passive prismatic joint. As the mechanism has a symmetrical design, the origin of the inertial frame is on the central normal of the triangle $A_{11}A_{21}A_{31}$. In addition, we take the $\{O' - x'y'z'\}$ coordinate system as the instantaneous reference frame with its origin located at the O'. The z'-coordinate axis is normal to the plane determined by three points A_{16}, A_{26}, A_{36} and pointing to the centroid M of the equilateral triangle $A_{16}A_{26}A_{36}$. The y'-axis is orthogonal to the z'-axis and in the plane determined by three points O', A_{16} and M, and has the opposite direction with vector $O'A_{15}$ in the home pose. The x'-axis can be obtained by the right-hand rule.

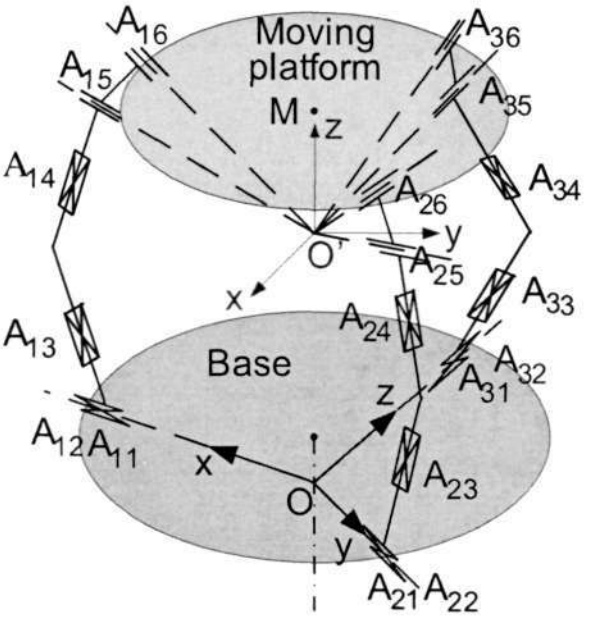

Figure 4.1: Schematic description the SA-PM

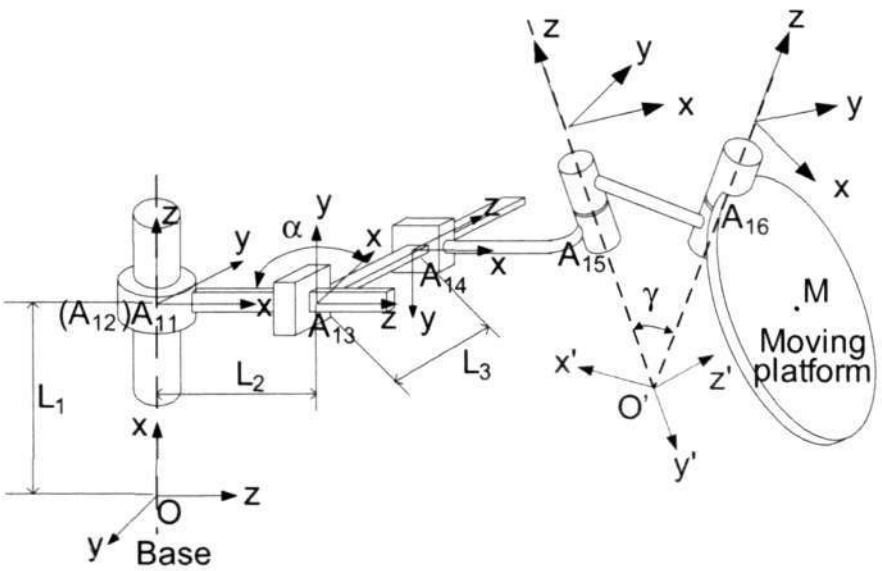

Figure 4.2: The first limb of the SA-PM

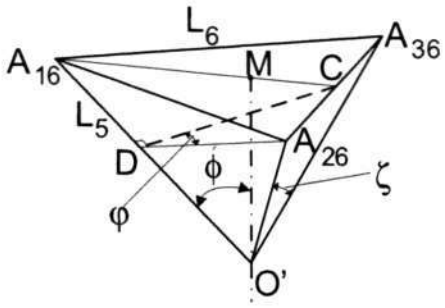

Figure 4.3: The geometry of the gripper link

Taking limb 1 as an example, the local frame associated with each link assembly is defined as shown in Fig. 4.2, which shows the initial configuration of the SA-PM ($\boldsymbol{\theta}_{ij} = 0$, $i = 1, 2, 3; j = 1, 2, \cdots, 6$). In this configuration, the two local frames $\{A_{i1}\}$ and $\{A_{i2}\}$ are coincident ($i = 1, 2, 3$), and the plane determined by vectors $\boldsymbol{O'A}_{i5}$ and $\boldsymbol{O'A}_{i6}$ is perpendicular to the plane determined by the three points A_{16}, A_{26} and A_{36}. Note that the origins of the two local frames $\{A_{i5}\}$ and $\{A_{i6}\}$ are both located at the common point O', and the x_{i6}-axis is on the plane determined by three points, namely, O', A_{i6} and M. Because of the symmetry, the local frames associated with each joint of limb 2 and 3 are defined in the same way as limb 1. The geometry of the moving platform (the end-effector) can be thought of as a pyramid with a triangular base ($A_{16}A_{26}A_{36}$) as shown in Fig. 4.3.

To describe the manipulator geometry, some notations are introduced below.

- L_1: the distance between origins of frame $\{A_{i1}\}$ and the base frame in the initial configuration;
- L_2: the distance between origins of frame $\{A_{i3}\}$ and $\{A_{i2}\}$ in initial configuration;
- L_3: the distance between origins of frame $\{A_{i4}\}$ and frame $\{A_{i3}\}$ in the initial configuration;
- α: the relative angle between s_{i3} and s_{i4};
- γ: the relative angle between s_{i5} and s_{i6};

- $[p_{4x}, p_{4y}, p_{4z}]$: the position of frame $\{A_{i5}\}$ relative to frame $\{A_{i4}\}$ in the initial configuration;
- $\begin{bmatrix} r_{11} & r_{12} & r_{13} \\ r_{21} & r_{22} & r_{23} \\ r_{31} & r_{32} & r_{33} \end{bmatrix}$: $\in SO(3)$, represents the orientation of frame $\{A_{i5}\}$ relative to frame $\{A_{i4}\}$ in the initial configuration;
- $\|\boldsymbol{O'A}_{16}\| = \|\boldsymbol{O'A}_{26}\| = \|\boldsymbol{O'A}_{36}\| = L_5$, where L_5 is a constant;
- $\|\boldsymbol{A}_{16}\boldsymbol{A}_{26}\| = \|\boldsymbol{A}_{16}\boldsymbol{A}_{36}\| = \|\boldsymbol{A}_{26}\boldsymbol{A}_{36}\| = L_6$, where L_6 is a constant;
- ς: the angle between $\boldsymbol{O'A}_{i6}$ and $\boldsymbol{O'A}_{j6}$, $(i \neq j;\ i, j = 1, 2, 3)$;
- ϕ: the angle between the last R-joint axis and the normal $\boldsymbol{O'M}$ of the plane determined by the equilateral triangle $A_{16}A_{26}A_{36}$,
- φ: the angle between two planes, namely, plane $O'A_{16}A_{26}$ and plane $O'A_{16}C$,
- $T_{OO'} = \begin{bmatrix} b_{11} & b_{12} & b_{13} & p_x \\ b_{21} & b_{22} & b_{23} & p_y \\ b_{31} & b_{32} & b_{33} & p_z \\ 0 & 0 & 0 & 1 \end{bmatrix}$: given end-effector pose.

Note that the geometry of the moving platform is fixed once L_5 and L_6 are given. The relationships are written as follows:

$$\sin(\varsigma/2) = L_6/(2L_5), \tag{4.1}$$

$$\sin\phi = \frac{2\sqrt{3}}{3}\sin(\varsigma/2), \tag{4.2}$$

$$\cos\varphi = \sqrt{3L_5^2 - L_6^2}/\sqrt{4L_5^2 - L_6^2}. \tag{4.3}$$

4.2.2 Inverse Displacement Analysis

Inverse kinematics is a mapping from the pose ($T_{OO'}$) of the moving platform into the actuator displacements (θ_{i1}, θ_{i2}). Referring to Fig. 4.2, the forward kinematic transformation from the base (O) to the end-effector (O') of the i^{th} limb is (note that $\hat{\mathbf{\$}}_{ij}$ here is

represented in its local frame [87]):

$$T_{OO'}(\theta_{i1}, \theta_{i2}, \ldots, \theta_{i6}) = T_{OA_{i1}} e^{\hat{\$}_{i1}\theta_{i1}} \ldots T_{A_{i5}A_{i6}}(0) e^{\hat{\$}_{i6}\theta_{i6}} T_{A_{i6}O'}(0), \tag{4.4}$$

where

$$T_{OA_{11}} = \begin{bmatrix} 0 & 0 & 1 & L_1 \\ 0 & -1 & 0 & 0 \\ 1 & 0 & 0 & 0 \\ 0 & 0 & 0 & 1 \end{bmatrix}, \quad T_{OA_{21}} = \begin{bmatrix} 1 & 0 & 0 & 0 \\ 0 & 0 & 1 & L_1 \\ 0 & -1 & 0 & 0 \\ 0 & 0 & 0 & 1 \end{bmatrix},$$

$$T_{OA_{31}} = \begin{bmatrix} 0 & -1 & 0 & 0 \\ 1 & 0 & 0 & 0 \\ 0 & 0 & 1 & L_1 \\ 0 & 0 & 0 & 1 \end{bmatrix}, \quad T_{A_{i1}A_{i2}}(0) = \begin{bmatrix} 1 & 0 & 0 & 0 \\ 0 & 1 & 0 & 0 \\ 0 & 0 & 1 & 0 \\ 0 & 0 & 0 & 1 \end{bmatrix},$$

$$T_{A_{i2}A_{i3}}(0) = \begin{bmatrix} 0 & 0 & 1 & L_2 \\ 1 & 0 & 0 & 0 \\ 0 & 1 & 0 & 0 \\ 0 & 0 & 0 & 1 \end{bmatrix},$$

$$T_{A_{i3}A_{i4}}(0) = \begin{bmatrix} -c\alpha & 0 & s\alpha & L_3 s\alpha \\ 0 & -1 & 0 & 0 \\ s\alpha & 0 & c\alpha & L_3 c\alpha \\ 0 & 0 & 0 & 1 \end{bmatrix},$$

where s represents sin, and c represents cos,

$$T_{A_{i4}A_{i5}}(0) = \begin{bmatrix} r_{11} & r_{12} & r_{13} & p_{4x} \\ r_{21} & r_{22} & r_{23} & p_{4y} \\ r_{31} & r_{32} & r_{33} & p_{4z} \\ 0 & 0 & 0 & 1 \end{bmatrix},$$

$$T_{A_{i5}A_{i6}}(0) = \begin{bmatrix} c\gamma & 0 & s\gamma & 0 \\ 0 & 1 & 0 & 0 \\ -s\gamma & 0 & c\gamma & 0 \\ 0 & 0 & 0 & 1 \end{bmatrix},$$

$$T_{A_{16}O'}(0) = \begin{bmatrix} 0 & c\phi & s\phi & 0 \\ -1 & 0 & 0 & 0 \\ 0 & -s\phi & c\phi & 0 \\ 0 & 0 & 0 & 1 \end{bmatrix},$$

$$T_{A_{26}O'}(0) = \begin{bmatrix} c\phi \cdot c(5\pi/6) & -c\phi \cdot s(5\pi/6) & s\phi & 0 \\ s(5\pi/6) & c(5\pi/6) & 0 & 0 \\ -s\phi \cdot c(5\pi/6) & s\phi \cdot s(5\pi/6) & c\phi & 0 \\ 0 & 0 & 0 & 1 \end{bmatrix},$$

$$T_{A_{36}O'}(0) = \begin{bmatrix} c\phi \cdot c(\pi/6) & -c\phi \cdot s(\pi/6) & s\phi & 0 \\ s(\pi/6) & c(\pi/6) & 0 & 0 \\ -s\phi \cdot c(\pi/6) & s\phi \cdot s(\pi/6) & c\phi & 0 \\ 0 & 0 & 0 & 1 \end{bmatrix}.$$

As the translations and rotations of the PM are decoupled, the position and orientation of the end-effector can be computed respectively. Applying the *position preservation* [23] technique, i.e., the position of the point O' will be preserved under the rotation of $\hat{\mathbf{S}}_{i5}$ and $\hat{\mathbf{S}}_{i6}$ as point O' is the intersecting point of two revolute joints, eqn. (4.4) can be reduced. Let $\boldsymbol{p}_{O'}$ represents the position vector of point O' in $\mathbb{R}^3$ with respect to the base frame, and Let $\boldsymbol{p}_{i6}$ represents the position vector of point O' in $\mathbb{R}^3$ with respect to the frame $\{A_{i6}\}$, we have $\boldsymbol{p}_{i6} = [0 \quad 0 \quad 0]^T$. Let $\bar{\boldsymbol{p}}_{O'} = \begin{bmatrix} \boldsymbol{p}_{O'} \\ 1 \end{bmatrix}$ and $\bar{\boldsymbol{p}}_{i6} = \begin{bmatrix} \boldsymbol{p}_{i6} \\ 1 \end{bmatrix}$, then

$$\bar{\boldsymbol{p}}_{O'} = T_{AA_{i1}}(0)e^{\hat{\mathbf{S}}_{i1}\theta_{i1}} \ldots T_{A_{i4}A_{i5}}(0)\bar{\boldsymbol{p}}_{i6}. \tag{4.5}$$

After computing for limb 1, 2 and 3, we have

$$\bar{\boldsymbol{p}}_{O'} = \begin{bmatrix} K_1 \\ f_1(\theta_{13}, \theta_{14}) \\ f_2(\theta_{13}, \theta_{14}) \\ 1 \end{bmatrix} = \begin{bmatrix} f_3(\theta_{23}, \theta_{24}) \\ K_2 \\ f_4(\theta_{23}, \theta_{24}) \\ 1 \end{bmatrix} = \begin{bmatrix} f_5(\theta_{33}, \theta_{34}) \\ f_6(\theta_{33}, \theta_{34}) \\ K_3 \\ 1 \end{bmatrix} \tag{4.6}$$

where

$$K_1 = \theta_{12} - p_{4y} + L_1,$$

$$K_2 = \theta_{22} - p_{4y} + L_1,$$

$$K_3 = \theta_{32} - p_{4y} + L_1,$$

$$\begin{aligned} f_1(\theta_{13}, \theta_{14}) = {} & -s\theta_{11} \cdot \theta_{13} - s(\theta_{11} + \alpha) \cdot \theta_{14} + c(\theta_{11} + \alpha) \cdot p_{4x} - s(\theta_{11} + \alpha) \cdot p_{4z} \\ & - c\theta_{11} \cdot s\alpha \cdot L_3 - s\theta_{11} \cdot c\alpha \cdot L_3 - s\theta_{11} \cdot L_2, \end{aligned}$$

$$\begin{aligned} f_2(\theta_{13}, \theta_{14}) = {} & c\theta_{11} \cdot \theta_{13} + c(\theta_{11} + \alpha) \cdot \theta_{14} + s(\theta_{11} + \alpha) \cdot p_{4x} + c(\theta_{11} + \alpha) \cdot p_{4z} \\ & - s\theta_{11} \cdot s\alpha \cdot L_3 + c\theta_{11} \cdot c\alpha \cdot L_3 - c\theta_{11} \cdot L_2, \end{aligned}$$

$$\begin{aligned} f_3(\theta_{23}, \theta_{24}) = {} & c\theta_{21} \cdot \theta_{23} + c(\theta_{21} + \alpha) \cdot \theta_{24} + s(\theta_{21} + \alpha) \cdot p_{4x} + c(\theta_{21} + \alpha) \cdot p_{4z} \\ & - s\theta_{21} \cdot s\alpha \cdot L_3 + c\theta_{21} \cdot c\alpha \cdot L_3 - c\theta_{21} \cdot L_2, \end{aligned}$$

$$\begin{aligned} f_4(\theta_{23}, \theta_{24}) = {} & -s\theta_{21} \cdot \theta_{23} - s(\theta_{21} + \alpha) \cdot \theta_{24} + c(\theta_{21} + \alpha) \cdot p_{4x} - s(\theta_{21} + \alpha) \cdot p_{4z} \\ & - c\theta_{21} \cdot s\alpha \cdot L_3 - s\theta_{21} \cdot c\alpha \cdot L_3 - s\theta_{21} \cdot L_2, \end{aligned}$$

$$\begin{aligned} f_5(\theta_{33}, \theta_{34}) = {} & -s\theta_{31} \cdot \theta_{33} - s(\theta_{31} + \alpha) \cdot \theta_{34} + c(\theta_{31} + \alpha) \cdot p_{4x} - s(\theta_{31} + \alpha) \cdot p_{4z} \\ & - c\theta_{31} \cdot s\alpha \cdot L_3 - s\theta_{31} \cdot c\alpha \cdot L_3 - s\theta_{31} \cdot L_2, \end{aligned}$$

$$\begin{aligned} f_6(\theta_{33}, \theta_{34}) = {} & c\theta_{31} \cdot \theta_{33} + c(\theta_{31} + \alpha) \cdot \theta_{34} + s(\theta_{31} + \alpha) \cdot p_{4x} + c(\theta_{31} + \alpha) \cdot p_{4z} \\ & - s\theta_{31} \cdot s\alpha \cdot L_3 + c\theta_{31} \cdot c\alpha \cdot L_3 - c\theta_{31} \cdot L_2. \end{aligned}$$

With a given end-effector pose $T_{OO'}$, (based on eqn.(4.6)), the linear displacements of actuators can be computed directly as follows:

$$\theta_{12} = p_x + p_{4y} - L_1, \tag{4.7}$$

$$\theta_{22} = p_y + p_{4y} - L_1, \tag{4.8}$$

$$\theta_{32} = p_z + p_{4y} - L_1. \tag{4.9}$$

Equations (4.7)$\sim$(4.9) show that the linear displacement of each actuator can be directly computed using the position vector of the end-effector. To compute the orientation of the moving platform, let $\bar{\boldsymbol{s}}_{ij} = \begin{bmatrix} \boldsymbol{s}_{ij} \\ 0 \end{bmatrix}$, $(i = 1, 2, 3; j = 5, 6)$, we have

$$\bar{\boldsymbol{s}}_{i5} = T_{A,A_{i1}}(0) e^{\hat{\$}_{i1}\theta_{i1}} \dots T_{A_{i4},A_{i5}}(0) \left[\bar{\boldsymbol{s}}_{i5}\right]^{A_{i5}}. \tag{4.10}$$

After computing for each limb, we have

$$\bar{\boldsymbol{s}}_{15} = \begin{bmatrix} -r_{23} \\ c(\theta_{i1}+\alpha)\cdot r_{13} - s(\theta_{i1}+\alpha)\cdot r_{33} \\ s(\theta_{i1}+\alpha)\cdot r_{13} + c(\theta_{i1}+\alpha)\cdot r_{33} \\ 0 \end{bmatrix},$$

$$\bar{\boldsymbol{s}}_{25} = \begin{bmatrix} s(\theta_{i1}+\alpha)\cdot r_{13} + c(\theta_{i1}+\alpha)\cdot r_{33} \\ -r_{23} \\ c(\theta_{i1}+\alpha)\cdot r_{13} - s(\theta_{i1}+\alpha)\cdot r_{33} \\ 0 \end{bmatrix},$$

$$\bar{\boldsymbol{s}}_{35} = \begin{bmatrix} c(\theta_{i1}+\alpha)\cdot r_{13} - s(\theta_{i1}+\alpha)\cdot r_{33} \\ s(\theta_{i1}+\alpha)\cdot r_{13} + c(\theta_{i1}+\alpha)\cdot r_{33} \\ -r_{23} \\ 0 \end{bmatrix}.$$

According to the geometry of the moving platform, $\boldsymbol{s}_{i6}$ can be easily expressed with respect to frame O' as follows:

$$\left[\boldsymbol{s}_{16}\right]^{O'} = \begin{bmatrix} 0 \\ -s\phi \\ c\phi \end{bmatrix}, \quad \left[\boldsymbol{s}_{26}\right]^{O'} = \begin{bmatrix} s\phi\cdot s(\pi/3) \\ s\phi\cdot c(\pi/3) \\ c\phi \end{bmatrix},$$

$$\left[\boldsymbol{s}_{36}\right]^{O'} = \begin{bmatrix} -s\phi\cdot s(\pi/3) \\ s\phi\cdot c(\pi/3) \\ c\phi \end{bmatrix}.$$

With the given end-effector pose $T_{OO'}$, $\bar{\boldsymbol{s}}_{i6}$ with respect to the base frame A can be written as:

$$\bar{\boldsymbol{s}}_{i6} = T_{OO'} \left[\bar{\boldsymbol{s}}_{i6}\right]^{O'}. \tag{4.11}$$

We can then write the closure equation as follows:

$$\bar{\boldsymbol{s}}_{i5} \cdot \bar{\boldsymbol{s}}_{i6} = \cos\gamma, \tag{4.12}$$

which, for each limb, leads to a trigonometric function equation of the form

$$A_{i1} \cdot s(\theta_{i1} + \alpha) + A_{i2} \cdot c(\theta_{i1} + \alpha) + A_{i3} = 0, \qquad (i = 1, 2, 3), \tag{4.13}$$

where A_{ij} (i=1, 2, 3; j=1, 2, 3) are constants, and their expressions are as follows.

$$A_{11} = (b_{22}s\phi - b_{23}c\phi)r_{33} + (-b_{32}s\phi + b_{33}c\phi)r_{13},$$

$$A_{12} = (-b_{22}s\phi + b_{23}c\phi)r_{13} + (-b_{32}s\phi + b_{33}c\phi)r_{33},$$

$$A_{13} = (b_{12}s\phi - b_{13}c\phi)r_{23} - c(\gamma),$$

$$A_{21} = (b_{11}s\phi \cdot s(\pi/3) + b_{12}s\phi \cdot c(\pi/3) + b_{13}c\phi)r_{13} - (b_{31}s\phi \cdot s(\pi/3) + b_{32}s\phi \cdot c(\pi/3) + b_{33}c\phi)r_{33},$$

$$A_{22} = (b_{11}s\phi \cdot s(\pi/3) + b_{12}s\phi \cdot c(\pi/3) + b_{13}c\phi)r_{33} + (b_{31}s\phi \cdot s(\pi/3) + b_{32}s\phi \cdot c(\pi/3) + b_{33}c\phi)r_{13},$$

$$A_{23} = -(b_{21}s\phi \cdot s(\pi/3) + b_{22}s\phi \cdot c(\pi/3) + b_{23}c\phi)r_{23} - c(\gamma),$$

$$A_{31} = (b_{11}s\phi \cdot s(\pi/3) - b_{12}s\phi \cdot c(\pi/3) - b_{13}c\phi)r_{33} + (-b_{21}s\phi \cdot s(\pi/3) + b_{22}s\phi \cdot c(\pi/3) + b_{23}c\phi)r_{13},$$

$$A_{32} = (-b_{11}s\phi \cdot s(\pi/3) + b_{12}s\phi \cdot c(\pi/3) + b_{13}c\phi)r_{13} + (-b_{21}s\phi \cdot s(\pi/3) + b_{22}s\phi \cdot c(\pi/3) + b_{23}c\phi)r_{33},$$

$$A_{33} = -(-b_{31}s\phi \cdot s(\pi/3) + b_{32}s\phi \cdot c(\pi/3) + b_{33}c\phi)r_{23} - c(\gamma).$$

Assume that $x_{i1} = \tan((\theta_{i1} + \alpha)/2)$, eqn. (4.13) can be written as:

$$(A_{i3} - A_{i2})x_{i1}^2 + 2A_{i1}x_{i1} + A_{i2} + A_{i3} = 0. \tag{4.14}$$

The symbolic solutions of $x_{i1}, (i = 1, 2, 3)$, can be directly obtained as

$$x_{i1} = (A_{i1} \pm \sqrt{A_{i1}^2 + A_{i2}^2 - A_{i3}^2})/(A_{i2} - A_{i3}). \tag{4.15}$$

Therefore,

$$\theta_{i1} = 2\arctan(x_{i1}) - \alpha. \tag{4.16}$$

Obviously, at most two solutions exist for the given end-effector pose in each limb. Hence, there are eight solutions at most for the inverse kinematics of the PM.

4.2.3 Forward Displacement Analysis

Forward kinematics is to find the possible pose of the end-effector with given actuator displacements. It will be helpful for determining assembly modes and off-line simulation. With given actuator displacements, based on eqn. (4.6), K_1, K_2 and K_3 are constants, the position of the moving platform can be directly obtained as follows:

$$p_x = \theta_{12} - p_{4y} + L_1, \tag{4.17}$$

$$p_y = \theta_{22} - p_{4y} + L_1, \tag{4.18}$$

$$p_z = \theta_{32} - p_{4y} + L_1. \tag{4.19}$$

The results show that each element of the position of the end-effector is directly controlled by an actuator. In other words, the PM is isotropic when all the actuators are in linear mode.

To solve the orientation of the end-effector, we can treat the PM as a virtual wrist with only rotary joints as the displacements of prismatic joints (including actuator) will not affect the orientation of the end-effector (without considering the joint limits here). Hence, we employ a similar way suggested by Gosselin [28] to calculate the orientation of the end-effector. In order to simplify the expressions, frame $\{O'\text{-}x'y'z'\}$ will be defined again as follows: the z'- coordinate axis is aligned with the last R-joint axis of limb 1, the x'-axis is orthogonal to the z'-axis and in the plane determined by two vectors, namely, $\boldsymbol{O'A_{16}}$ and $\boldsymbol{O'A_{26}}$ and the y'-axis is obtained by the right-hand rule. The transformation from the original frame $\{O'\text{-}x'y'z'\}$ to the new frame $\{O'\text{-}x'y'z'\}$ is written as:

$$T = \begin{bmatrix} s\varphi & -c\varphi & 0 & 0 \\ c\phi \cdot c\varphi & c\phi \cdot s\varphi & -s\varphi & 0 \\ s\phi \cdot c\varphi & s\phi \cdot s\varphi & s\varphi & 0 \\ 0 & 0 & 0 & 1 \end{bmatrix}. \tag{4.20}$$

In the following part, the new frame $\{O'\text{-}x'y'z'\}$ will be used for the orientation of SA-PM. Also in order to simplifying the expressions, the frame $\{O'\text{-}x'y'z'\}$ is represented by Z-Y-Z Euler angles with respect to frame $\{A_{15}\text{-}x_{15}y_{15}z_{15}\}$ as shown in Fig. 4.4. The Z-Y-Z

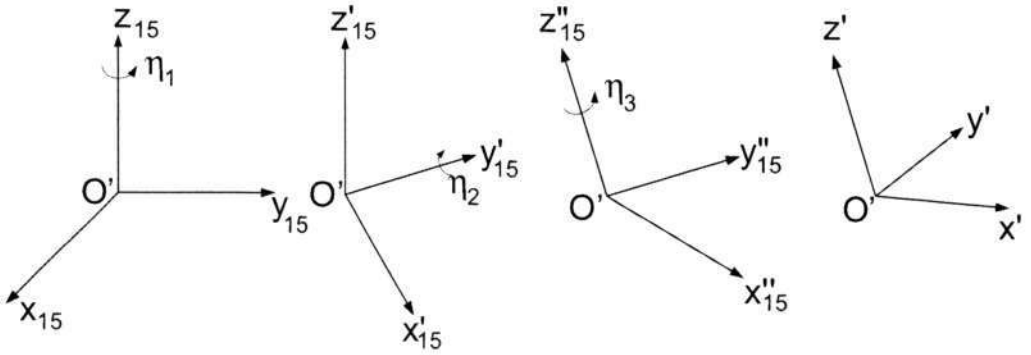

Figure 4.4: Z-Y-Z Euler angles from frame $\{A_{15}\}$ to frame $\{O'\}$

Euler angles associated with the rotation from frame $\{A_{15}\text{-}x_{15}y_{15}z_{15}\}$ to frame $\{O'\text{-}x'y'z'\}$ are defined as follows: first, a rotation of angle η_1 about z_{15}-axis which will bring axis x_{15} in the plane defined by z_{15}- and z'- axes; then, a rotation of angle η_2 about y'_{15}-axis (obtained from the previous rotation) which will bring z_{15}-axis in coincidence with z'-axis; and, finally, a rotation of angle η_3 around z'-axis which will bring x''_{15}-axis (obtained from the previous rotation) in coincidence with x'-axis. The corresponding rotation matrices, written in local coordinate frames can easily be written as:

$$R_1 = \begin{bmatrix} c\eta_1 & -s\eta_1 & 0 \\ s\eta_1 & c\eta_1 & 0 \\ 0 & 0 & 1 \end{bmatrix}, \quad R_2 = \begin{bmatrix} c\eta_2 & 0 & s\eta_2 \\ 0 & 1 & 0 \\ -s\eta_2 & 0 & c\eta_1 \end{bmatrix}, \quad R_3 = \begin{bmatrix} c\eta_3 & -s\eta_3 & 0 \\ s\eta_3 & c\eta_3 & 0 \\ 0 & 0 & 1 \end{bmatrix}.$$

Hence, the rotation from frame $\{A_{15}\text{-}x_{15}y_{15}z_{15}\}$ to frame $\{O'\text{-}x'y'z'\}$ is written as

$$R = R_1R_2R_3 = \begin{bmatrix} c_{11} & c_{12} & c_{13} \\ c_{21} & c_{22} & c_{23} \\ c_{31} & c_{32} & c_{33} \end{bmatrix} \tag{4.21}$$

where

$c_{11} = -s\eta_1 \cdot s\eta_3 + c\eta_1 \cdot c\eta_2 \cdot c\eta_3$,$c_{12} = -c\eta_3 \cdot s\eta_1 - c\eta_1 \cdot s\eta_3 \cdot c\eta_2$,

$c_{13} = c\eta_1 \cdot s\eta_2$, $c_{21} = c\eta_1 \cdot s\eta_3 + c\eta_3 \cdot s\eta_1 \cdot c\eta_2$,

$c_{22} = c\eta_1 \cdot c\eta_3 - s\eta_1 \cdot s\eta_3 \cdot c\eta_2$, $c_{23} = s\eta_1 \cdot s\eta_2$,

$c_{31} = -c\eta_3 \cdot s\eta_2$,$c_{32} = s\eta_3 \cdot s\eta_2$,$c_{33} = c\eta_2$.

For forward kinematics, the geometrical constraints that the three limbs are coupled to a common moving platform should be expressed. To this end, the unit vectors $\boldsymbol{s}_{16}$, $\boldsymbol{s}_{26}$ and

$\boldsymbol{s}_{36}$ are expressed in a common frame $\{O'\text{-}x'y'z'\}$, which are written as:

$$[\boldsymbol{s}_{16}]^{O'} = \begin{bmatrix} 0 \\ 0 \\ 1 \end{bmatrix} \quad [\boldsymbol{s}_{26}]^{O'} = \begin{bmatrix} s\varsigma \\ 0 \\ c\varsigma \end{bmatrix} \quad [\boldsymbol{s}_{36}]^{O'} = \begin{bmatrix} c\beta \cdot s(\varsigma/2) \\ s\beta \\ c\beta \cdot c(\varsigma/2) \end{bmatrix}$$

where $\beta = \arcsin(\frac{2s(\varsigma/2)}{\sqrt{3}}) + \arctan(\frac{s(\varsigma/2)}{\sqrt{3-4s(\varsigma/2)^2}})$. Let

$$T_{i15} = T_{A,A_{i1}} e^{\hat{\$}_{i1}\theta_{i1}} \ldots T_{A_{i4},A_{i5}}(0) = \begin{bmatrix} R_{i15} & \boldsymbol{P}_{i15} \\ \boldsymbol{0} & 1 \end{bmatrix}, (i = 1, 2, 3), \tag{4.22}$$

the vector $\boldsymbol{s}_{i6}$, with respect to the base frame, can be written as:

$$\boldsymbol{s}_{i6} = R_{115} R [\boldsymbol{s}_{i6}]^{O'}, \qquad (i = 1, 2, 3). \tag{4.23}$$

The vector $\boldsymbol{s}_{i5}$, with respect to the base frame A, can be written as:

$$\boldsymbol{s}_{i5} = R_{i15} [\boldsymbol{s}_{i5}]^{A_{i5}}, \qquad (i = 1, 2, 3). \tag{4.24}$$

Therefore, the geometric constraints to be specified for the closure of the kinematic loops are:

$$\boldsymbol{s}_{i5} \cdot \boldsymbol{s}_{i6} = c\gamma, \qquad (i = 1, 2, 3). \tag{4.25}$$

Substituting eqn. (4.23) and eqn. (4.24) into eqn. (4.25) will lead to three nonlinear algebraic equations in η_1, η_2 and η_3. As a result, one of the three equations can be simplified as:

$$\cos\eta_2 = \cos\gamma. \tag{4.26}$$

Hence, the angle η_2 can be solved directly, and the other two equations can be written as:

$$C_1 \cdot s\eta_1 + C_2 \cdot c\eta_1 + C_3 = 0, \tag{4.27}$$

$$D_1 \cdot s\eta_1 + D_2 \cdot c\eta_1 + D_3 = 0. \tag{4.28}$$

where

$C_1 = -B_1 \cdot s\eta_3 + B_2 \cdot c\eta_3 \cdot c\eta_2 + B_5 \cdot s\eta_2,$

$C_2 = B_1 \cdot c\eta_3 \cdot c\eta_2 + B_2 \cdot s\eta_3 + B_4 \cdot s\eta_2,$

$C_3 = -B_3 \cdot c\eta_3 \cdot s\eta_2 + B_6 \cdot c\eta_2 - c\eta_2,$

$R_{115} = [d_{ij}], (i, j = 1, 2, 3),$

$B_1 = (-d_{13}d_{31} + d_{33}d_{21} + d_{23}d_{11}) \cdot s\varsigma,$

$B_2 = (-d_{13}d_{32} + d_{33}d_{22} + d_{23}d_{12}) \cdot s\varsigma,$

$B_3 = (-d_{13}d_{33} + d_{33}d_{23} + d_{23}d_{13}) \cdot s\varsigma,$

$B_4 = (-d_{13}d_{31} + d_{33}d_{21} + d_{23}d_{11}) \cdot c\varsigma,$

$B_5 = (-d_{13}d_{32} + d_{33}d_{22} + d_{23}d_{12}) \cdot c\varsigma,$

$B_6 = (-d_{13}d_{33} + d_{33}d_{23} + d_{23}d_{13}) \cdot c\varsigma,$

$D_1 = -E_1 \cdot s\eta_3 + E_2 \cdot c\eta_3 \cdot c\eta_2 - E_4 \cdot c\eta_3 - E_5 \cdot s\eta_3 \cdot c\eta_2 + E_8 \cdot s\eta_2,$

$D_2 = E_1 \cdot c\eta_3 \cdot c\eta_2 + E_2 \cdot s\eta_3 - E_4 \cdot s\eta_3 \cdot c\eta_2 + E_5 \cdot c\eta_3 + E_7 \cdot s\eta_2,$

$D_3 = -E_3 \cdot c\eta_3 \cdot s\eta_2 + E_6 \cdot s\eta_3 \cdot s\eta_2 + E_9 \cdot c\eta_2 - c\eta_2.$

$E_1 = (-d_{23}d_{31} - d_{13}d_{21} + d_{33}d_{11}) \cdot c\beta \cdot s(\varsigma/2),$

$E_2 = (-d_{23}d_{32} - d_{13}d_{22} + d_{33}d_{12}) \cdot c\beta \cdot s(\varsigma/2),$

$E_3 = (-d_{23}d_{33} - d_{13}d_{23} + d_{33}d_{13}) \cdot c\beta \cdot s(\varsigma/2),$

$E_4 = (-d_{23}d_{31} - d_{13}d_{21} + d_{33}d_{11}) \cdot s\beta,$

$E_5 = (-d_{23}d_{32} - d_{13}d_{22} + d_{33}d_{12}) \cdot s\beta,$

$E_6 = (-d_{23}d_{33} - d_{13}d_{23} + d_{33}d_{13}) \cdot s\beta,$

$E_7 = (-d_{23}d_{31} - d_{13}d_{21} + d_{33}d_{11}) \cdot c\beta \cdot c(\varsigma/2),$

$E_8 = (-d_{23}d_{32} - d_{13}d_{22} + d_{33}d_{12}) \cdot c\beta \cdot c(\varsigma/2),$

$E_9 = (-d_{23}d_{33} - d_{13}d_{23} + d_{33}d_{13}) \cdot c\beta \cdot c(\varsigma/2).$

Combining eqn. (4.27) and eqn. (4.28), $s\eta_1$ and $c\eta_1$ can be solved as follows:

$$s\eta_1 = (-C_2D_3 + C_3D_2)/(C_2D_1 - C_1D_2),$$

$$c\eta_1 = (C_1D_3 - C_3D_1)/(C_2D_1 - C_1D_2).$$

Substituting above two equations into the following trigonometric identity

$$s\eta_1^2 + c\eta_1^2 = 1, \tag{4.29}$$

Table 4.1: Geometric data of SA-PM

L_1	L_2	L_3	L_5	L_6	p_{4x}	p_{4y}	p_{4z}	α	β_1	β_2	β_3	γ
30	30	30	30	30	50	30	-30	$\pi/2$	$\pi/18$	$5\pi/6$	π	$\pi/3$

which leads to an equation containing only one unknown, namely angle η_3. The equation is written as:

$$C_1^2D_2^2 + C_2^2D_1^2 + C_2^2D_3^2 + C_3^2D_2^2 + C_1^2D_3^2 + C_3^2D_1^2 \\ -2C_1C_2D_1D_2 - 2C_2C_3D_2D_3 - 2C_1C_3D_1D_3 = 0 \tag{4.30}$$

with the following condition:

$$C_2D_1 - C_1D_2 \neq 0. \tag{4.31}$$

Assume that

$$s\eta_3 = 2y/(1+y^2), \qquad c\eta_3 = (1-y^2)/(1+y^2),$$

where $y = \tan(\eta_3/2)$, after simplification, eqn. (4.30) can be written in the following form.

$$\sum_{i=0}^{8} k_i y^i = 0, \tag{4.32}$$

where $y = \tan(\eta_3/2)$, the coefficients k_i $(i = 0, 1, \cdots, 8)$ are functions of the geometric parameters of the PM and the actuator displacements. Clearly, there are at most eight solutions for the forward kinematics of this PM. A numerical example of the forward kinematics is shown in Tables 4.1, 4.2 and 4.3. Table 4.1 shows the geometry parameters of the SA-PM. Given the rotary displacements (Table 4.2) of the three actuators, eight real orientation solutions are obtained for the forward kinematics, as shown in Table 4.3. Note that eqn. (4.32) may not have eight real solutions for some sets of rotary displacements of actuators. As a result, there are at most eight solutions for the forward kinematics of the SA-PM.

Table 4.2: Rotary displacements of actuators

θ_{11}	θ_{21}	θ_{31}
$\pi/12$	$\pi/18$	$\pi/15$

Table 4.3: Eight orientation solutions of forward kinematics

No.	y	η_1	η_2	η_3
1	-18.9867	2.3714	$\pi/3$	-3.0364
2	-0.7722	3.0047	$\pi/3$	-1.3151
3	-0.5739	2.7512	$\pi/3$	-1.0420
4	-0.2533	0.8348	$\pi/3$	-0.4962
5	0.1754	0.1080	$\pi/3$	0.3473
6	1.1473	0.9730	$\pi/3$	1.7078
7	2.0807	4.6859	$\pi/3$	2.2456
8	10.3226	4.7820	$\pi/3$	2.9484

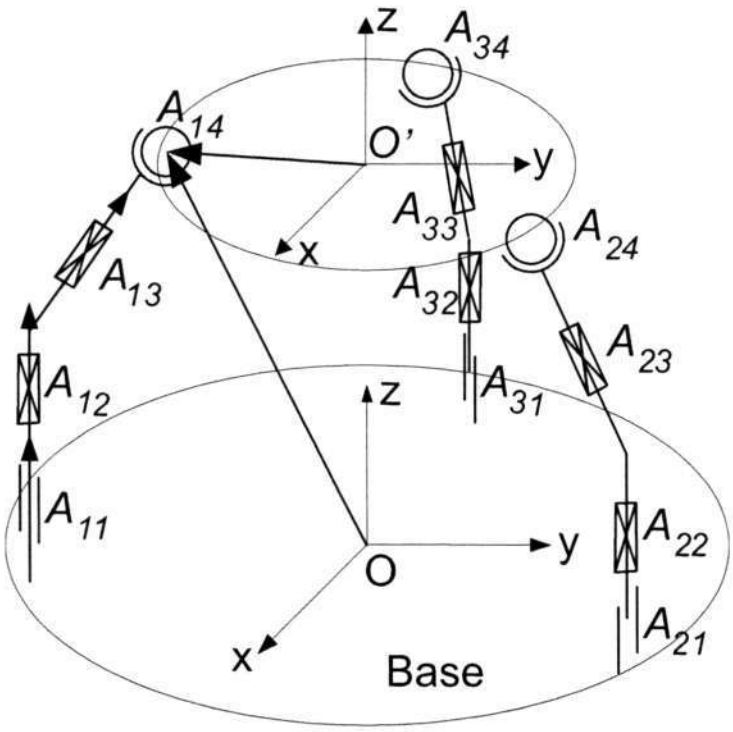

Figure 4.5: Schematic description of the 3-RPPS PM

4.3 Displacement Analysis of 3P3S PMs

Based on the kinematic features of the 3P3S PMs such that one actuator is linear and perpendicular to the base plane, a projective approach can be used to simplify the analysis.

By projecting these 3P3S PMs onto the base plane, i.e., the {O-xy} plane, the 6-DOF decoupled PMs will become 3-DOF planar ones (3-RRR, 3-RPR, 3-PRR and 3-PPR). Take the 3-RPPS structure as an example, the inverse and forward displacements are analyzed as follows.

4.3.1 Inverse Displacement Analysis

The inverse displacement analysis is to find the actuator displacements $(\theta_{i1}, \theta_{i2})$ by given the end-effector pose $T_{OO'}$. According to the geometry of the end-effector, the position vector of the point A_{i4} with respect to the base frame can be directly obtained by

$$\boldsymbol{OA}_{i4} = \boldsymbol{OO'} + T_{OO'} \cdot [\boldsymbol{O'A}_{i4}]^{O'}. \tag{4.33}$$

where $[\boldsymbol{O'A}_{i4}]^{O'}$ is the vector relative to the end-effector frame, all other vectors is with respect to the base frame. Therefore, each of the three limbs can be regarded as a RPP type serial chain as shown in Fig. 4.6. By projecting the limb onto the vertical plane (Fig. 4.6(a)), the displacement of the linear actuator can be directly computed by

$$\theta_{i2} = z_{i4} - h. \tag{4.34}$$

where h is the lowest position (zero position) of the linear actuator. By projecting the limb onto the base plane (Fig. 4.6(b)), the displacement of the rotary actuator can be calculated by

$$\cos\theta_{i1} = \boldsymbol{OA}_{i1} \cdot \boldsymbol{A}_{i1}\boldsymbol{A}'_{i4} / (\|\boldsymbol{OA}_{i1}\| \cdot \|\boldsymbol{A}_{i1}\boldsymbol{A}'_{i4}\|) \ for \ \|\boldsymbol{A}_{i1}\boldsymbol{A}'_{i4}\| \neq 0. \tag{4.35}$$

Therefore, we have

$$\theta_{i1} = \pm \arccos(\boldsymbol{OA}_{i1} \cdot \boldsymbol{A}_{i1}\boldsymbol{A}'_{i4} / (\|\boldsymbol{OA}_{i1}\| \cdot \|\boldsymbol{A}_{i1}\boldsymbol{A}'_{i4}\|)). \tag{4.36}$$

As a result, there are at most two solutions of each limb, and at most eight solutions exist for the inverse kinematics of the 3-RPPS PM.

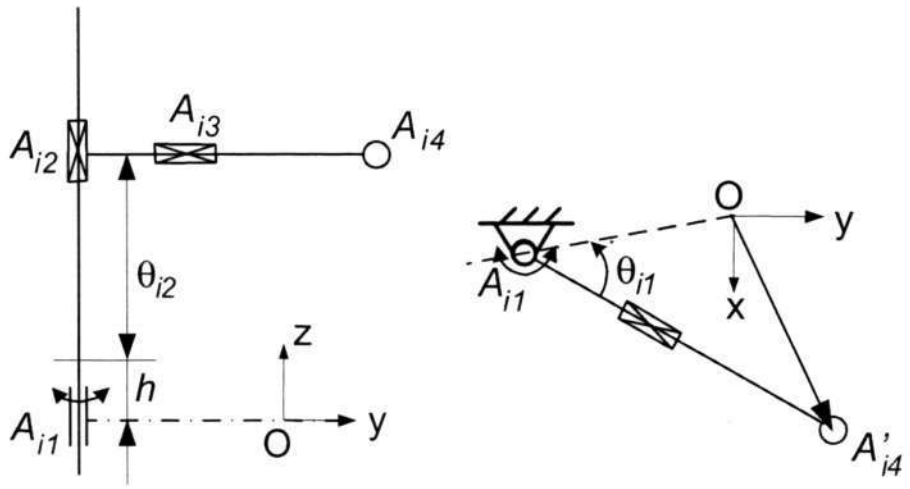

(a) front view (b) top view

Figure 4.6: The ith limb of 3-RPPS PM

4.3.2 Forward Displacement Analysis

Forward kinematics is to find the end-effector pose when all actuator displacements θ_{i1} and θ_{i2} (i=1, 2, 3), are known. A similar approach with [110] is employed to solve the forward kinematics here. Let $T_{OO'} \in SE(3)$ represents the end-effector pose with respect to the base frame $\{O - xyz\}$, then

$$T_{OO'} \begin{bmatrix} [\boldsymbol{OA}_{i4}]^{O'} \\ 1 \end{bmatrix} = \begin{bmatrix} [\boldsymbol{OA}_{i4}]^{O} \\ 1 \end{bmatrix}, \quad (i = 1, 2, 3), \tag{4.37}$$

where $[\boldsymbol{OA}_{i4}]^{O'}$ and $[\boldsymbol{OA}_{i4}]^{O}$ represent respectively the vector $\boldsymbol{OA}_{i4}$ with respect to the end-effector frame $\{O'\text{-}xyz\}$ and the base frame $\{O\text{-}xyz\}$. Since both these two frames are right-hand Cartesian coordinate frames, we have

$$T_{OO'} \begin{bmatrix} [\boldsymbol{A}_{14}\boldsymbol{A}_{24}]^{O'} \times [\boldsymbol{A}_{24}\boldsymbol{A}_{34}]^{O'} \\ 0 \end{bmatrix} = \begin{bmatrix} [\boldsymbol{A}_{14}\boldsymbol{A}_{24}]^{O} \times [\boldsymbol{A}_{24}\boldsymbol{A}_{34}]^{O} \\ 0 \end{bmatrix}, \quad (i = 1, 2, 3), \tag{4.38}$$

Combining equations (4.37) and (4.38), the end-effector pose can be written by

$$\begin{aligned} T_{OO'} = & \begin{bmatrix} [\boldsymbol{OA}_{14}]^{O} & [\boldsymbol{OA}_{24}]^{O} & [\boldsymbol{OA}_{34}]^{O} & [\boldsymbol{A}_{14}\boldsymbol{A}_{24}]^{O} \times [\boldsymbol{A}_{24}\boldsymbol{A}_{34}]^{O} \\ 1 & 1 & 1 & 0 \end{bmatrix} \\ & \cdot \begin{bmatrix} [\boldsymbol{OA}_{14}]^{O'} & [\boldsymbol{OA}_{24}]^{O'} & [\boldsymbol{OA}_{34}]^{O'} & [\boldsymbol{A}_{14}\boldsymbol{A}_{24}]^{O'} \times [\boldsymbol{A}_{24}\boldsymbol{A}_{34}]^{O'} \\ 1 & 1 & 1 & 0 \end{bmatrix}^{-1}, \end{aligned} \tag{4.39}$$

Note that the inverse matrix occurs in eqn. (4.39) is a constant matrix for a certain manipulator, and it always exists if points A_{14}, A_{24} and A_{34} are neither collinear nor coincident. Equation (4.39) shows that the pose of the end-effector can be determined once the coordinates of the three points A_{14}, A_{24} and A_{34} with respect to the base frame are obtained. Based on the structure geometry (Fig. 4.6(a)), the z-coordinate of point A_{i4} can be directly calculated by

$$z_{i4} = \theta_{i2} + h. \tag{4.40}$$

As the links $\boldsymbol{A}_{i2}\boldsymbol{A}_{i3}$ and $\boldsymbol{A}_{i3}\boldsymbol{A}_{i4}$ move only in the horizontal plane, the 3-RPPS PM can be projected onto the base plane, i.e., the $\{O\text{-}xy\}$ plane, as shown in Fig. 4.7 or Fig. 4.8. As the moving platform may not be parallel to the base plane, the end-distance of the three limbs, $\|\boldsymbol{A}_{14}\boldsymbol{A}_{24}\|$, $\|\boldsymbol{A}_{24}\boldsymbol{A}_{34}\|$ and $\|\boldsymbol{A}_{34}\boldsymbol{A}_{14}\|$ become the projected distance $\|\boldsymbol{A}'_{14}\boldsymbol{A}'_{24}\|$, $\|\boldsymbol{A}'_{24}\boldsymbol{A}'_{34}\|$ and $\|\boldsymbol{A}'_{34}\boldsymbol{A}'_{14}\|$, that

$$l_1 = \|\boldsymbol{A}'_{14}\boldsymbol{A}'_{24}\| = \sqrt{\|\boldsymbol{A}_{14}\boldsymbol{A}_{24}\|^2 - \|z_{24} - z_{14}\|^2} \tag{4.41}$$

$$l_2 = \|\boldsymbol{A}'_{24}\boldsymbol{A}'_{34}\| = \sqrt{\|\boldsymbol{A}_{24}\boldsymbol{A}_{34}\|^2 - \|z_{24} - z_{34}\|^2} \tag{4.42}$$

$$l_3 = \|\boldsymbol{A}'_{34}\boldsymbol{A}'_{14}\| = \sqrt{\|\boldsymbol{A}_{34}\boldsymbol{A}_{14}\|^2 - \|z_{34} - z_{14}\|^2}. \tag{4.43}$$

To simplify the calculation, a new frame $\{A_{11}\text{-}xy\}$ is taken as the reference frame as shown in Fig. 4.7. Let λ represent the displacement of the passive prismatic joint of limb 1, and β denote the relative angle between $\boldsymbol{A}'_{14}\boldsymbol{A}'_{24}$ and $\boldsymbol{A}'_{14}\boldsymbol{A}'_{34}$. Point A'_{24} slides along a line with unit vector $\boldsymbol{u}_2(u_{2x}, u_{2y})$, and point A'_{34} slides along a line with unit vector $\boldsymbol{u}_3(u_{3x}, u_{3y})$. The posture of the 3-RPR PM will be determined by the value of λ and the orientation angle α. For the structure shown in Fig. 4.7, two equations can describe points A'_{24} and A'_{34} sliding along the given lines:

$$(l_1 \cdot \sin\alpha - y_{21}) \cdot u_{2x} - (\lambda + l_1 \cdot \cos\alpha - x_{21}) \cdot u_{2y} = 0 \tag{4.44}$$

$$(l_1 \cdot \sin(\alpha+\beta) - y_{31}) \cdot u_{3x} - (\lambda + l_1 \cdot \cos(\alpha+\beta) - x_{31}) \cdot u_{3y} = 0 \tag{4.45}$$

The value of α can be obtained by eqn. (4.44) as

$$\lambda = u_{2x} \cdot (l_1 \cdot \sin\alpha - y_{21})/u_{2y} - l_1 \cdot \cos\alpha + x_{21}, \tag{4.46}$$

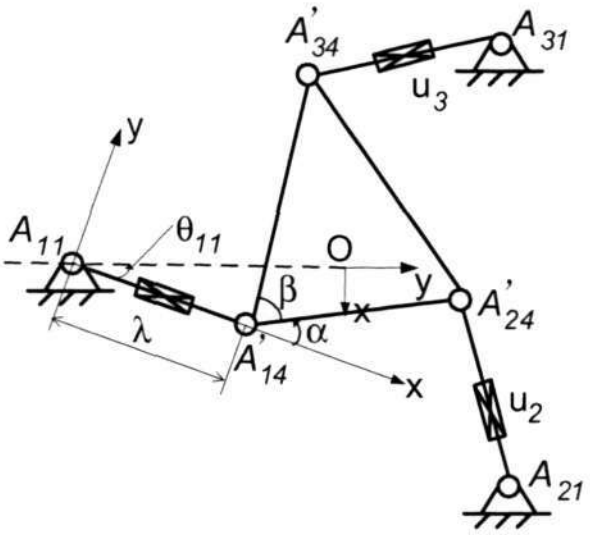

Figure 4.7: Projected planar 3-RPR PM

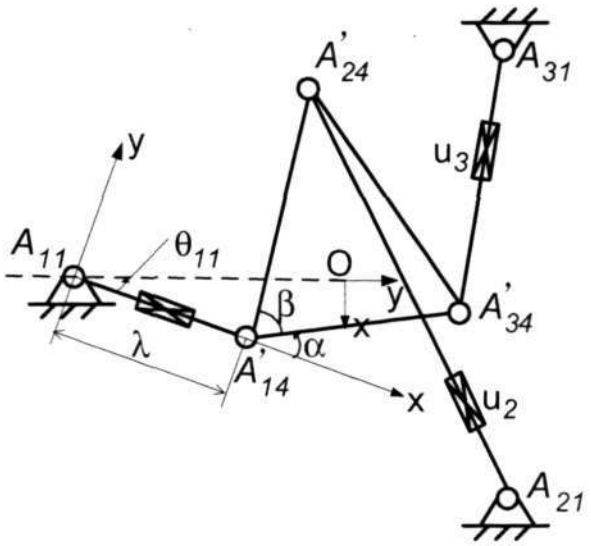

Figure 4.8: Projected planar 3-RPR PM

Substituting λ into eqn. (4.45), we have

$$A \cdot \sin\alpha + B \cdot \cos\alpha + C = 0, \tag{4.47}$$

where

$A = u_{3x} \cdot l_1 \cdot \cos\beta + u_{3y} \cdot l_1 \cdot \sin\beta - u_{3y} \cdot u_{2y} \cdot l_1/u_{2x}$,

$B = u_{3x} \cdot l_1 \cdot \sin\beta - u_{3y} \cdot l_1 \cdot \cos\beta - u_{3y} \cdot \cdot l_1$,

$C = u_{3y} \cdot u_{2y} \cdot y_{21}/u_{2x} - u_{3y} \cdot x_{21} - u_{3x} \cdot y_{31} + u_{3y} \cdot x_{31}$.

For the structure shown in Fig. 4.8, the coefficients of eqn. (4.47) are

$A = u_{2x} \cdot l_2 \cdot \cos\beta + u_{2y} \cdot l_3 \cdot \sin\beta - u_{2y} \cdot u_{3y} \cdot l_3/u_{3x}$,

$B = u_{2x} \cdot l_3 \cdot \sin\beta - u_{2y} \cdot l_3 \cdot \cos\beta - u_{2y} \cdot \cdot l_3$,

$C = u_{2y} \cdot u_{3y} \cdot y_{31}/u_{3x} - u_{2y} \cdot x_{31} - u_{2x} \cdot y_{21} + u_{2y} \cdot x_{21}$.

Assume that $\Omega = \tan(\alpha/2)$, eqn. (4.47) can be written as:

$$(C - B)\Omega^2 + 2A \cdot \Omega + B + C = 0. \tag{4.48}$$

The symbolic solutions of Ω, can be directly obtained by

$$\Omega = (A_{i1} \pm \sqrt{A^2 + B^2 - C^2})/(B - C). \tag{4.49}$$

Therefore,

$$\alpha = 2 \cdot \arctan(\Omega). \tag{4.50}$$

Once the angle α is obtained, λ can be obtained by using eqn. (4.46). After α and λ are solved, the coordinates of A'_{i4} with respect to frame $\{A_{11}\text{-}xy\}$ can be solved as:

$$[\boldsymbol{A}_{11}\boldsymbol{A}'_{14}]^{A_{11}} = \begin{bmatrix} \lambda \\ 0 \end{bmatrix}, \tag{4.51}$$

$$[\boldsymbol{A}_{11}\boldsymbol{A}'_{24}]^{A_{11}} = \begin{bmatrix} \lambda + l_1 \cdot \cos\alpha \\ l_1 \cdot \sin\alpha \end{bmatrix}, \tag{4.52}$$

$$[\boldsymbol{A}_{11}\boldsymbol{A}'_{34}]^{A_{11}} = \begin{bmatrix} \lambda + l_1 \cdot \cos(\alpha + \beta) \\ l_1 \cdot \sin(\alpha + \beta) \end{bmatrix}. \tag{4.53}$$

Let $R^O_{A_{11}}$ represent the transformation from frame $\{A_{11}\text{-}xy\}$ to frame $\{O\text{-}xy\}$, we have

$$R^O_{A_{11}} = \begin{bmatrix} \cos(\pi/2 - \theta_{i1}) & -\sin(\pi/2 - \theta_{i1}) \\ \sin(\pi/2 - \theta_{i1}) & \cos(\pi/2 - \theta_{i1}) \end{bmatrix} = \begin{bmatrix} \sin(\theta_{i1}) & -\cos(\theta_{i1}) \\ \cos(\theta_{i1}) & \sin(\theta_{i1}) \end{bmatrix} \tag{4.54}$$

The coordinates of A'_{i4} with respect frame $\{O\text{-}xy\}$ can be obtained as:

$$[\boldsymbol{OA}'_{i4}]^O = [\boldsymbol{OA}'_{11}]^O + R^O_{A_{11}} \cdot [\boldsymbol{A}_{11}\boldsymbol{A}'_{i4}]^{A_{11}} . \tag{4.55}$$

As A'_{i4} is the projection of A_{i4} along z-axis, the first two coordinates of point of A'_{i4} and A_{i4} are identical. The coordinates of points A_{14}, A_{24} and A_{34} are thus determined. In other words, the position of the moving platform can be directly determined by eqn. (4.39). Hence, there are at most four solutions for the forward kinematics of the 3-RPPS PM.

4.4 Summary

Displacement analysis is the basis for workspace analysis, dimension optimization, motion planing and control. Due to motion decoupling, a decomposition method and a projective method are applied to compute the displacements for the SA-PM and the 3RPPS PM respectively. As a result, closed-form solutions for both inverse and forward kinematics are obtained. There are at most eight solutions for both inverse and forward kinematics of the SA-PM. For the 3RPPS-PM, there are at most eight solutions for the inverse kinematics and four solutions for the forward kinematics.

Chapter 5

Workspace Evaluation through Finite-Partition of $SE(3)$

Workspace analysis is a challenging problem for PMs. The solution of this problem is critical in the design and motion planing of the manipulator. As the complete workspace of a 6-DOF manipulator is embedded in a 6-dimensional space, there is no simple way to visualize it in a human-readable way. Therefore, the workspace of parallel manipulators is usually visualized in various 3-D subspaces [81], such as the constant-orientation workspace, the reachable orientation workspace and the reachable positional workspace.

Due to the complexity of forward kinematic problem which involves solving highly nonlinear equations, there is no suitable way to compute the workspace volume by integrating along its boundary. Hence, very few global performance criteria of PMs can be evaluated. Most of the literatures for optimal design of PM focused on the optimization of the reachable positional workspace which is a 3-D subspace of the complete 6-D manipulator workspace. Based on the topology of the rigid motion group $SE(3)$, a numerical approach to parametrically partition the 6-D workspace into finite elements, is introduced in Section 5.3. Two global performance indices and three optimal points (position or orientation or pose) are introduced in Section 5.4. In Section 5.5, dimension optimization and performance specification of the SA-PM and the 3-RPPS PM are used as case studies to demonstrate the effectiveness of the partition method.

5.1 Introduction

As the major drawback of PMs is their limited workspace, workspace volume becomes an important performance index of PMs [9, 12, 25, 59, 65, 75, 83, 85, 113]. Some researchers made use of geometrical methods to calculate the workspace of PMs [25, 59, 83]. Other researchers studied the design for the desired workspace by optimization [9, 56, 75, 85].

Gosselin [25] proposed a geometrical method to compute the reachable positional workspace of Stewart-type of PMs. The inverse kinematic solution of the PM is used. The workspace boundaries are obtained by the intersection of the reachable workspace generated by each limb. Then the reachable positional workspace is sliced vertically so that the workspace volume of each workspace slice can be integrated along the boundary. The volume of the complete reachable positional workspace is subsequently obtained by the summation of the volume of all workspace slices.

Merlet et al. [83] proposed geometrical algorithms in calculating various types of workspaces for planar PMs. Types of the workspace include constant orientation workspace, the maximal workspace, the inclusive workspace, the total orientational workspace and the dextrous workspace.

Kumar [65] made use of the properties of screw system to calculate the reachable workspace, the dextrous workspace, and the controllable dextrous workspace (a subset of dextrous workspace, in which, with the reference point fixed at any point, the end-effector can rotate completely about any arbitrary line through that point in a controllable, continuous, and smooth motion.) for PMs. According to the screw theory, the singularity conditions, i.e., the workspace boundaries, are transformed into the reciprocal screw conditions for different types of workspaces. By using inverse kinematics, the reciprocal screw condition can be readily obtained, and hence the workspace boundaries.

Masory and Wang [77] introduced a numerical method to compute the reachable workspace

volume with respect to manipulator geometry parameters and joint constraints of a Stewart-type parallel manipulator. The reachable workspace is sliced into laminates so that the workspace boundary of each slice is obtained by a fast search method. The reachable workspace is then quantified by the integration of all slices of the reachable workspace.

Wang and Hsieh [109] proposed a numerical approach for systematically calculating the reachable workspace of general PMs. In this method, finding the extreme reach is formulated as an optimization problem, which can be solved by a combined optimization strategy with the cyclic coordinate descent method and the quasi-Newtonian method. Because it is a numerical optimization method, the global optimal solution cannot be guaranteed.

Badescu and Mavroidis [8] proposed several performance indices for workspace analysis based on the concept of dexterous solid angle [3], including the workspace volume, the dexterous workspace volume, the dexterity index and the workspace volume with a certain dexterity. The concept of dexterous solid angle is used to represent the orientation ability of manipulators, and it refers to the ratio of the service sphere surface area that the end-effector z-axis can intersect to the area of the complete service sphere (a 2-D sphere surface). However, the dexterous solid angle cannot completely represent the dexterity of orientation which should be a 3-D manifold (SO(3)), because it only uses the z-axis of the end-effector to represent the end-effector orientation. Therefore, these performance indices cannot characterize the complete 6-D workspace, including both 3-D translational workspace and 3-D orientational workspace.

The representation of orientational workspace is a challenging problem because it cannot be easily described and visualized as its physical meaning in Cartesian space. Bulca et al. [12] proposed a method to describe the orientational workspace of PMs by using the four Euler-Rodrigues parameters. In order to graphically describe the orientational workspace, one parameter will be eliminated based on the normality condition.

Yang et al. [113] presented a differential geometry approach for numerically analyzing the orientational workspace of parallel manipulators which can be represented by the Special Orthogonal group $SO(3)$ and geometrically visualized as a solid sphere of radius π. A 3D division scheme is proposed to parametrically and proportionally divide the solid sphere into a number of finite elements of the same volume. When the number of the finite elements is sufficiently large, each element can be kinematically represented by a point located inside the element. Hence, the workspace volume is converted into a simple summation of all volume elements in the workspace.

5.2 Geometric Background

A general rigid body spatial motion consisting of both translation and rotation can be mathematically represented by an element of the Special Euclidean group $SE(3)$, which has the following form:

$$SE(3) = \{(\boldsymbol{p}, R) \mid \boldsymbol{p} \in \mathbb{R}^3, R \in SO(3)\} \equiv \mathbb{R}^3 \times SO(3), \tag{5.1}$$

where $SO(3)$ is the Special Orthogonal group representing the spatial rigid body rotation, $R \in SO(3)$ represents a rigid body rotation and $\boldsymbol{p} \in \mathbb{R}^3$ represents a rigid body translation. For the purpose of homogeneous transformation, it can also be denoted by a 4×4 matrix in the form of

$$\begin{bmatrix} R & \boldsymbol{p} \\ \mathbf{0} & 1 \end{bmatrix}. \tag{5.2}$$

$SE(3)$ is a Lie group of dimension six. The *Lie algebra* of $SE(3)$, denoted as $se(3)$, has the form of

$$\begin{bmatrix} \hat{w} & \boldsymbol{v} \\ \mathbf{0} & 0 \end{bmatrix}, \tag{5.3}$$

where

$$\hat{w} = \begin{bmatrix} 0 & -w_z & w_y \\ w_z & 0 & -w_x \\ -w_y & w_x & 0 \end{bmatrix}. \tag{5.4}$$

The set of 3×3 real skew-symmetric matrices, $\hat{w}$, forms the Lie algebra of $SO(3)$, denoted by $so(3)$. Note that a skew-symmetric matrix can be equivalently represented as a vector

$\boldsymbol{w} = [w_x, w_y, w_z]^T \in \mathbb{R}^3$ for assigning the orientation of the end-effector. An element of $se(3)$ thus admits a 6×1 vector form: $\begin{bmatrix} \boldsymbol{w} \\ \boldsymbol{v} \end{bmatrix} \in \mathbb{R}^6$, termed a twist.

Based on the topology of $\mathbb{R}^3$, the geometry of $\mathbb{R}^3$ can be regarded as a cube as shown in Fig. 5.1. Hence the volume element for integration can be defined with Cartesian coordinates as

$$d\boldsymbol{p} = dx \cdot dy \cdot dz. \tag{5.5}$$

Obviously, the rigid body translation $\mathbb{R}^3$ can be conveniently described by using the 3D Cartesian coordinates system. However, this is not the case for rigid body rotation because $SO(3)$ is only topologically homeomorphic to $\mathbb{R}^3$ and it does not bear the simple geometrical features of [68]. Usually, a relatively intuitive way to represent orientations makes use of three Euler angle parameters. But such a representation approach has its inherent disadvantages, i.e. the three parameters are not independent to each other and need to follow certain sequence, and singularities exist (e.g. when $\beta = 0$ and $\beta = \pi$ for $\alpha - \beta - \gamma$ parameters in the Z-Y-Z Euler angle representation).

Park and Ravani [68, 92] verified that the Special Orthogonal group $SO(3)$ can be visualized as a solid sphere of radius π centered at the origin in $\mathbb{R}^3$ as shown in Fig. 5.2. Note that the solid sphere is viewed in the coordinate frame of exponential coordinates of $SO(3)$. Each point in the solid sphere maps one element of $SO(3)$ which have the form as

$$R = e^{\hat{\boldsymbol{w}}}. \tag{5.6}$$

In this way, $SO(3)$ can be parameterized with exponential coordinates $\{w_x, w_y, w_z\}$, which can be viewed as Cartesian coordinates over the interior space of the solid sphere.

It is shown in [15] that the volume element (i.e., differentiation of eqn. (5.6)) can be written as

$$dR = |det(J(R(\boldsymbol{w})))| d\boldsymbol{w}, \tag{5.7}$$

where dR denotes the volume element of $SO(3)$, $d\boldsymbol{w} = dw_x dw_y dw_z$ denotes the volume

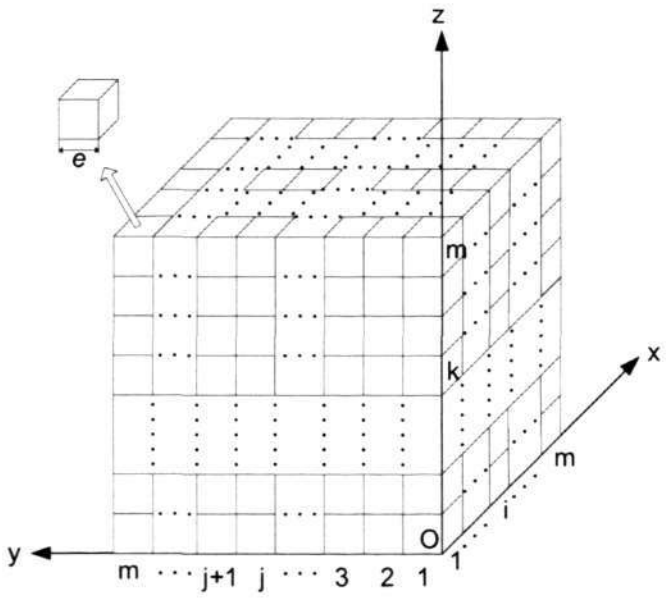

Figure 5.1: Partition of $\mathbb{R}^3$

element of the solid sphere of radius π in $\mathbb{R}^3$, and $|det(J(R(\boldsymbol{w})))| = \frac{2(1-\cos(\|\boldsymbol{w}\|))}{\|\boldsymbol{w}\|^2}$, $(\|\boldsymbol{w}\| = \sqrt{w_x^2 + w_y^2 + w_z^2})$, is the integration measure. Therefore, the entire $SO(3)$ workspace volume is given by

$$\int_{R\in SO(3)} dR = \int_{\boldsymbol{w}\in D^3} f(R(\boldsymbol{w}))\frac{2(1-\cos(\|\boldsymbol{w}\|))}{\|\boldsymbol{w}\|^2}d\boldsymbol{w} = 8\pi^2, \tag{5.8}$$

The integration of a rotation-dependant function $f(R)$ over a set of rotations $S \in SO(3)$ is given by

$$\int_{R\in S} f(R)dR = \int_{\boldsymbol{w}\in Q} f(R(\boldsymbol{w}))\frac{2(1-\cos(\|\boldsymbol{w}\|))}{\|\boldsymbol{w}\|^2}d\boldsymbol{w}, \tag{5.9}$$

where Q denotes the parameter space, i.e., a subset of D^3 (the solid ball).

As each element of $SE(3)$ is the product of two related elements of $\mathbb{R}^3$ and $SO(3)$ respectively, the product of two volume elements of $\mathbb{R}^3$ and $SO(3)$ respectively leads to the corresponding volume element of $SE(3)$. Based on eqn. (5.5) and eqn. (5.7), the volume element of $SE(3)$, dW, can be written as

$$dW = d(\boldsymbol{p}, R) = d\boldsymbol{p} \cdot dR = d\boldsymbol{p} \cdot \frac{2(1-\cos(\|\boldsymbol{w}\|))}{\|\boldsymbol{w}\|^2}d\boldsymbol{w}. \tag{5.10}$$

To make ease of workspace evaluation of a manipulator, following terms are defined:

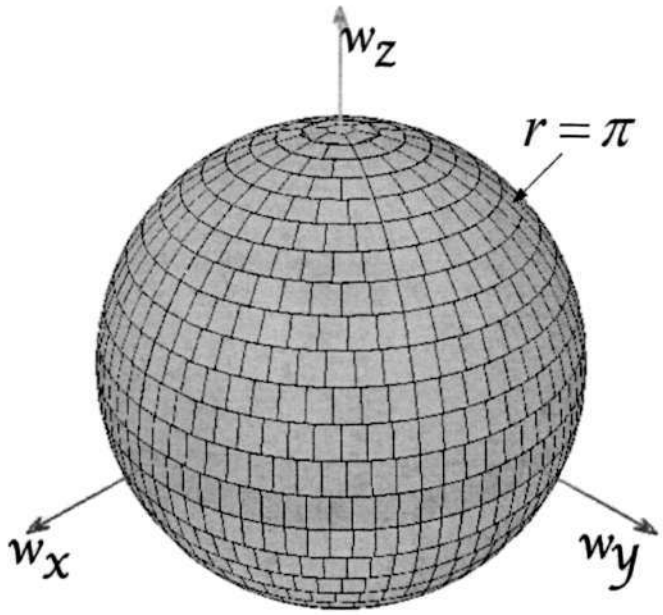

Figure 5.2: Visualization of $SO(3)$

- W: the complete 6-D workspace, $W \in SE(3)$;
- W_p: the reachable positional workspace, $W_p \subset \mathbb{R}^3$;
- W_R: the reachable orientational workspace, $W_R \subseteq SO(3)$;
- $W_R(\boldsymbol{p})$: the orientational workspace at a constant position $\boldsymbol{p}$, $W_R(\boldsymbol{p}) \subseteq W_R$;
- $W_p(R)$: the positional workspace under a constant orientation R, $W_p(R) \subseteq W_p$;
- W_C: the positional workspace envelope containing the reachable positional workspace of a manipulator, $W_C \subset \mathbb{R}^3$ and $W_C \supseteq W_p$.

The manipulator workspace $W \in SE(3)$ can be represented by

$$W = \{(\boldsymbol{p}, R) \mid \boldsymbol{p} \in W_p \subseteq \mathbb{R}^3, R \in W_R(\boldsymbol{p}) \subseteq SO(3)\}, \tag{5.11}$$

or

$$W = \{(\boldsymbol{p}, R) \mid \boldsymbol{p} \in W_p(R) \subseteq \mathbb{R}^3, R \in W_R \subseteq SO(3)\}. \tag{5.12}$$

In most cases, the position and orientation are dependent on each other. Based on eqn. (5.10), the workspace volume of a manipulator (eqn. (5.11) or eqn. (5.12)) can be written as

$$\int_W dW = \int_{\boldsymbol{p}\in W_p} \int_{R\in W_R(\boldsymbol{p})} \frac{2(1-\cos(\|\boldsymbol{w}\|))}{\|\boldsymbol{w}\|^2} d\boldsymbol{w}d\boldsymbol{p}, \tag{5.13}$$

or

$$\int_W dW = \int_{R\in W_R} \int_{\boldsymbol{p}\in W_p(R)} \frac{2(1-\cos(\|\boldsymbol{w}\|))}{\|\boldsymbol{w}\|^2} d\boldsymbol{p}d\boldsymbol{w}. \tag{5.14}$$

As the reachable position workspace W_p is usually easy to obtain, eqn. (5.13) is preferred for workspace determination.

5.3 Finite-partition of $SE(3)$

As each element of $SE(3)$ is the product of two related elements of $\mathbb{R}^3$ and $SO(3)$ respectively, the finite-partition of $SE(3)$ can be transformed into partitions of the cube and the solid sphere respectively. To isotropically partition the cube and the solid sphere into finite elements, following properties are required to be fulfilled:

- **Geometric identity:** All elements are geometrically identical to each other.
- **Parametrization:** The number of elements is determined based on the division m along each dimension, which is parametrically alterable. In other words, the total number of elements is in the order of $O(m^3)$ for a three dimensional manifold.
- **Uniform convergence:** All three dimensions of each element are inverse-proportional to the division m, so the dimensions are uniformly convergent when m is large.

5.3.1 Isotropic Partition of $\mathbb{R}^3$

Partition method

Based on the topology of $\mathbb{R}^3$, the geometry of $\mathbb{R}^3$ can be regarded as a cube. A natural isotropic partition of the cube is to take a cubic element as the basis element which is homomorphic to $\mathbb{R}^3$, as shown in Fig. 5.1. Let m be the number of division along each dimension, which determines the numerical resolution of each element in the cube. Therefore, there are totally m^3 basis elements in the cube. Each basis element will have the same convergence rate with m increasing. When m is sufficiently large, each element can be regarded as a point. When the manipulator workspace is to be evaluated, the reachable position workspace can always be bounded by a cube although it may be of a complex shape. To reduce the computation effort, one can also choose a cuboid to bound the reachable position workspace. In this case, the scaling factors along each dimension are required to normalizing the cuboid to a cube.

Mathematical representation of elements

To facilitate the numerical computation, a feature point within each element, will be defined to represent the local property of the element when m is sufficiently large. The centroid of the basis cube element will be a suitable choice as the feature point of the element. Assume that the reachable position workspace W_p is embedded in a cube with edge of length a. As shown in Fig. 5.1, the edge length e of the basis element is defined as:

$$e = \frac{a}{m}. \tag{5.15}$$

Let i, j and k represent the ordinal number along the x, y and z axes respectively, we have the coordinates of the (i, j, k) element as follows.

$$\begin{cases} x = (i-1) * e + \frac{e}{2} \\ y = (j-1) * e + \frac{e}{2} \\ z = (k-1) * e + \frac{e}{2} \end{cases}. \tag{5.16}$$

5.3.2 Equi-volumetric Partition of Solid Sphere [113]

The solid sphere does not possess such an isotropic partition scheme as $\mathbb{R}^3$ so that the above three properties could not be simultaneously satisfied. By relaxing the first property of geometric identity to equi-volumetric elements, it is possible to obtain an equi-volumetric partition of the solid sphere that satisfies Properties 2 and 3 as well. Yang et al. [113] presented a differential geometry approach for parametrically and proportionally dividing the solid sphere of radius π into $2n^3$ elements with the same unit volume $d\boldsymbol{w}$ in $\mathbb{R}^3$. With every element of the same volume, numerical integration in $SO(3)$ becomes algebraical addition of valid volume elements in $SO(3)$ based on eqn. (5.9).

Partition method

The equi-volumetric partition scheme of $SO(3)$ is achieved based on the equi-volumetric partition on the solid sphere of radius π in a number of steps shown below.

STEP 1: *Solid ball to solid hemispheres*

Divide the solid sphere into two solid hemispheres along w_x-O-w_y plane, as shown in Fig. 5.3. Because $SO(3)$ is equivalent to a solid sphere of radius π with antipodal points identified, attention will be focused on one solid hemisphere in the following context as the other one will be partitioned in a similar manner.

STEP 2: *Solid hemisphere to hemispherical shells*

Divide the solid hemisphere into n hemispherical shells (like onion shells) with the same thickness δr $(= \pi/n)$ as shown in Fig. 5.4. Note that the first shell, the core, is a small solid hemisphere with a radius of $r_1 = \delta r = \frac{\pi}{n}$ and a volume of $\mathrm{v}_u = \frac{2\pi\delta r^3}{3} = \frac{2\pi^4}{3n^3}$. This core element is a basic element of the partition scheme and its volume is defined as the unit volume of all the partition elements though they may be topologically different. Label the shells from 1 to n starting from the core. The i^{th} hemispherical shell $(i = 1, 2, \ldots, n)$ possesses m_i $(= i^3 - (i-1)^3)$ elements of identical volume of v_u. Altogether the entire

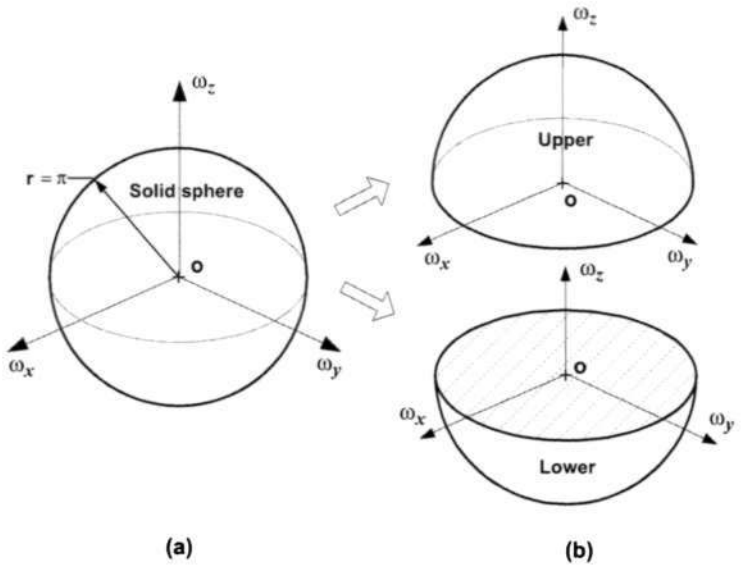

Figure 5.3: Partition of the solid sphere into two solid hemispheres

solid hemisphere contains m $(= \sum_{i=1}^{n} m_i = n^3)$ such elements.

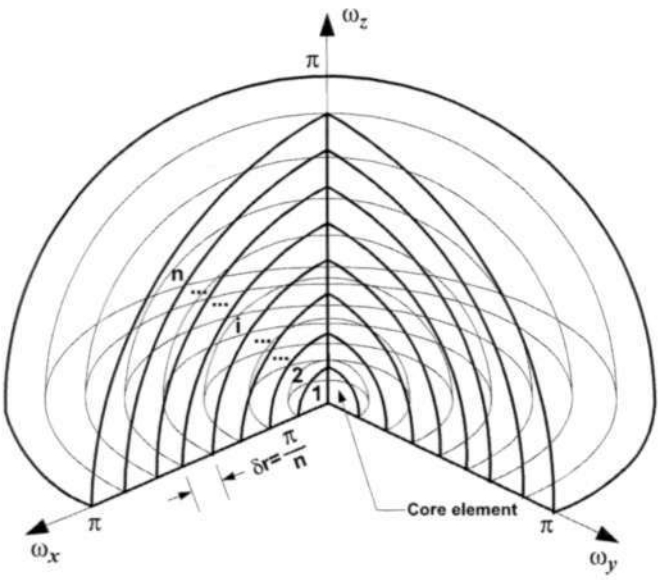

Figure 5.4: Shells of a solid hemisphere

STEP 3: *Hemispherical shells to basic elements*

Divide the i^{th} hemispherical shell $(i = 2, 3, \ldots, n)$ into m_i elements of the same volume, i.e., the unit volume. Now consider the integer $m_i = i^3 - (i-1)^3 = 1 + 3i(i-1)$ which is the number of elements in the i^{th} shell. It is realized that m_i is equal to the summation

of the integer series $1, 6, 12, \ldots, 6(i-1)$, i.e., $m_i = 1 + \sum_{p=1}^{i} 6(p-1)$. For example, the second shell has $m_2 = 7 = 1 + 6$ elements and the third shell has $m_3 = 19 = 1 + 6 + 12$ elements. Based on this integer series expression of m_i, an equi-volumetric partition of the i^{th} hemispherical shell into m_i elements ($i = 2, 3, \ldots, n$) can be achieved in the following manner.

Step 3-1 Divide the i^{th} hemispherical shell into one circular cap and $i-1$ circular bands around the pole as shown in Fig. 5.5a. The cap element is a spherical disk shell homeomorphic to $D^2 \times \Re$ and has a unit volume of v_u. Label the cap and the bands from 1 to i.

Step 3-2 Based on the integer series $1, 6, \ldots 6(j-1)$, divide the j^{th} ($j = 2, 3, \ldots, i$) band into $6(j-1)$ equi-volumetric elements of v_u. These elements, called common elements, are spherical rectangular shells homeomorphic to $\mathbb{R}^3$. To ensure that the volume of every element is identical to the unit volume, the angular division of the spherical rectangular shell needs to obey two rules:

- As shown in Fig. 5.5b, The latitudinal division angle of the j^{th} band ($j = 1$ for the cap) in the i^{th} shell, β_{ij}, can be computed as:

$$\begin{aligned} \beta_{ij} &= \cos^{-1}\left(1 - \frac{j^3 - (j-1)^3}{i^3 - (i-1)^3}\right) \\ &= \cos^{-1}\left(\frac{3(i-j)(i+j-1)}{1 + 3i(i-1)}\right) \end{aligned} \tag{5.17}$$

  where $i = 2, 3, \ldots, n$ and $j = 1, 2, \ldots, i$.

- The longitudinal span of the common element in the j^{th} band of the i^{th} shell is $\gamma_{ij} = \frac{2\pi}{6(j-1)}$ as shown in Fig. 5.5c. Therefore, the longitudinal orientation (starting from w_x-axis) of the k^{th} element in the j^{th} band can be given by:

$$\alpha_{ijk} = \frac{2k\pi}{6(j-1)}, \tag{5.18}$$

  where $i = 2, 3, \ldots, n$, $j = 2, \ldots, i$, and $k = 1, 2, \ldots, 6(j-1)$. Note that there is no division in the cap element ($j = 1$) and thus $\alpha_{i11} = 2\pi$.

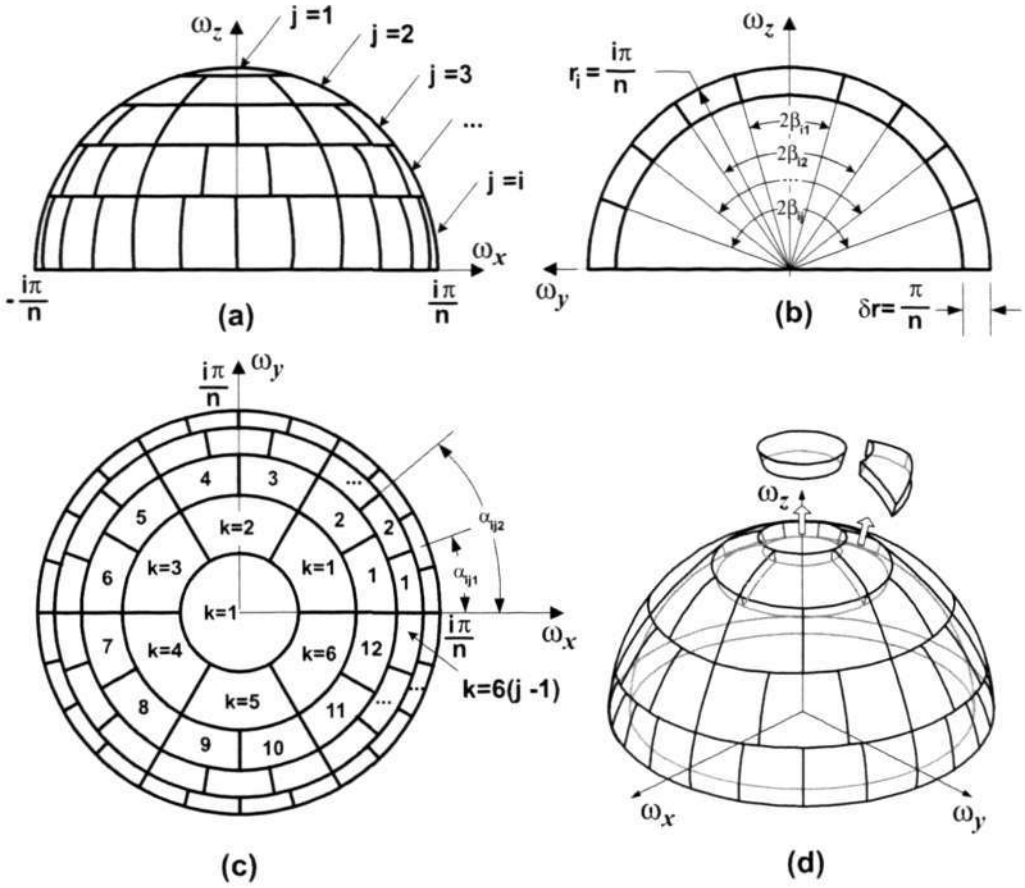

Figure 5.5: Equi-volumetric partition of a hemispherical shell

Using this finite partition scheme, the solid hemisphere of radius π can be divided into n^3 elements of equal volume. There is one core element of a solid hemisphere of radius $\frac{\pi}{n}$, n cap elements of spherical disk shells, and the rest are all common elements of spherical rectangular shells. With the other hemisphere partitioned in the same manner, the complete solid sphere $SO(3)$ will have $2n^3$ elements in total. It was verified in [113] that when the number of elements increases, the dimensions of every element have the same convergence rates according to n.

Mathematical representation of elements

To simplify computational effort, the feature point of a common element is selected as the intersecting point of its three neutral planes. Hence, the feature point coordinates, $w_{ijk} =$

$(w^x_{ijk}, w^y_{ijk}, w^z_{ijk})$ $(i = 2,3,\ldots,n; j = 2,3,\ldots,i, k = 1,2,\ldots,6(j-1))$ can determined through its spherical coordinates r^w_i, β^w_{ij}, and α^w_{ijk} given by:

$$\begin{aligned} r^w_i &= \frac{r_i + r_{i-1}}{2} = \frac{(2i-1)\pi}{2n}, \\ \beta^w_{ij} &= \frac{\beta_{ij} + \beta_{i(j-1)}}{2}, \\ \alpha^w_{ijk} &= \frac{\alpha_{ijk} + \alpha_{ij(k-1)}}{2}. \end{aligned} \tag{5.19}$$

The Cartesian coordinates of the feature point, w_{ijk}, can be determined by:

$$\begin{aligned} w^x_{ijk} &= r^w_i \sin\beta^w_{ij} \cos\alpha^w_{ijk}, \\ w^y_{ijk} &= r^w_i \sin\beta^w_{ij} \sin\alpha^w_{ijk}, \\ w^z_{ijk} &= r^w_i \cos\beta^w_{ij}. \end{aligned} \tag{5.20}$$

As the core and cap elements $(i = 1,2,\ldots,n; j = k = 1)$ are along the pole axis of the solid sphere, their feature point coordinates can be written as:

$$\begin{aligned} w^x_{ijk} &= 0 \\ w^y_{ijk} &= 0, \\ w^z_{ijk} &= \frac{(2i-1)\pi}{2n}. \end{aligned} \tag{5.21}$$

For the lower half solid hemisphere, the Cartesian coordinates of all n^3 feature points $\bar{w}_{ijk} = (\bar{w}^x_{ijk}, \bar{w}^y_{ijk}, \bar{w}^z_{ijk})$, have the following form due to symmetry about the $x-y$ plane:

$$\begin{aligned} \bar{w}^x_{ijk} &= w^x_{ijk}, \\ \bar{w}^y_{ijk} &= w^y_{ijk}, \\ \bar{w}^z_{ijk} &= -w^z_{ijk}, \end{aligned} \tag{5.22}$$

where $i = 1,2,\ldots,n; j = 1,2,\ldots,i; k = 1,2,\ldots,6(j-1)$. Therefore, the solid sphere can be characterized by all feature points of $2n^3$ equi-volumetric elements. Using eqn. (5.6), the rotation matrices associate with feature points w_{ijk} and $\bar{w}_{ijk}$ can be written as

$$\begin{aligned} R_{ijk} &= e^{\hat{w}_{ijk}}, \\ \bar{R}_{ijk} &= e^{\hat{\bar{w}}_{ijk}}. \end{aligned} \tag{5.23}$$

An algorithm to calculate the coordinates of each element and its corresponding rotation matrices of $SO(3)$ has been introduced in [113].

5.4 Global Performance Indices

For optimal design of parallel manipulators, the workspace quality and quantity measures appear to be the most suitable indices. The isotropy property is often used for a specific task. Based on the finite-partition of $SE(3)$, two global performance indices and three optimal points will be introduced in this section, which are very helpful for the dimension optimization and task-based applications.

Workspace Volume Ratio (W_r)

As the workspace calculation involves the solutions of highly non-linear equations, it is a challenging problem to compute the workspace volume of the complete 6-D workspace. The 3-D reachable positional workspace is usually used for calculating the workspace volume in literatures [25, 77]. However, the volume of the 3-D reachable workspace cannot represent the complete properties of the entire 6-D workspace. Therefore an effective method for quantity the 6-D workspace is necessary and essential.

As discussed in Section 5.3, one can use the feature points of $\mathbb{R}^3$ or $SO(3)$ to represent the properties of the partitioned elements of $\mathbb{R}^3$ or $SO(3)$ respectively when m and n is sufficiently large. The product of two feature points of $\mathbb{R}^3$ and $SO(3)$ respectively, forms a feature point representing an element of $SE(3)$, which is associated with a spatial transformation. As the parallel manipulators have limited workspace, the dimensions are always optimized for obtaining the maximal workspace. The workspace volume ratio, W_r,

is defined as a workspace volume measure as follows.

$$W_r = \frac{\int_{\boldsymbol{p}\in W_p}\int_{R\in W_R(\boldsymbol{p})}\frac{2(1-\cos(\|w\|))}{\|w\|^2}d\boldsymbol{w}d\boldsymbol{p}}{\int_{\boldsymbol{p}\in W_C}\int_{R\in SO(3)}\frac{2(1-\cos(\|w\|))}{\|w\|^2}d\boldsymbol{w}d\boldsymbol{p}}\times 100\% = \frac{\sum_{R\in W_R(\boldsymbol{p})\ \&\ \boldsymbol{p}\in W_p} dW}{\sum_{R\in SO(3)\ \&\ \boldsymbol{p}\in W_C} dW}\times 100\%. \quad (5.24)$$

The numerator of the right-hand side of eqn. (5.24) is to compute the workspace volume of a manipulator in hand. The denominator represents the volume of the entire sampling workspace, which is determined by the position workspace envelope W_C and the entire orientational workspace $SO(3)$. As the parameter spaces of W_C and $SO(3)$ are always larger than that of W_p and $W_R(\boldsymbol{p})$ respectively, we have $W_r \in [0.0\%\ 100\%]$. The larger the W_r value, the larger the workspace volume.

Global Condition Index

Jacobian matrix is very important in manipulator design because it is used to map both the velocity and the force systems from the actuator input to end-effector output. The relationships are shown by following equations:

$$\Delta\boldsymbol{\theta} = J\Delta\boldsymbol{X}, \quad (5.25)$$

$$\boldsymbol{F} = J^T\boldsymbol{\tau}, \quad (5.26)$$

where $\Delta\boldsymbol{\theta}$ and $\Delta\boldsymbol{X}$ are the infinitesimal actuator input displacements and the end-effector output displacements respectively, $\boldsymbol{F}$ represents the end-effector output forces and moments, and $\boldsymbol{\tau}$ represents the actuator input torques or forces. Equations (5.25) and (5.26) show that the manipulator performance is largely dependent on the property of the Jacobian matrix.

It is often based on the condition number of the manipulator Jacobian matrix ($C(J)$) to evaluate the workspace quality [97]. The condition number of the Jacobian matrix is defined as

$$C(J) = \|J\|\|J^{-1}\|, \quad (5.27)$$

where $\|\cdot\|$ denotes the Euclidean norm of its matrix argument, which is defined as

$$\|J\| = \sqrt{tr(J \cdot \mathrm{W} \cdot J^T)}; \quad \mathrm{W} = \frac{1}{u} I \tag{5.28}$$

where u is the dimension of the square matrix J, and I is the $u \times u$ identity matrix. As $C(J)$ is always positive and $1 \leq C(J) \leq +\infty$, the inverse of condition number, or condition index ($C_I(J)$), is often used, thus

$$C_I(J) = 1/C(J), \quad C_I(J) \in [0, 1]\,. \tag{5.29}$$

The condition number of a matrix measures the sensitivity of the solution of a system of linear equations to errors in the data. It gives an indication of the accuracy of the results from matrix inversion and the linear equation solution. As the Jacobian matrix maps both the velocity and static force between the actuator inputs and the end-effector outputs in robot design, the condition index is used to evaluate the kinetostatic performance of a manipulator. It can represent not only the occurrence of the singular point, but also how far it is away from its nearest singularity. It also represents uniformity of the force distribution with the homogeneous actuator input. The larger the condition index, the velocity and force is more uniformly distributed in the entire workspace. When the condition index approaches zero, the Jacobian matrix is ill-conditioned. The manipulator will be in an isotropic configuration when the condition number is identity.

Note that when the end-effector motion includes both rotation and translation, the elements of Jacobin matrix will have inhomogeneous units, i.e., no physical unit for orientation but physical unit for position, such as the meter. Even though the Jacobian has homogeneous units, the condition index can only evaluate uniformity of the Cartesian velocities and/or end-effector wrenches with identical actuator inputs. In practice, the actuators of a robot may have very different capacity (such as larger actuators at the base and smaller actuators near the end-effector of a fixed stationed robot). To cope with this problem, Tandirci et al. [101] proposed the concept of characteristic length (CL) to minimizing the condition number of the dimensionless Jacobian. This approach later was

generalized by Stocco et al. [100] by using two scaling matrices to normalize the Jacobian matrix and balancing the nonuniform capabilities of actuators for task-based design.

To evaluate the global properties of the workspace, Gosselin [27] proposed the global condition index (GCI) which is the ratio between the integration of condition index and the workspace volume. However, the workspace volume is merely the reachable positional workspace, the 3-D sub-space of the 6-D workspace. The GCI can be extended to the entire 6-D workspace based on the notion of $SE(3)$. Therefore, the following definition of GCI in 6-D workspace is adopted:

$$GCI = \frac{\int_W C_I(J)dW}{\int_W dW} = \frac{\sum_W C_I(J)dW}{\sum_W dW}, \tag{5.30}$$

where W is the 6-D workspace, and J is the manipulator Jacobian matrix which is pose dependent.

Definition: Global Optimal Position

For a specific manipulator design, one may want to find the position with maximal orientational workspace, which is necessary for machining tasks on complex surfaces. The global optimal position $\boldsymbol{p}_G$ can be defined as

$$\boldsymbol{p}_G = \{\boldsymbol{p} \mid max\ W_R(\boldsymbol{p}) \subseteq SO(3)\}. \tag{5.31}$$

Definition: Global Optimal Orientation

Similarly, one may want to find the orientation with maximal positional workspace, which is used for the tasks with translational requirements, such as pick-and-place. Therefore, the global optimal orientation R_G, corresponding to the maximal positional workspace can be defined as

$$R_G = \{R \mid max\ W_p(R) \subset \mathbb{R}^3\}. \tag{5.32}$$

Definition: Global Isotropy Point

Isotropy refers to the condition index of manipulator Jacobian equal to one so that it has uniform velocity and force distribution. Global isotropy point (GIP) here is defined as

the point in $SE(3)$ with the best conditioning. In other words, the point with maximal condition index is the GIP, which is often used as the operational pose of manipulators.

5.5 Applications

In this section, the two global performance indices and the three optimal points are applied to optimize the geometrical dimensions and evaluate the performance of the SA-PM and the 3RPPS PM respectively. For the manipulator workspace optimization through the finite-partition of $SE(3)$, we need to follow the procedure below.

1. Find reachable position workspace W_p, so that the position workspace envelope W_C can be defined;
2. Partition the workspace in $SE(3)$ which is determined by W_C and $SO(3)$ into $m^3 \times 2n^3$ basis elements of $SE(3)$;
3. Compute the feature point of each basis elements of $SE(3)$;
4. Check if each feature point is in the workspace by inverse kinematics;
5. Compute the volume (dW) and condition index C_I of current element of $SE(3)$;
6. Calculate the workspace volume ratio W_r and the global condition index GCI based on equations (5.24) and (5.30).

5.5.1 Dimension optimization of SA-PM

For the SA-PM, the kinematics displacement analysis clearly shows us that the position of the moving platform is directed controlled by three linear actuators, and the orientation is only related with the rotary actuators and passive rotary joints without considering passive joints' limits. Hence, for any end-effector orientation, the translation workspace of the end-effector is always the same without considering the joint limits. At each

point in the positional workspace, the orientational workspace is always identical if the passive P-joints are within their joint limits. Due to the decoupling characteristics, the design parameters related to position and orientation of the SA-PM can be optimized respectively.

Determination of parameters relating to positional workspace

Assume that the moving range of each linear actuator is $[L_1 - \rho_{max}/2, L_1 + \rho_{max}/2]$, the range of $K_i (i = 1, 2, 3)$ of eqn. (4.6) is

$$-\rho_{max}/2 - p_{4y} + L_1 \leq K_i \leq \rho_{max}/2 - p_{4y} + L_1. \tag{5.33}$$

Without loss of generality, assume that $L_1 = p_{4y}$ for simplification of expressions, eqn. (5.33) can be simplified as

$$-\rho_{max}/2 \leq K_i \leq \rho_{max}/2. \tag{5.34}$$

Based on eqn. (4.6), K_1, K_2 and K_3 are constants with given actuator displacements. Combining the two equations, $f_1(\theta_{13}, \theta_{14}) = K_2$ and $f_2(\theta_{13}, \theta_{14}) = K_3$, the passive prismatic joint displacements, θ_{13} and θ_{14} can be computed as follows:

$$\theta_{13} = (-p_{4x} + K_2 \cdot c\alpha \cdot c\theta_{11} + K_3 \cdot c\alpha \cdot s\theta_{11} - K_2 \cdot s\alpha \cdot s\theta_{11} + K_3 \cdot s\alpha \cdot c\theta_{11} - L_2 \cdot s\alpha)/s\alpha \tag{5.35}$$

$$\theta_{14} = (p_{4x} \cdot c\alpha - p_{4z} \cdot s\alpha - L_3 \cdot s\alpha - K_2 \cdot c\theta_{11} - K_3 \cdot s\theta_{11})/s\alpha. \tag{5.36}$$

Let $s\mu = K_2/\sqrt{K_2^2 + K_3^2}, (0 \leq \mu < \pi)$, eqn. (5.35) and eqn. (5.36) can be written as

$$\theta_{13} = (-p_{4x} + \sqrt{K_2^2 + K_3^2} \cdot s(\mu + \alpha + \theta_{11}) - L_2 \cdot s\alpha)/s\alpha, \tag{5.37}$$

$$\theta_{14} = (p_{4x}c\alpha - p_{4z}s\alpha - L_3 s\alpha - \sqrt{K_2^2 + K_3^2} \cdot s(\mu + \theta_{11}))/s\alpha. \tag{5.38}$$

As $|s(\mu + \alpha + \theta_{11})| \leq 1$ and $|s(\mu + \theta_{11})| \leq 1$, the required maximal motion range of passive P-joints of limb 1 can be obtained as follows:

$$(-p_{4x} - L_2 \cdot s\alpha - \sqrt{2}/2\rho_{max})/s\alpha \leq \theta_{13} \leq (-p_{4x} - L_2 \cdot s\alpha + \sqrt{2}/2\rho_{max})/s\alpha, \tag{5.39}$$

$$(p_{4x}c\alpha - p_{4z}s\alpha - L_3s\alpha - \sqrt{2}/2\rho_{max})/s\alpha \leq \theta_{14} \leq (p_{4x}c\alpha - p_{4z}s\alpha - L_3s\alpha + \sqrt{2}/2\rho_{max})/s\alpha. \tag{5.40}$$

Similarly, the optimal dimensions of passive P-joints of limbs 2 and 3 can be obtained:

$$(-p_{4x} - L_2 \cdot s\alpha - \sqrt{2}/2\rho_{max})/s\alpha \leq \theta_{23} \leq (-p_{4x} - L_2 \cdot s\alpha + \sqrt{2}/2\rho_{max})/s\alpha, \tag{5.41}$$

$$(p_{4x}c\alpha - p_{4z}s\alpha - L_3s\alpha - \sqrt{2}/2\rho_{max})/s\alpha \leq \theta_{24} \leq (p_{4x}c\alpha - p_{4z}s\alpha - L_3s\alpha + \sqrt{2}/2\rho_{max})/s\alpha, \tag{5.42}$$

$$(-p_{4x} - L_2 \cdot s\alpha - \sqrt{2}/2\rho_{max})/s\alpha \leq \theta_{33} \leq (-p_{4x} - L_2 \cdot s\alpha + \sqrt{2}/2\rho_{max})/s\alpha, \tag{5.43}$$

$$(p_{4x}c\alpha - p_{4z}s\alpha - L_3s\alpha - \sqrt{2}/2\rho_{max})/s\alpha \leq \theta_{34} \leq (p_{4x}c\alpha - p_{4z}s\alpha - L_3s\alpha + \sqrt{2}/2\rho_{max})/s\alpha. \tag{5.44}$$

Generally speaking, the longer the stroke, the heavier and bulkier the passive prismatic joint will be. It would be better makeing the required motion range of the passive prismatic joints small. Based on eqn. (5.39) to eqn. (5.44), we can easily obtain the optimal value for α:

$$\alpha = \pi/2. \tag{5.45}$$

The required maximal dimensions of passive P-joints are further computed as:

$$-p_{4x} - L_2 - \sqrt{2}/2\rho_{max} \leq \theta_{i3} \leq -p_{4x} - L_2 + \sqrt{2}/2\rho_{max}, \quad (i = 1, 2, 3) \tag{5.46}$$

$$-p_{4z} - L_3 - \sqrt{2}/2\rho_{max} \leq \theta_{i4} \leq -p_{4z} - L_3 + \sqrt{2}/2\rho_{max}, \quad (i = 1, 2, 3) \tag{5.47}$$

Without loss of generality, we can assume that $p_{4z} = -L_3$, so eqn. (5.47) can be rewritten as:

$$-\sqrt{2}/2\rho_{max} \leq \theta_{i4} \leq +\sqrt{2}/2\rho_{max}, \qquad (i = 1, 2, 3). \tag{5.48}$$

As a result, it will not limit the orientational workspace if the motion range of each passive P-joints is in $\left[0, \sqrt{2}\rho_{max}\right]$. In other words, the manipulator will have identical positional or orientational workspace at every orientation or position in the entire workspace. However, in practice, joint limits always exist to reduce the weight of the moving components and to

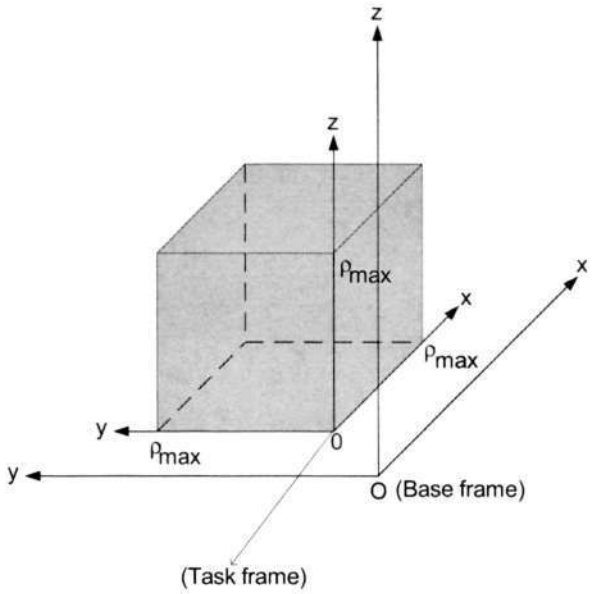

Figure 5.6: Maximal translational workspace of SA-PM

avoid leg interferences. The positional or orientational workspace at every orientation or position will therefore be different. Assume that the motion range of the passive P-joint is $[0, \rho_{max}]$, based on the forward kinematic algorithm, the reachable positional workspace will be a cube with edge of length ρ_{max}, as shown in Fig. 5.6. The transformation from the task frame to the base frame is:

$$T = \begin{bmatrix} 1 & 0 & 0 & L_1 - \rho_{max}/2 \\ 0 & 1 & 0 & L_1 - \rho_{max}/2 \\ 0 & 0 & 1 & L_1 - \rho_{max}/2 \\ 0 & 0 & 0 & 1 \end{bmatrix}. \tag{5.49}$$

Note that the reachable positional workspace may not be obtained at only one position of $\mathbb{R}^3$. The positional workspace envelope will be identical with the reachable positional workspace (Full-W_p) in optimization.

Dimension optimization for maximal workspace with satisfied conditioning

As the SA-PM has decoupled translation and rotation, and is isotropic when three actuators are in linear motion, the GCI here can be defined based on pure orientation as

$$GCI = \frac{\int_W C_I(J_r) dW}{\int_W dW}, \tag{5.50}$$

where W is the workspace volume of the complete 6-D workspace, and $J_r(= D^{-1} \cdot A)$ is the orientation Jacobian matrix. For the orientation of the end-effector of the SA-PM, each limb can be regarded as a virtual wrist, which means the orientation is only dependent on the geometry of s_{i1}, s_{i5} and s_{i6} without considering the limit of P-joints. If the passive P-joint limit is considered, the orientational workspace will be position-dependent. Our objective here is to obtain the optimal geometrical data for the maximal workspace with GCI larger than 0.1 meaning that the maximal to minimal velocity in the workspace will be different by ten times at most. By the inverse kinematics algorithm, the partition scheme of $SE(3)$ is applied to the SA-PM for evaluating its orientational workspace under each set of design parameters. As the objective function is highly nonlinear and is very difficult to formulate its derivatives, the complex algorithm is chosen for design optimization of the SA-PM. The complex algorithm is a direct multi-variable search method, and can pursue the optimal solution without strongly depending on the initial guess of the variables. The dimension optimization problem is defined as follows.

Design variables: β_1, β_2, β_3, γ, and ς, where β_1, β_2, β_3 are the Z-Y-Z Euler angles to represent the initial orientation of local frame $\{A_{i5}\}$ relative to local frame $\{A_{i4}\}$, γ is the relative angle between $O'A_{i5}$ and $O'A_{i6}$, and ς is the angle between $O'A_{i6}$ and $O'A_{j6}, (i \neq j; i, j = 1, 2, 3)$.

Objective function:

$$max \;\; W_r$$

Design constraints:

$$0 \leq \;\; \beta_1 \;\; < 2\pi, \tag{5.51}$$

$$0 \leq \;\; \beta_2 \;\; < \pi, \tag{5.52}$$

$$0 \leq \;\; \beta_3 \;\; < 2\pi, \tag{5.53}$$

$$0 < \;\; \gamma \;\; < \pi, \tag{5.54}$$

$$0 < \;\; \varsigma \;\; < 2/3\pi, \tag{5.55}$$

$$-10\ cm < \;\; \theta_{i3} \;\; < 10\ cm, (i = 1, 2, 3) \tag{5.56}$$

$$-10\ cm < \quad \theta_{i4} \quad < 10\ cm, \tag{5.57}$$

$$0.1 \quad < \quad GCI. \tag{5.58}$$

Table 5.1: Geometric data of SA-PM

$L_1(cm)$	$L_2(cm)$	$L_3(cm)$	$L_5(cm)$	$p_{4x}(cm)$	$p_{4y}(cm)$	$p_{4z}(cm)$	α	ρ_{max} (cm)
12	15	15	10	5	6	-15	$\pi/2$	20

The other geometry parameters are shown in Table 5.1. The optimization procedure is shown in Fig. 5.7.

Table 5.2 shows the computation-intensive optimization results based on the full positional workspace. It is difficult to implement the dimension optimization with very high resolution with large m and n due to the number of computed points increasing at exponential rate. One way to contain this problem is to make use of parallel processing on a cluster of computers, which is beyond our current scope for implementation. All current computations are run on a P4 2.6GHz computer.

Alternatively, to reduce the computation time, the reduced positional workspace (Diagonal-W_p) based on its diagonal elements as shown in Fig.5.8 is used in the optimization. Since the SA-PM bears a 3-limb symmetrical design with decoupled translation and rotation, both its orientational workspace and positional workspace will be symmetrical. The orientational workspace at different position is purely affected by the joint limits of the passive P-joints, i.e., the point on the diagonal line in the positional workspace as shown in Fig.5.8 corresponds to the maximal orientation workspace. In other words, the orientational workspace at other point on the same plane normal to the diagonal line will be a subspace of that of the corresponding point on the diagonal line. Therefore, we believe that the elements along the diagonal line can be used to represent the entire positional workspace in the optimization. Using the same approach except for the reduced number of feature points in the positional workspace, the optimal results are obtained as shown in Table 5.3. The comparison results (Table 5.4) between the two approaches show that the

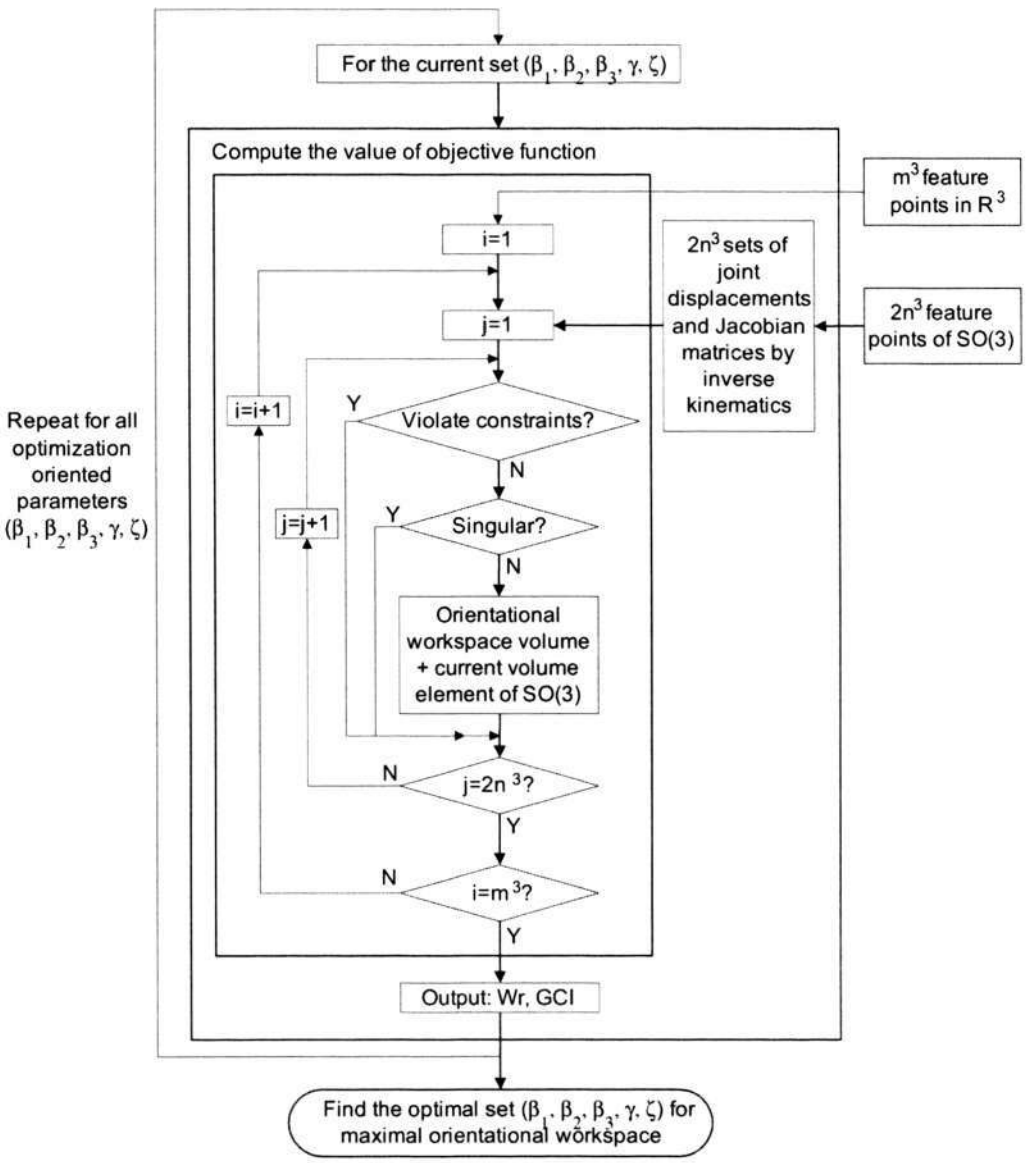

Figure 5.7: Procedure of the dimension optimization of SA-PM

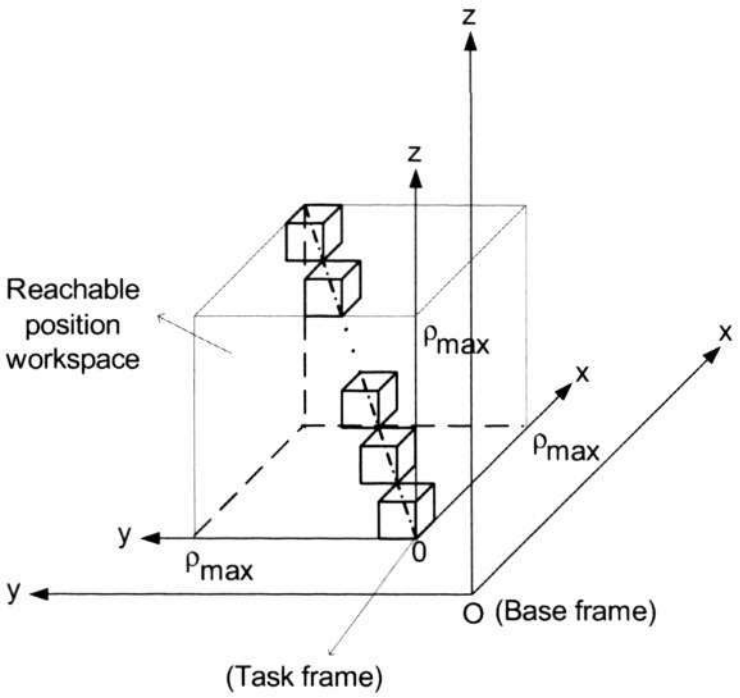

Figure 5.8: Reduced positional workspace for dimension optimization of SA-PM

set of optimal parameters over the entire positional workspace is only a little better than the other one since its GCI is better. Hence, the resultant optimal dimensions based on full positional workspace is selected as the optimal solutions.

Table 5.2: Optimization results over the complete 6-D workspace (Full-W_p)

i	m	n	t (hours)	W_r	GCI	β_1 (rad)	β_2 (rad)	β_3 (rad)	γ (rad)	ς (rad)
1	5	5	0.0337	4.25%	0.6160	0.0000	0.7261	3.8127	1.5267	1.8666
2	10	10	2.0840	4.20%	0.6121	0.0000	0.7261	3.8127	1.5267	1.8666
3	15	15	24.7290	4.10%	0.6054	0.0468	0.7261	3.8127	1.5732	1.5519

Table 5.3: Optimization results over the reduced workspace (Diagonal-W_p)

m	n	t (hours)	W_r	GCI	β_1 (rad)	β_2 (rad)	β_3 (rad)	γ (rad)	ς (rad)
40	40	84.8877	26.25%	0.6005	0.0384	0.5000	3.6000	1.5700	1.5000

Table 5.4: Comparison of optimization results

	β_1 (rad)	β_2 (rad)	β_3 (rad)	γ (rad)	ς (rad)	m	n	t (hours)	W_r	GCI
Full-W_p	0.0468	0.6051	3.8127	1.5732	1.5519	20	20	3.0071	4.15%	0.6047
Diagonal-W_p	0.0384	0.5000	3.6000	1.5700	1.5000	20	20	2.9977	4.15%	0.6017

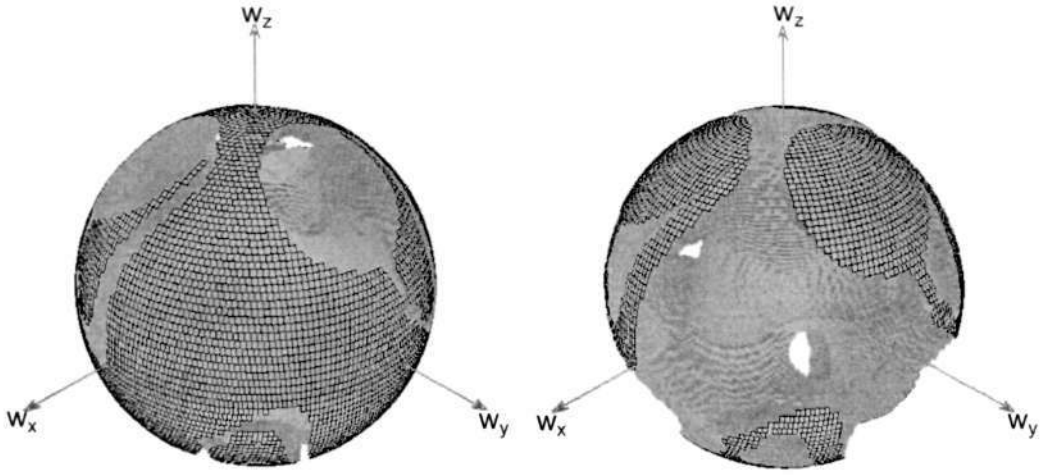

(a) Orientational workspace (b) Singularity zone

Figure 5.9: Orientational workspace of SA-PM before optimization

5.5.2 Determination of $\boldsymbol{p}_G$, R_G and GIP of SA-PM

With the optimal geometric parameters obtained in Section 5.5.1, points $\boldsymbol{p}_G$, R_G and GIP of the SA-PM can be easily obtained. The results indicate that there are 230 $\boldsymbol{p}_G$ points with the maximum orientational workspace (99.72%) in the reachable positional workspace. Taking one $\boldsymbol{p}_G$ point $(5.5, 5.5, 5.5)$ as an example, its orientational workspace before and after optimization are shown in Fig. 5.9 and Fig. 5.10 respectively. Note that the actual topology of the singularity loci should be 1-D manifold (like a curve) as shown in Fig. 5.10. Due to sampling resolution of the workspace representation and stop criteria of the numerical approach, the singularity loci look like volumetric 3-D manifold. The volume ratios of orientational workspaces before and after optimization to the entire $SO(3)$ space volume are 60.07% and 97.54% respectively, which shows that the orientational workspace has been significantly improved with acceptable GCI.

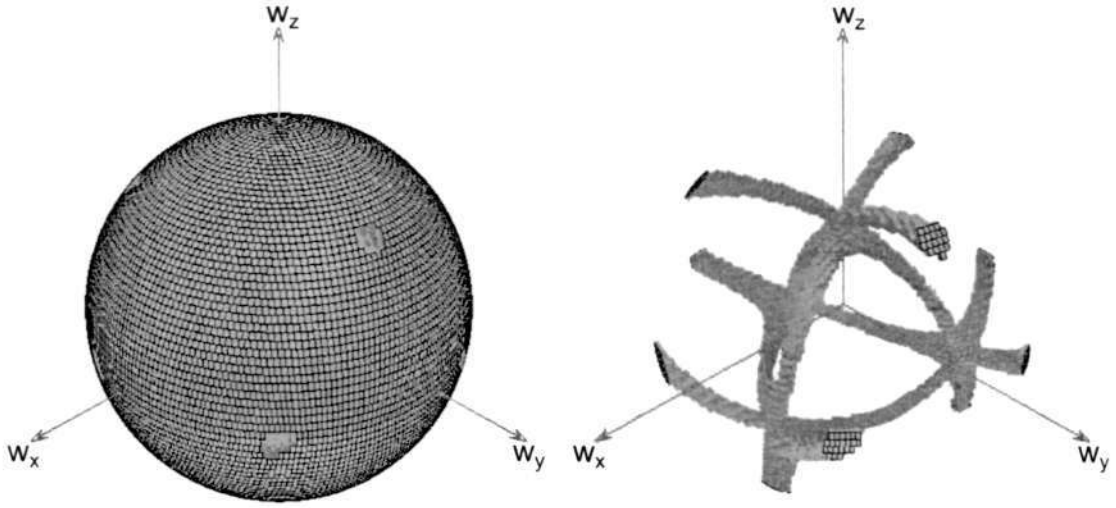

(a) Orientational workspace (b) Singularity manifold

Figure 5.10: Orientational workspace of SA-PM after optimization

The global orientation R_G is

$$R_G = \begin{bmatrix} -0.5820 & 0.5440 & 0.6044 \\ -0.0380 & 0.7242 & -0.6885 \\ -0.8123 & -0.4237 & -0.4008 \end{bmatrix}. \tag{5.59}$$

The corresponding positional workspace under this orientation is shown as Fig. 5.11 and its volume is about 6.36% of the positional workspace envelope. There will be many GIPs having the same orientation, and the condition index of each GIP point is 0.9976.

5.5.3 Dimension optimization of 3P3S PMs

For the 3P3S PMs, the orientational workspace will be different at various point in the positional workspace. Therefore, the positional workspace and the orientational workspace cannot be treated separately. In this section, the optimization algorithm will be developed to obtain the optimal dimensions of 3P3S PMs for maximal workspace with satisfied conditioning in the complete 6-D workspace.

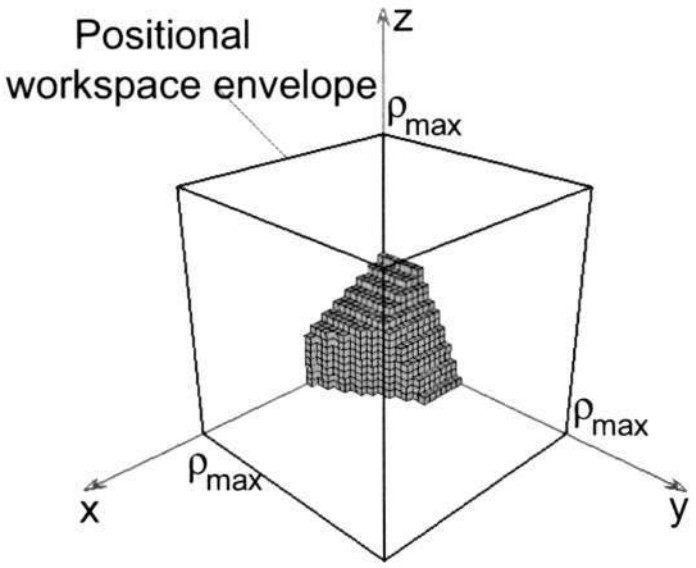

Figure 5.11: Positional workspace of R_G of SA-PM in the task frame

Reachable Positional Workspace of 3RPPS PMs

The reachable positional workspace is the set of the positions that the end-effector can reach with at least one orientation. Due to the structure properties of the family of 3P3S PMs, the reachable workspace in z-direction can be directly determined by the stroke of linear actuators. For the reachable workspace in the x-y plane, each PM can be regarded as a 3-DOF planar one accordingly. The workspace analysis of these 3-DOF planar PMs can be found in [81, 83]. The reachable workspace of the end-effector is the cross section of the reachable workspaces from the three limbs. Let r_1 and r_2 represent the radius of the base and moving platform respectively (Fig. 5.13), ρ_{pmin} and ρ_{pmax} represent respectively the distance from point A_{i2} to the proximal end and distal end that the passive joint can reach. The reachable positional workspace in x-y plane generated by each limb will be an annular plane, and can be expressed mathematically as:

$$(\rho_{pmin} - r_2)^2 \leq (x - x_{i1})^2 + (y - y_{i1})^2 \leq (\rho_{pmax} + r_2)^2 \quad for\ r_2 < \rho_{pmin}, \tag{5.60}$$

$$0 \leq (x - x_{i1})^2 + (y - y_{i1})^2 \leq (\rho_{pmax} + r_2)^2 \quad for\ r_2 \geq \rho_{pmin}. \tag{5.61}$$

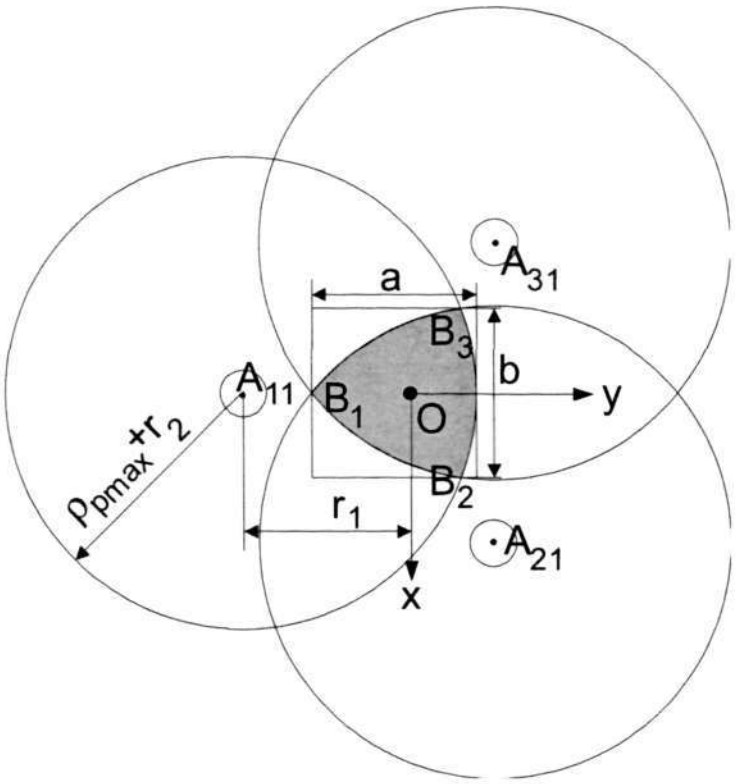

Figure 5.12: Reachable workspace in x-y plane of the 3RPPS PM

The reachable positional workspace of the end-effector in the $x-y$ plane, i.e., the intersection of the reachable workspace generated by the three limbs, will be the region in gray as shown in Fig. 5.12, for $r_2 < \rho_{pmin}$. If $r_2 \geq \rho_{pmin}$, the reachable workspace generated by each limb will be a complete area in the circle with radius of $\rho_{pmax} + r_2$, and the reachable workspace will have similar shape as shown in Fig. 5.12. Therefore, the reachable workspace of the 3RPPS PM is shown in Fig. 5.14, and can be mathematically represented as:

$$(\rho_{pmin} - r_2)^2 \leq (x - x_{i1})^2 + (y - y_{i1})^2 \leq (\rho_{pmax} + r_2)^2, \quad (i = 1, 2, 3), \tag{5.62}$$

$$h \leq z \leq h + \rho_a, \tag{5.63}$$

where h is the lowest position of the linear actuator relative to the base frame, and ρ_a represents the stoke of each linear actuator. Obviously, the longer the motion range of the passive P-joints and the larger the stroke of the linear actuator, the larger the reachable workspace.

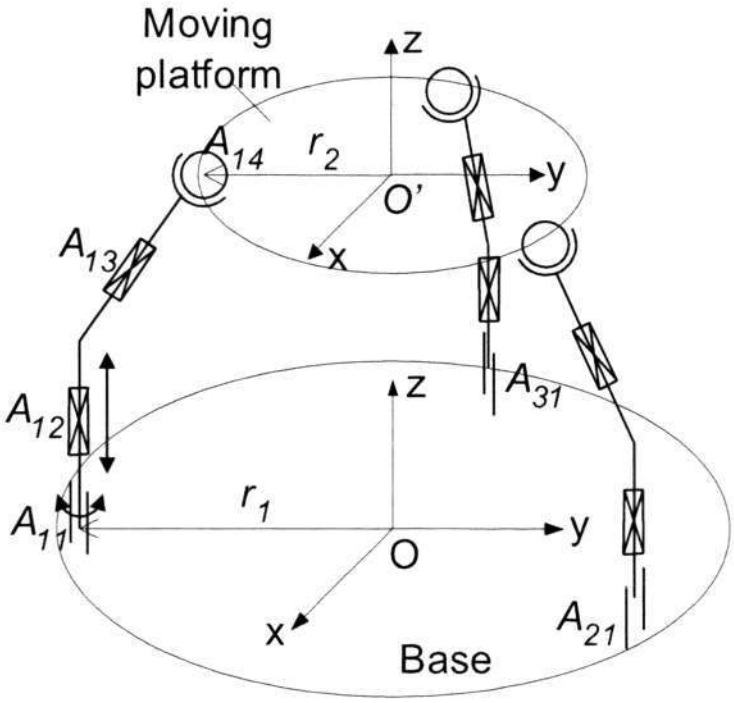

Figure 5.13: Schematic description of 3RPPS PM

For the optimization over the complete 6-D workspace, a suitable cube is required to accommodate the reachable positional workspace. Although we can select a large cube to enclose the complete reachable workspace, the computational time is a critical issue to consider. Therefore, we prefer to use a cuboid as small as possible to bound the reachable positional workspace. Let a, b and c are the lengths of the three edges of the cuboid. For the 3RPPS PM, the two edges a and b in the x-y plane can be defined as shown in Fig. 5.12. Let (x_{i1}, y_{i1}) be the coordinates of the point A_{i1} of the planar PM, the three larger circles can be represented by

$$x^2 + (y - y_{11})^2 = r_m^2, \tag{5.64}$$

$$(x - x_{21})^2 + (y - y_{21})^2 = r_m^2, \tag{5.65}$$

$$(x + x_{21})^2 + (y - y_{21})^2 = r_m^2, \tag{5.66}$$

where $r_m = \rho_{max} + r_2$. The position of the six intersecting points can be easily calculated, and the coordinates of the points $B_i(x_{Bi}, y_{Bi})$ are obtained as follows:

$$x_{B1} = 0, \tag{5.67}$$

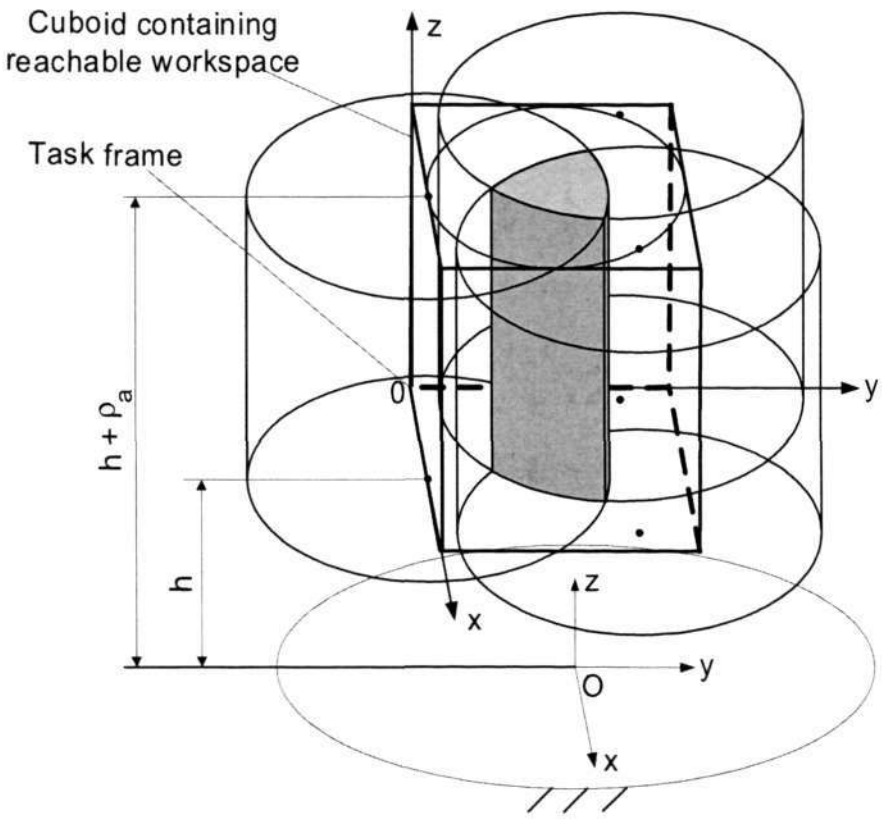

Figure 5.14: Reachable workspace of the 3RPPS PM

$$y_{B1} = -\sqrt{r_m^2 - x_{21}^2} + y_{21}, \tag{5.68}$$

$$y_{B2} = \frac{1}{2}\frac{2y_{11} - 2\cdot D\cdot E + 2\sqrt{-2y_{11}\cdot D\cdot E - D^2\cdot y_{11} + D^2\cdot r_m^2 - E^2 + r_m^2}}{D^2+1}, \tag{5.69}$$

$$(x + x_{21})^2 + (y - y_{21})^2 = r_m^2, \tag{5.70}$$

$$x_{B2} = D\cdot y_{B2} + E, \tag{5.71}$$

where $D = \frac{y_{11}-y_{21}}{x_{21}}$, $E = \frac{x_{21}^2+y_{21}^2-y_{11}^2}{2x_{21}}$. Therefore, the three edges a, b and c can be obtained as:

$$a = r_m - y_{B1} + y_{11}, \tag{5.72}$$

$$b = 2x_{B2}, \tag{5.73}$$

$$c = \rho_a. \tag{5.74}$$

Practically, the reachable workspace of the 3RPPS-PM should be contained by the solid cylinder whose bottom surface is a circle determined by the three points A_{11}, A_{21} and

A_{31}. Identical basis feature points are required for different set of design parameters in the optimization. Therefore, the cuboid bounding the solid cylinder as shown in Fig. 5.14 is taken as the positional workspace envelope in the optimization. The three edges a, b and c are obtained as:

$$a = 2r_1, \tag{5.75}$$

$$b = 2r_1, \tag{5.76}$$

$$c = \rho_a. \tag{5.77}$$

The transformation from the task frame to the base frame is:

$$T = \begin{bmatrix} 1 & 0 & 0 & -2r_1 \\ 0 & 1 & 0 & -2r_1 \\ 0 & 0 & 1 & h \\ 0 & 0 & 0 & 1 \end{bmatrix}. \tag{5.78}$$

Dimension optimization for maximal workspace with satisfied conditioning

Dimension optimization is to find the optimal dimensions for the moving platform and the base, to obtain maximal workspace with satisfied conditioning. As presented in Section 5.4, the optimization of the 3RPPS PMs will encounter the problems of inhomogeneous units and non-uniform actuators. To eliminate the problem of inhomogeneous units, all dimensions are normalized by the base radius r_1, and the ratio $\nu = r_2/r_1$ is defined as a design variable. To normalize the actuator inputs, $\xi = \tau_1/\tau_2$ is defined as the capability ratio of a rotary actuator to a linear actuator another design variable. For the 3RPPS PM, eqn. (5.26) can be written as follows:

$$\boldsymbol{F} = J^T \cdot \boldsymbol{\tau} = J^T \cdot J_s \cdot \boldsymbol{\tau}^*, \tag{5.79}$$

where

$J_s = diag[\xi \quad \xi \quad \xi \quad 1 \quad 1 \quad 1]$, $\boldsymbol{\tau} = [\tau_1 \quad \tau_1 \quad \tau_1 \quad \tau_2 \quad \tau_2 \quad \tau_2]^T$, and

$\boldsymbol{\tau}^* = [\tau_2 \quad \tau_2 \quad \tau_2 \quad \tau_2 \quad \tau_2 \quad \tau_2]^T$.

The normalized Jacobian matrix is $J^* = J^T \cdot J_s$, which is used to find the condition

Table 5.5: Optimization results

i	m	n	t (hours)	W_r	GCI	ν	ξ
1	5	5	0.6395	7.74%	0.1003	0.2701	0.4634
2	10	10	25.5661	6.77%	0.1201	0.2500	0.6640

index of the manipulator. The optimal ξ value will give us the best coordination of linear and rotary actuators. Practically, the spherical joints always have their physical limits, which will greatly influences the volume of the workspace. The Hook-type spherical joint is considered here, and its tilting angle is in $[-\pi/2, \pi/2]$, and the spin angle, i.e., along the axis $\boldsymbol{s}_{i3}$, has no limits. Mathematically, the spherical joint limits can be expressed as follows:

$$\angle(\boldsymbol{s}_{i3} \cdot \boldsymbol{A_{i4}O'}) \in [0, \pi/2]\,. \tag{5.80}$$

The normalized stroke of linear actuator and the passive joint limit are $\rho_a \in [0, 2]$ and $\rho_p \in [\rho_{pmin}, \rho_{pmax}] = [0.2, 2]$ respectively. The design objective is to maximize the 6-D workspace volume with satisfied conditioning, i.e., $GCI \geq 0.1$. Therefore, the optimization problem can be defined as follows:

Design variables: ν and ξ

Design objective: $max \;\; W_r$,

Design constraints: $1/4 \leq \nu \leq 3/4$,

$0 \leq \xi \leq 10$,

$\angle(\boldsymbol{s}_{i3} \cdot \boldsymbol{A_{i4}O'}) \in [0, \pi/2]$.

The complex optimization strategy is employed, and is shown in Fig. 5.15. Table 5.5 shows the optimization results with two sets of m and n, which indicate that the algorithm is also computational intensive. Table 5.6 lists the performance value of the 3RPPS PM before and after optimization, which indicates that the workspace volume is improved 130.51% with satisfied conditioning by optimization.

Table 5.6: Comparison of results before and after optimization

	ν	μ	m	n	W_r	GCI
after optimization	0.2500	0.6640	20	20	6.80%	0.1001
before optimization	0.5000	1.0000	20	20	2.95%	0.1475

5.5.4 Determination of $\boldsymbol{p}_G$, R_G and GIP of 3RPPS PM

With the optimal geometric parameters obtained in Section 5.5.3, $\boldsymbol{p}_G$, R_G and GIP of the 3RPPS PM can be easily obtained as shown in the Tables 5.7, 5.8 and 5.9 respectively. Taking one $\boldsymbol{p}_G$ $(-0.05,\ 0.05,\ 1.07)$ point as an example, its corresponding orientation workspace is shown in Fig. 5.16. The orientation workspace volume is 16.94% of the entire $SO(3)$ workspace. The position workspace of the two R_G points are shown in Fig. 5.17, and their volume are both 54.99% of the positional workspace envelope. Two GIP points are obtained as shown in Table 5.9. The maximum condition index in the workspace is 0.4540.

Table 5.7: $\boldsymbol{p}_G$ of 3RPPS PM ($Wr = 16.94\%,\ m = n = 20,\ t = 14.2072$ hours)

i	$\boldsymbol{p}_G$	i	$\boldsymbol{p}_G$	i	$\boldsymbol{p}_G$
1	−0.0500 0.0500 0.0700	11	−0.0500 0.0500 1.0700	21	0.0500 0.0500 0.5700
2	−0.0500 0.0500 0.1700	12	−0.0500 0.0500 1.1700	22	0.0500 0.0500 0.6700
3	−0.0500 0.0500 0.2700	13	−0.0500 0.0500 1.2700	23	0.0500 0.0500 0.7700
4	−0.0500 0.0500 0.3700	14	−0.0500 0.0500 1.3700	24	0.0500 0.0500 0.8700
5	−0.0500 0.0500 0.4700	15	−0.0500 0.0500 1.4700	25	0.0500 0.0500 0.9700
6	−0.0500 0.0500 0.5700	16	0.0500 0.0500 0.0700	26	0.0500 0.0500 1.0700
7	−0.0500 0.0500 0.6700	17	0.0500 0.0500 0.1700	27	0.0500 0.0500 1.1700
8	−0.0500 0.0500 0.7700	18	0.0500 0.0500 0.2700	28	0.0500 0.0500 1.2700
9	−0.0500 0.0500 0.8700	19	0.0500 0.0500 0.3700	29	0.0500 0.0500 1.3700
10	−0.0500 0.0500 0.9700	20	0.0500 0.0500 0.4700	30	0.0500 0.0500 1.4700

Table 5.8: R_G of 3RPPS PM ($Wr = 54.99\%,\ m = n = 20,\ t = 14.2083$ hours)

i	R_G	i	R_G
1	$\begin{bmatrix} 0.9881 & 0.1059 & 0.1118 \\ -0.1240 & 0.9776 & 0.1700 \\ -0.0913 & -0.1819 & 0.9791 \end{bmatrix}$	2	$\begin{bmatrix} 0.9881 & -0.1059 & -0.1118 \\ 0.1240 & 0.9776 & 0.1700 \\ 0.0913 & -0.1819 & 0.9791 \end{bmatrix}$

Table 5.9: GIP of 3RPPS PM ($m = n = 20,\ CI = 0.4540,\ t = 14.1762$ hours)

i	T	i	T
1	$\begin{bmatrix} 1 & 0 & 0 & -0.05 \\ 0 & 1 & 0 & -0.05 \\ 0 & 0 & 1 & 0.07 \\ 0 & 0 & 0 & 1 \end{bmatrix}$	2	$\begin{bmatrix} 1 & 0 & 0 & 0.05 \\ 0 & 1 & 0 & -0.05 \\ 0 & 0 & 1 & 0.07 \\ 0 & 0 & 0 & 1 \end{bmatrix}$

5.6 Summary

In this chapter, a finite-partition approach for parametrical and proportional partition of $SE(3)$ is introduced based on its topology, which is the product of $\mathbb{R}^3$ and $SO(3)$. It is known that the Special Orthogonal group $SO(3)$ is homeomorphic to a solid ball D^3 with antipodal points identified while the geometry of $\mathbb{R}^3$ can be regarded as a cube. Furthermore the solid ball and the cube can be parametrically and proportionally partitioned into a number of elements. Therefore, a basis volume element of $SE(3)$ is the product of two basis volume elements of $\mathbb{R}^3$ and $SO(3)$ respectively. By this way, the integration of the complete 6-D workspace volume is transformed into the simple summation of the basis volume elements of $SE(3)$. Based on this finite-partition method, two performance indices and three optimal points are defined over the complete 6-D workspace. Two algorithms are developed for the dimension optimization of the SA-PM and the 3RPPS-PM respectively with the first two indices. As a result, the optimization approach is valid although it is computationally intensive. The $\boldsymbol{p}_G$, R_G and GIP of the two PMs with optimal dimensions are obtained. The results show that they can be used to objectively evaluate the performance of a manipulator.

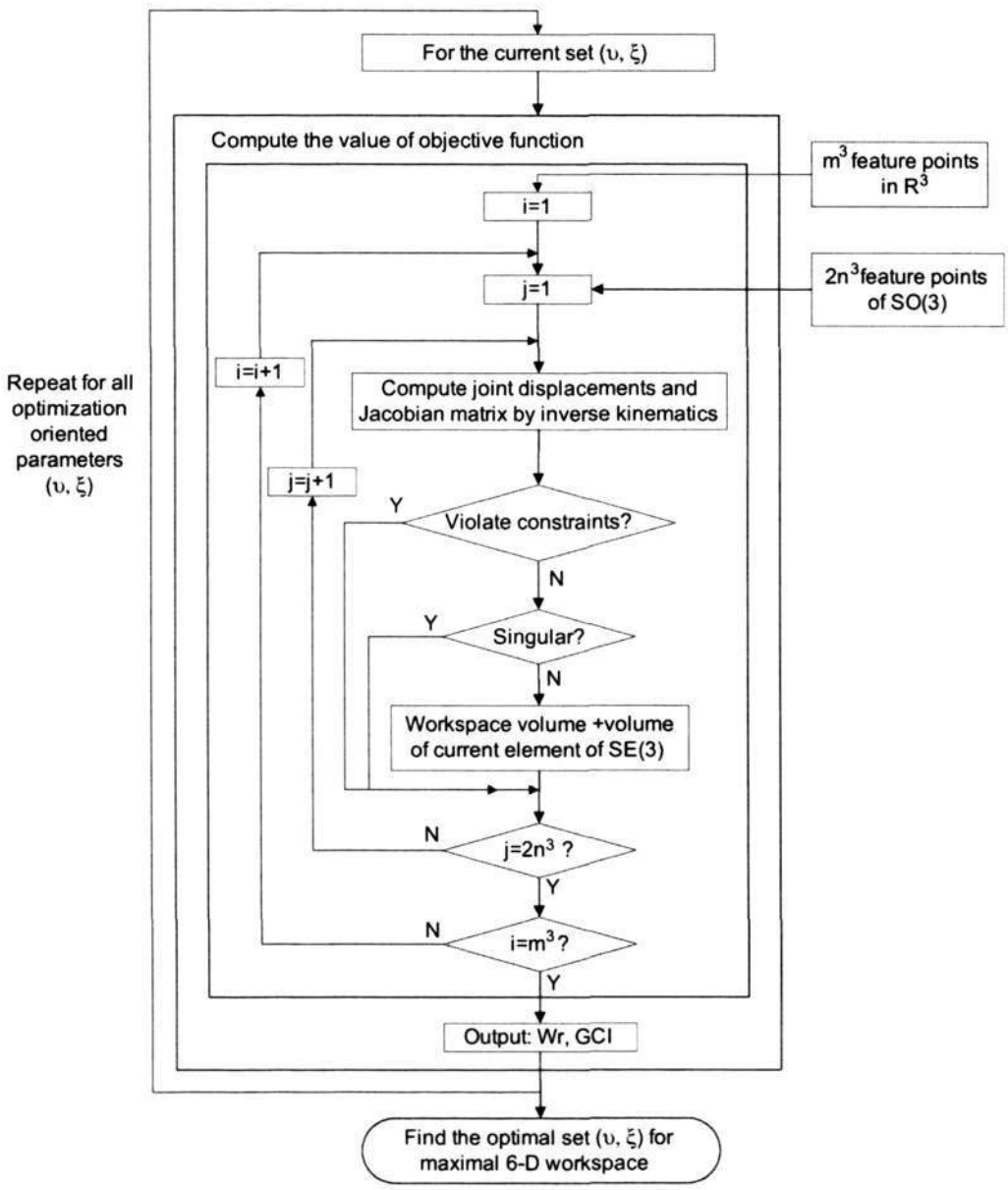

Figure 5.15: Dimension optimization procedure of 3RPPS PM

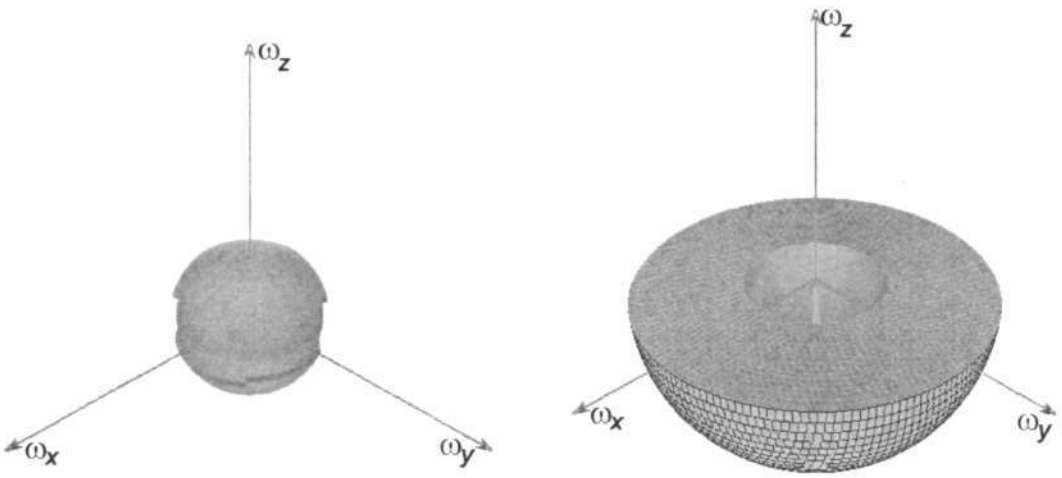

(a) Orientational workspace (b) Singularity zone (lower half)

Figure 5.16: Orientational workspace of $\boldsymbol{p}_G(-0.05, 0.05, 1.07)$

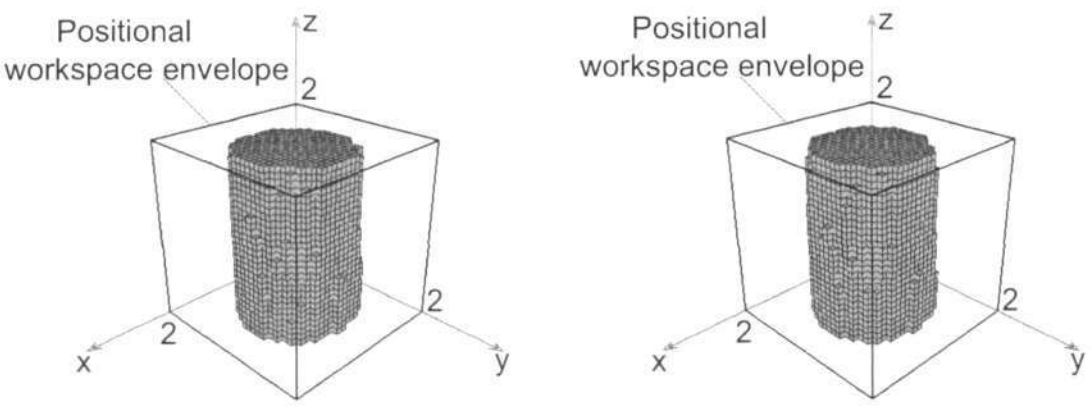

(a) $R_G(1)$ (b) $R_G(2)$

Figure 5.17: Positional workspace of the two R_Gs in the task frame

Chapter 6

Statics and Stiffness Analysis

Static force analysis is of practical importance in evaluating the force transmission through the manipulator joints and links. When a manipulator performs a given task, such as forging and pressing a workpiece, its end-effector will exert force and moments to the external environment. The force and moments (also called generalized force in [81]) are generated by actuators and transformed by the mechanical structure. For a manipulator design, it is essential to specify the maximum force and moments that the end-effector can perform. The maximum force and moment output is an important measure to select a PM for specific tasks.

Stiffness is an important criterion for evaluate robot performance when the end-effector exerts force and moments to its environment. The external force and moments will lead to the deflection of the mechanism so that the end-effector will be deflected away from the desired pose. Therefore, the stiffness will give an immediate impact on the positioning accuracy of a manipulator. Some control algorithms make use of the stiffness characteristics for accurately controlling a robot manipulator. The overall stiffness of a manipulator depends on several factors, including the mechanical structure, the dimensions and the materials of the links and the actuators. Especially when the links or joints are more compliant, the stiffness of the entire manipulator become the major concern. Due to the complex structure and multiple joints of PMs, the stiffness analysis become the critical

issue in manipulator design.

In this chapter, both statics and stiffness properties of the decoupled PMs are studied. Section 6.1 briefly introduced the latest research efforts on statics and stiffness of PMs. Section 6.2 introduced statics and stiffness of the SA-PM, which shows that the contribution from the position and that of orientation can be independently calculated when a proper reference frame is chosen. The statics and the stiffness of the 3P3S-PMs are studied in Section 6.3.

6.1 Introduction

It is generally complicated to determine the force transmission of the parallel manipulators, which relies on the mechanical structure. The problem becomes more complex if elasticity of every component is considered. To reduce the complexity of stiffness problem, only the driving forces and moments are of interest in most robotics literatures [4, 19, 29, 80, 102, 106]. Some researchers argued that the simplified theoretical stiffness model is very close to their experimental results [19, 106].

Agrawal and Roth [4] established a framework for studying the statics of general PM systems based on the duality of the screw. Four classes of serial chains are classified based on the instantaneous configuration, and the correspondence between reciprocal screw and joint torques of each class of kinematic chains are obtained. Based on these correspondence, the general condition to determine the controllability from a set of actuators are obtained. The conditions of static singularities, i.e., configurations losing the static equilibrium under at least one external force/moment, were also presented. Many researchers investigated manipulator statics by applying the virtual work principles. Merlet presented an efficient algorithm for determining the extremal joint forces of the Stewart-Gough type of PM [80]. Gosselin studied the statics and proposed a stiffness mapping method for PMs with rigid links [29]. In this method, the stiffness matrix of a PM is related to the Jacobian

matrix and the spring constants of actuators. Based on the stiffness matrix, the stiffness maps in the workspace of the manipulator can be obtained, which will help the designer to have a better understanding of the properties of the manipulator. Griffis and Duffy [36] proposed an approach for global stiffness modeling of compliant couplings which consist of translational springs acting in-parallel. This approach is applicable for the stiffness mapping of both planar and spatial manipulators. The resulting stiffness matrices show that they are functions of the configuration of their respective compliant couplings, and is possible to have asymmetric stiffness mappings for compliant devices. Huang and Schimmel [41] proposed a method to realize an arbitrary spatial elastic behavior by using an elastic mechanism with concurrent axes. The study showed that any full-rank spatial stiffness matrix can be realized by a PM with all spring axes intersecting at a common point, and any full-rank compliance matrix can be realized by a serial mechanism with all joint axes intersecting at a common point. Gosselin and Zhang [31] proposed an approach for stiffness analysis of PMs using a lumped parameter model. In this lumped model, the compliance of links are replaced by virtual joints and rigid links. Two different methods were introduced for the formulation of the stiffness models for rigid mechanisms and flexible mechanisms respectively. Using these stiffness models, the stiffness contour graphs can be obtained. A 6-DOF PM example showed that when the link stiffness is sufficiently large, the stiffness of the PM with flexible links is very close to that of the PM with rigid links. Ceccarelli and Carbone [14] studied the stiffness characteristics of a 3-DOF PM (CaPaMan). The stiffness matrix is formulated based on the structure analysis, and numerical results are presented for the PM. Specially, the determinant of the stiffness matrix is used as a stiffness performance index. Other works of stiffness of PMs can be seen in [24, 42, 96]

6.2 Statics and Stiffness Analysis of SA-PM

6.2.1 Maximal Generalized Force of SA-PM

According to the principle of virtual work, the output force system $\boldsymbol{F} = \begin{bmatrix} \boldsymbol{n} \\ \boldsymbol{f} \end{bmatrix}$ ($\boldsymbol{n}$ represents moment and $\boldsymbol{f}$ represents force) by the end-effector, and all the active forces or moments on the actuators, $\boldsymbol{\tau} = [\,\tau_1 \quad \tau_2 \quad \cdots \quad \tau_n\,]^T$, are related by Jacobian matrix as follows:

$$\boldsymbol{F} = J^T \boldsymbol{\tau}, \tag{6.1}$$

where $J = J_\theta^{-1} J_x$. In designing a manipulator, one may want to find the force distribution and the maximum generalized forces that can be generated by the manipulator when the active force/moments are bounded. Assume that $\|\boldsymbol{\tau}\| \leq 1$, with the help of eqn. (6.1), we have

$$\boldsymbol{F} J^{-1} J^{-T} \boldsymbol{F} \leq 1. \tag{6.2}$$

Taking J_x and J_θ obtained in Section 3.2.3, we have

$$J = J_\theta^{-1} J_x = \begin{bmatrix} D^{-1} \cdot A & 0 \\ 0 & C \end{bmatrix}, \tag{6.3}$$

where $A = [\,\boldsymbol{s}_{15} \times \boldsymbol{s}_{16} \quad \boldsymbol{s}_{25} \times \boldsymbol{s}_{26} \quad \boldsymbol{s}_{35} \times \boldsymbol{s}_{36}\,]^T$,

$C = [\,\boldsymbol{s}_{11} \quad \boldsymbol{s}_{21} \quad \boldsymbol{s}_{31}\,]^T$,

$D = diag\,[(\boldsymbol{s}_{15} \times \boldsymbol{s}_{16})\boldsymbol{s}_{11}, (\boldsymbol{s}_{25} \times \boldsymbol{s}_{26})\boldsymbol{s}_{21}, (\boldsymbol{s}_{35} \times \boldsymbol{s}_{36})\boldsymbol{s}_{31}]$.

Due to the decoupling characteristics of the SA-PM, eqn. (6.1) can be written as

$$\boldsymbol{n} = J_r \boldsymbol{\tau}_1, \tag{6.4}$$

$$\boldsymbol{f} = J_p \boldsymbol{\tau}_2. \tag{6.5}$$

where J_r and J_p are the Jacobian matrices related to the orientation and position respectively, $\boldsymbol{\tau}_1 = [\,\tau_{11} \quad \tau_{21} \quad \tau_{31}\,]^T$ represents the rotary actuator torques, and $\boldsymbol{\tau}_2 = [\,\tau_{12} \quad \tau_{22} \quad \tau_{32}\,]^T$ the forces from the three linear actuators, $J_r = D^{-1} \cdot A$ and $J_p = C$ (refer to eqn. (3.8)). As shown in Section 3.2.3, by suitably defining the coordinate frame

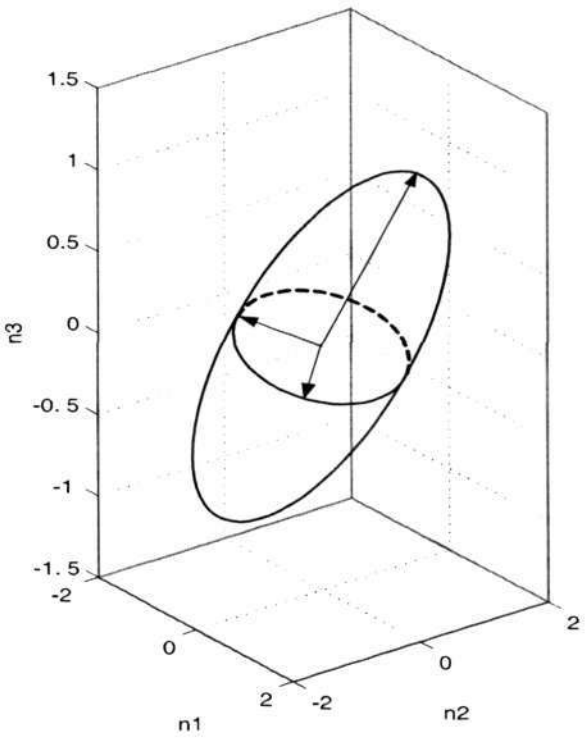

Figure 6.1: Generalized moment ellipsoid of the GIP of SA-PM

and mounting actuators orthogonally J_p is an identity matrix. The end-effector output force are identical with the linear actuator inputs. Therefore, only the torques that the end-effector can output are of our concern. Equation. (6.2) thus becomes

$$\boldsymbol{n}^T J_r^{-1} J_r^{-T} \boldsymbol{n} \leq 1. \tag{6.6}$$

Equation (6.6) represents a three-dimensional moment ellipsoid. Because $J_r^{-1} J_r^{-T}$ is a symmetric positive semi-definite matrix, its eigenvectors are orthogonal to each other. The principal axes of the ellipsoid coincide with the eigenvectors of $J_r^{-1} J_r^{-T}$, and their lengths are equal to the reciprocals of the square roots of the eigenvalues. Fig. 6.1 shows the generalized moment ellipsoid of the GIP $(0.05, -0.05, 0.07)$ when the joint torque are limited by $\|\boldsymbol{\tau}_1\| \leq 1$.

6.2.2 Stiffness Evaluation

Let $\boldsymbol{\Delta\theta}$ be the vector of actuator joint displacements. We can relate $\boldsymbol{\Delta\theta}$ and $\boldsymbol{\tau}$ by an $n \times n$ diagonal matrix as follows:

$$\boldsymbol{\tau} = \chi \boldsymbol{\Delta\theta}, \tag{6.7}$$

where $\chi = diag[k_1, k_2, \ldots, k_n]$ is spring constants related to the actuators.

For a parallel manipulator, the displacements of actuators $\boldsymbol{\Delta\theta}$ is related to the displacements of end-effector $\boldsymbol{\Delta X}$ by the Jacobian matrix as follows:

$$\Delta\boldsymbol{\theta} = J\Delta\boldsymbol{X}, \tag{6.8}$$

Substituting eqn.(6.8) into eqn.(6.7), and then into eqn.(6.1), we have

$$\boldsymbol{F} = K\boldsymbol{\Delta X}, \tag{6.9}$$

where

$$K = J^T \chi J, \tag{6.10}$$

is the stiffness matrix of the parallel manipulator.

As shown in [74], the condition index of the stiffness matrix, $C_I(K)$, can be used to represent the stiffness property of a PM. The larger the condition index of the stiffness matrix, the more uniform distribution of the stiffness in all directions. Therefore, $C_I(K)$ can help the designer to reveal the workspace stiffness properties for task operations.

Let k_r represent the stiffness of the rotary actuators, and k_l the stiffness of the linear actuators, the stiffness matrix K can be written as

$$K = \begin{bmatrix} D^{-1} \cdot A & 0 \\ 0 & C \end{bmatrix}^T \cdot \begin{bmatrix} k_r & 0 & 0 & 0 & 0 & 0 \\ 0 & k_r & 0 & 0 & 0 & 0 \\ 0 & 0 & k_r & 0 & 0 & 0 \\ 0 & 0 & 0 & k_l & 0 & 0 \\ 0 & 0 & 0 & 0 & k_l & 0 \\ 0 & 0 & 0 & 0 & 0 & k_l \end{bmatrix} \cdot \begin{bmatrix} D^{-1} \cdot A & 0 \\ 0 & C \end{bmatrix}. \tag{6.11}$$

Equation (6.11) shows that the stiffness matrix including two 3×3 sub-matrices which represent the torsional stiffness K_r and the translational stiffness K_l of the PM respectively, and all the coupling coefficients are zero. Hence, eqn. (6.11) can be expanded into two equations as

$$\begin{cases} K_r = k_r \cdot (D^{-1} \cdot A)^T \cdot D^{-1} \cdot A \\ K_l = k_l \cdot C^T \cdot C \end{cases} . \tag{6.12}$$

Equation (6.12) shows that the translational stiffness matrix is a constant matrix determined by the location of the three linear actuators, and the direction of the reference frame. Therefore, for maximal translational stiffness in x-, y- and z- directions, the three actuators should be located mutually orthogonal and the coordinates of the reference frame should be along the three actuator axes respectively. Then we have the translational stiffness $K_l = k_l \cdot I$, where I is a 3×3 identity matrix. In other words, the translational stiffnesses in x-, y- and z- directions of SA-PM are identical with the stiffness of the three linear actuators.

In the orientation workspace, the stiffness property of the SA-PM is evaluated by using the stiffness condition index $C_I(K_r)$ with optimal geometry parameters obtained in Section 5.5.1. The orientation of the end-effector is represented by three parameters, w_x, w_y and w_z as described in Section 5.2. Fig. 6.2 and Fig. 6.3 show the stiffness contours of the SA-PM in its orientation workspace with different value of w_z. The stiffness distribution of the entire orientation workspace is revealed by this way, so that we can easily find the orientation workspace with the best uniform stiffness property, e.g., the central zone of Fig. 6.2(a), (d) and (e).

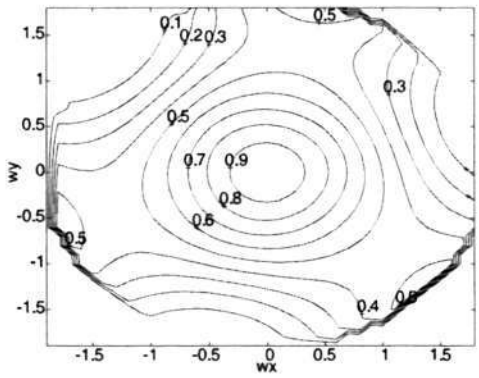

(a) $w_z = -2.5$

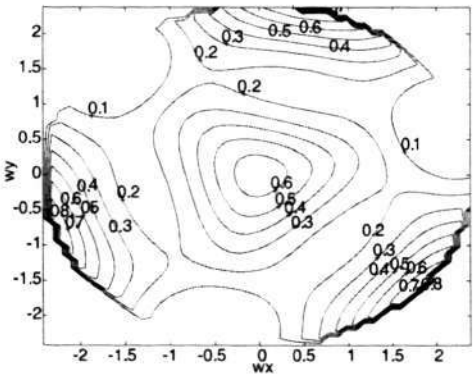

(b) $w_z = -2.0$

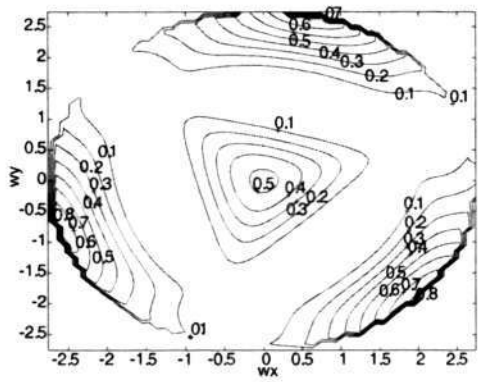

(c) $w_z = -1.5$

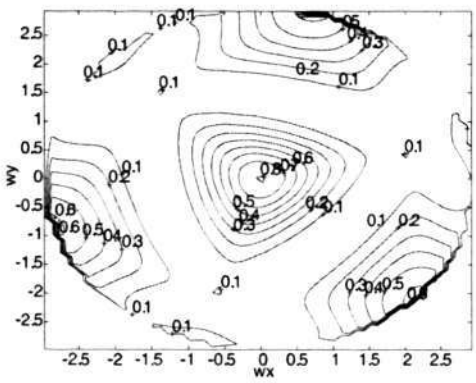

(d) $w_z = -1$

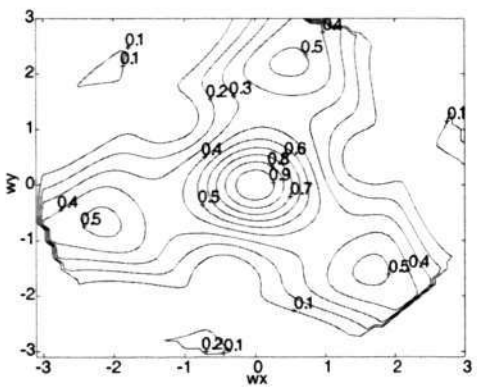

(e) $w_z = -0.5$

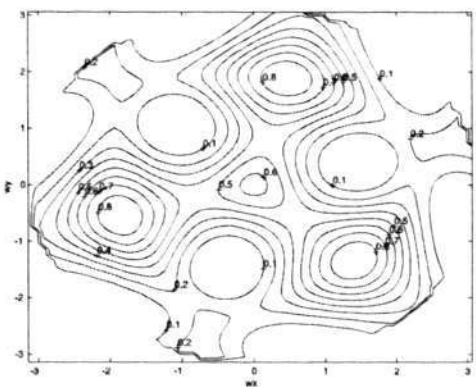

(f) $w_z = 0$

Figure 6.2: Stiffness contours $(C_I(K_r))$ of $\boldsymbol{p}_G$ of SA-PM

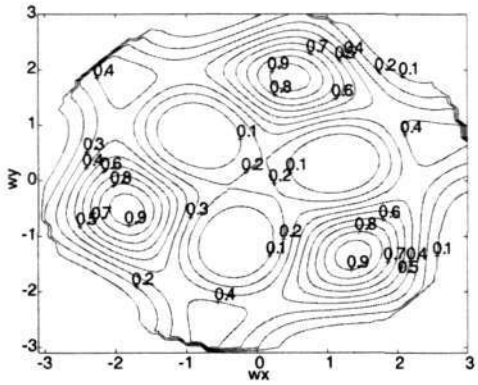

(a) $w_z = 0.5$

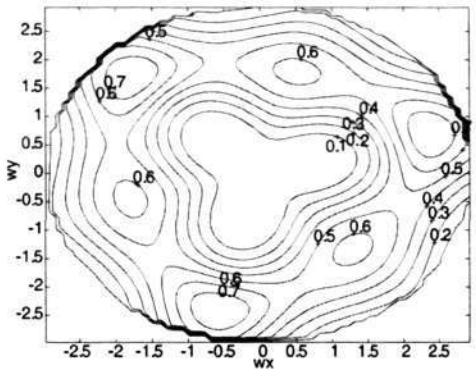

(b) $w_z = 1$

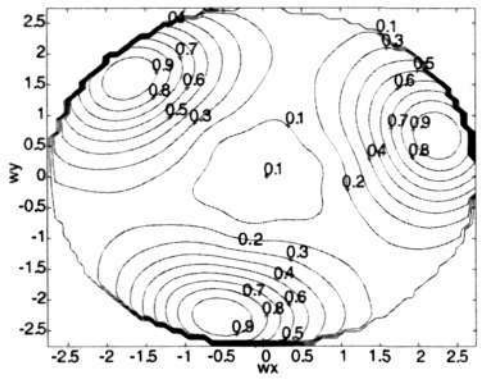

(c) $w_z = 1.5$

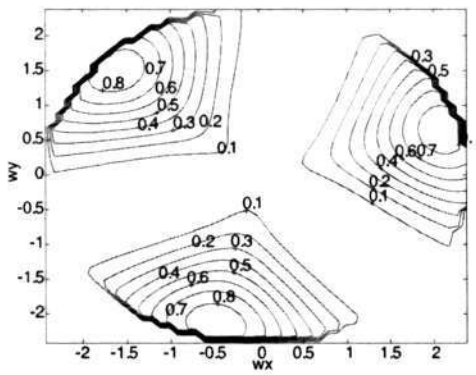

(d) $w_z = 2.0$

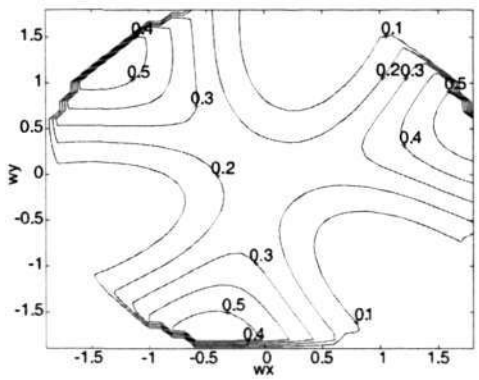

(e) $w_z = 2.5$

Figure 6.3: Stiffness contours ($C_I(K_r)$) of $\boldsymbol{p}_G$ of SA-PM

6.3 Statics and Stiffness Analysis of 3RPPS PM

6.3.1 Maximal Generalized Force of 3RPPS PM

With manipulator Jacobians J_x and J_θ obtained in Section 3.3.1, the Jacobian matrix, $J = J_\theta^{-1} \cdot J_x$, can be directly computed by

$$J = \begin{bmatrix} t_{11} & t_{12} & 0 & t_{14} & t_{15} & t_{16} \\ t_{21} & t_{22} & 0 & t_{24} & t_{25} & t_{26} \\ t_{31} & t_{32} & 0 & t_{34} & t_{35} & t_{36} \\ 0 & 0 & 1 & t_{44} & t_{45} & 0 \\ 0 & 0 & 1 & t_{54} & t_{55} & 0 \\ 0 & 0 & 1 & t_{64} & t_{65} & 0 \end{bmatrix}, \tag{6.13}$$

where

$t_{i1} = (y_{i3} - y_{i4})/A_i, (i = 1, 2, 3),$

$t_{i2} = (x_{i4} - x_{i3})/A_i,$

$t_{i4} = z_{i4}(x_{i3} - x_{i4})/A_i,$

$t_{i5} = z_{i4}(y_{i3} - y_{i4})/A_i,$

$t_{i6} = (x_{i4}(x_{i4} - x_{i3}) - y_{i4}(y_{i3} - y_{i4}))/A_i,$

$t_{j4} = y_{j4}, (j = 4, 5, 6),$

$t_{j5} = -x_{j4}.$

$A_i = (y_{i1} - y_{i4})(y_{i3} - y_{i4}) + (x_{i4} - x_{i1})(x_{i4} - x_{i3}),\ (i = 1, 2, 3)$

Based on eqn. (6.1) the output force $\boldsymbol{F} = [\, f_1 \quad f_2 \quad f_3 \quad n_1 \quad n_2 \quad n_3 \,]^T$ can individually controlled by the actuator input in the following manner:

$$\begin{bmatrix} f_1 \\ f_2 \\ n_3 \end{bmatrix} = \begin{bmatrix} t_{11} & t_{12} & t_{31} \\ t_{12} & t_{22} & t_{32} \\ t_{16} & t_{26} & t_{36} \end{bmatrix} \cdot \begin{bmatrix} \tau_{11} \\ \tau_{21} \\ \tau_{31} \end{bmatrix}, \tag{6.14}$$

$$f_3 = \tau_{12} + \tau_{22} + \tau_{32}, \tag{6.15}$$

$$\begin{bmatrix} n_1 \\ n_2 \end{bmatrix} = \begin{bmatrix} t_{14} & t_{24} & t_{34} & t_{44} & t_{54} & t_{64} \\ t_{15} & t_{25} & t_{35} & t_{45} & t_{55} & t_{65} \end{bmatrix} \cdot \begin{bmatrix} \tau_{11} \\ \tau_{21} \\ \tau_{31} \\ \tau_{12} \\ \tau_{22} \\ \tau_{32} \end{bmatrix}, \tag{6.16}$$

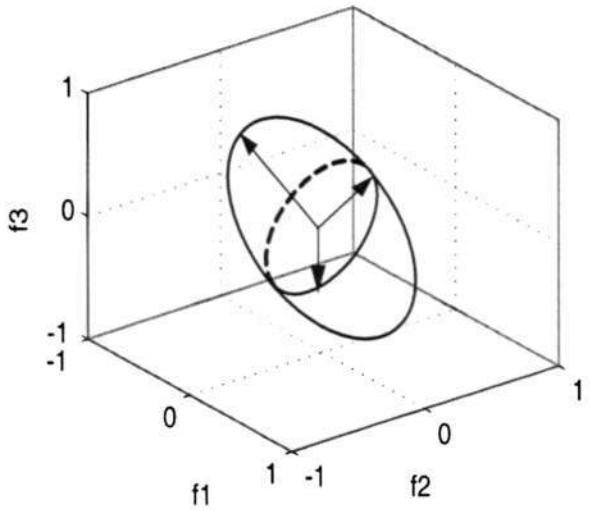

Figure 6.4: Generalized force ellipsoid of the GIP of 3RPPS PM

where τ_{i1} and τ_{i2} $(i = 1, 2, 3)$ represent the rotary actuator torques and the linear actuator forces of the three limbs respectively. Equations (6.14)$\sim$(6.16) show that the output force/moment can be easily computed with given actuator input, or vice versa. The force along the z-axis of the base frame f_3 is the summation of the force inputs from the three linear actuators. The two forces parallel to the base plane (f_1 and f_2) and the moment about the z-axis (n_3) is determined by the inputs from the three rotary actuators. The moments about x- and y- axes are contributed by all actuator inputs. Based on eqn. (6.2), Figures 6.4 and 6.5 illustrate the generalized force and moment ellipsoid of the GIP of the 3-RPPS PM by the normalized Jacobian matrix J^* when the joint force and torque are bounded ($\|\boldsymbol{\tau} * \| \leq 1$). The pose of the GIP is

$$GIP = \begin{bmatrix} 1 & 0 & 0 & 0.05 \\ 0 & 1 & 0 & -0.05 \\ 0 & 0 & 1 & 0.07 \\ 0 & 0 & 0 & 1 \end{bmatrix}. \tag{6.17}$$

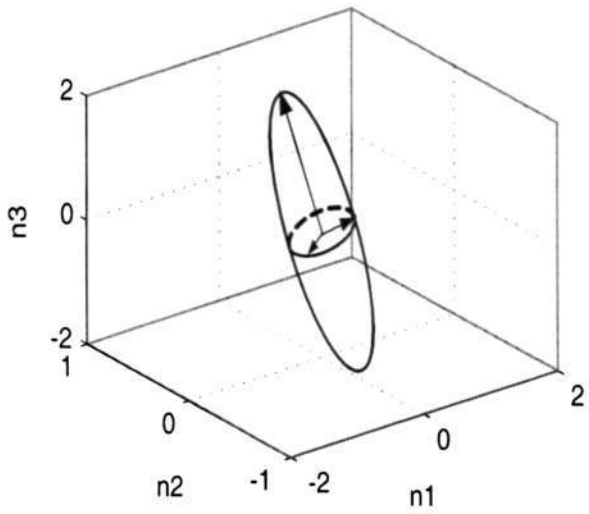

Figure 6.5: Generalized moment ellipsoid of the GIP of 3RPPS PM

6.3.2 Stiffness Evaluation

Let k_r represent the stiffness of the rotary actuators, and k_l represent the stiffness of the linear actuators, the stiffness matrix K (eqn. (6.10)) can be written as

$$K = \begin{bmatrix} K_{11} & K_{12} & 0 & K_{14} & K_{15} & K_{16} \\ K_{12} & K_{22} & 0 & K_{24} & K_{25} & K_{26} \\ 0 & 0 & K_{33} & K_{34} & K_{35} & 0 \\ K_{14} & K_{24} & K_{34} & K_{44} & K_{45} & K_{46} \\ K_{15} & K_{25} & K_{35} & K_{45} & K_{55} & K_{56} \\ K_{16} & K_{26} & K_{36} & K_{46} & K_{56} & K_{66} \end{bmatrix} \tag{6.18}$$

where

$K_{11} = k_r \cdot (t_{11}^2 + t_{21}^2 + t_{31}^2)$,

$K_{12} = k_r(t_{11} \cdot t_{12} + t_{21} \cdot t_{22} + t_{31} \cdot t_{32})$,

$K_{14} = k_r(t_{11} \cdot t_{14} + t_{21} \cdot t_{24} + t_{31} \cdot t_{34})$,

$K_{15} = k_r(t_{11} \cdot t_{15} + t_{21} \cdot t_{25} + t_{31} \cdot t_{35})$,

$K_{16} = k_r(t_{11} \cdot t_{16} + t_{21} \cdot t_{26} + t_{31} \cdot t_{36})$,

$K_{22} = k_r \cdot (t_{12}^2 + t_{22}^2 + t_{32}^2)$,

$K_{24} = k_r(t_{12} \cdot t_{14} + t_{22} \cdot t_{24} + t_{32} \cdot t_{34})$,

$K_{25} = k_r(t_{12} \cdot t_{15} + t_{22} \cdot t_{25} + t_{32} \cdot t_{35})$,

$K_{26} = k_r(t_{12} \cdot t_{16} + t_{22} \cdot t_{26} + t_{32} \cdot t_{36})$,

$K_{33} = 3 \cdot k_l$,

$$K_{34} = k_l \cdot (t_{44} + t_{54} + t_{64}),$$

$$K_{35} = k_l \cdot (t_{45} + t_{55} + t_{65}),$$

$$K_{44} = k_r \cdot (t_{14}^2 + t_{24}^2 + t_{34}^2) + k_l \cdot (t_{44}^2 + t_{54}^2 + t_{64}^2),$$

$$K_{45} = k_r \cdot (t_{14} \cdot t_{15} + t_{24} \cdot t_{25} + t_{34} \cdot t_{35}) + k_l \cdot (t_{44} \cdot t_{45} + t_{54} \cdot t_{55} + t_{64} \cdot t_{65}),$$

$$K_{46} = k_r \cdot (t_{14} \cdot t_{16} + t_{24} \cdot t_{26} + t_{34} \cdot t_{36}),$$

$$K_{55} = k_r \cdot (t_{15}^2 + t_{25}^2 + t_{35}^2) + k_l \cdot (t_{45}^2 + t_{55}^2 + t_{65}^2),$$

$$K_{56} = k_r \cdot (t_{15} \cdot t_{16} + t_{25} \cdot t_{26} + t_{35} \cdot t_{36}),$$

$$K_{66} = k_r \cdot (t_{16}^2 + t_{26}^2 + t_{36}^2).$$

In the stiffness matrix K, the upper left 3×3 sub-matrix is the translational matrix of the PM, the lower right 3×3 sub-matrix represent the torsional stiffness of the PM, and the other two 3×3 sub-matrices are the cross coupling effects between forces and moments. Note that the translational stiffness along x- and y- axes, and the torsional stiffness about z-axis, are only related to the stiffness of rotary actuators. The translational stiffness along the z-direction, K_{33}, is a constant, which is three times of the stiffness of the linear actuators. This is obvious because the forces along the z-direction is completely supported by the three linear actuators. This property makes the PM suitable for supporting large vertical load.

With the optimal parameters obtained in Section 5.5.3, and $k_r = 1000Nm$ and $k_l = 1000N/m$, the stiffness contours of the condition index of the 3RPPS PM are shown in Fig. 6.6 and Fig. 6.7. In these figures, the PM are in the position workspace under two orientations R_1 and R_2 respectively as follows.

$$R_1 = \begin{bmatrix} 1 & 0 & 0 \\ 0 & 1 & 0 \\ 0 & 0 & 1 \end{bmatrix}, \quad R_2 = \begin{bmatrix} 0.9881 & 0.1059 & 0.1118 \\ -0.1240 & 0.9776 & 0.1700 \\ -0.0913 & -0.1819 & 0.9791 \end{bmatrix}$$

Fig. 6.6 and Fig. 6.7 indicate that the central zones have the most uniform stiffness behavior. However the condition index of the stiffness matrix in these zones is very small, which means the stiffness is direction-dependent. Therefore, for certain tasks, it is better to operate in the direction with high stiffness. To further study the stiffness of the 3RPPS

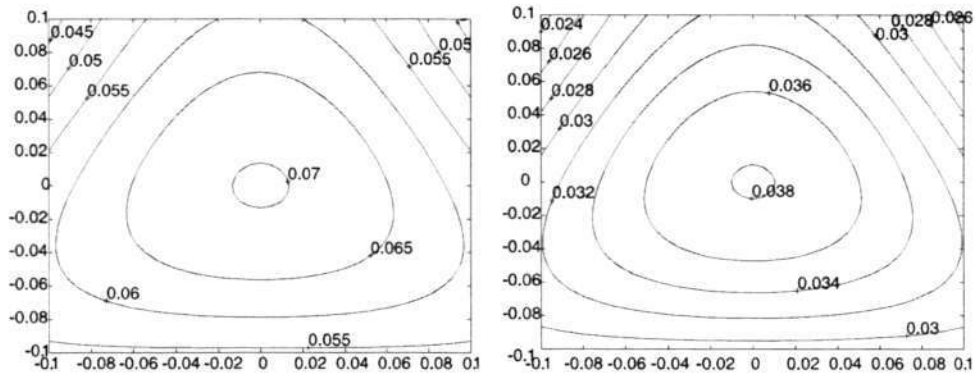

(a) $z = 0.2$ (b) $z = 0.4$

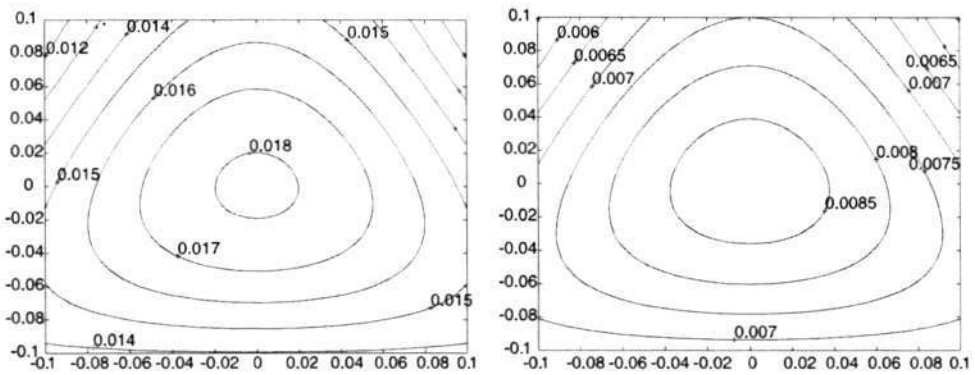

(c) $z = 0.6$ (d) $z = 0.8$

Figure 6.6: Stiffness contours 3RPPS PM in translation workspace (R_1)

PM, the stiffness mappings under two orientations (R_1 and R_2) are shown in Fig. 6.8 and Fig. 6.9. From Fig. 6.8 and Fig. 6.9, we can see that the translational stiffness along the x-axis, and the torsional stiffness about y-axis, will increase when y value decreases. The translational stiffness along the y-axis, and the torsional stiffness about the x-axis, will increase when y value increases. The central region has the lowest torsional stiffness about the z-axis. Fig. 6.10 shows the stiffness mapping in the orientational workspace. Note that the end-effector orientations are represented by three Z-Y-Z Euler angles, i.e., α, β and γ. We can clearly see that the home position of the manipulator (i.e., $\alpha = \beta = \gamma = 0$) have the best stiffness property in every directions from Fig. 6.10.

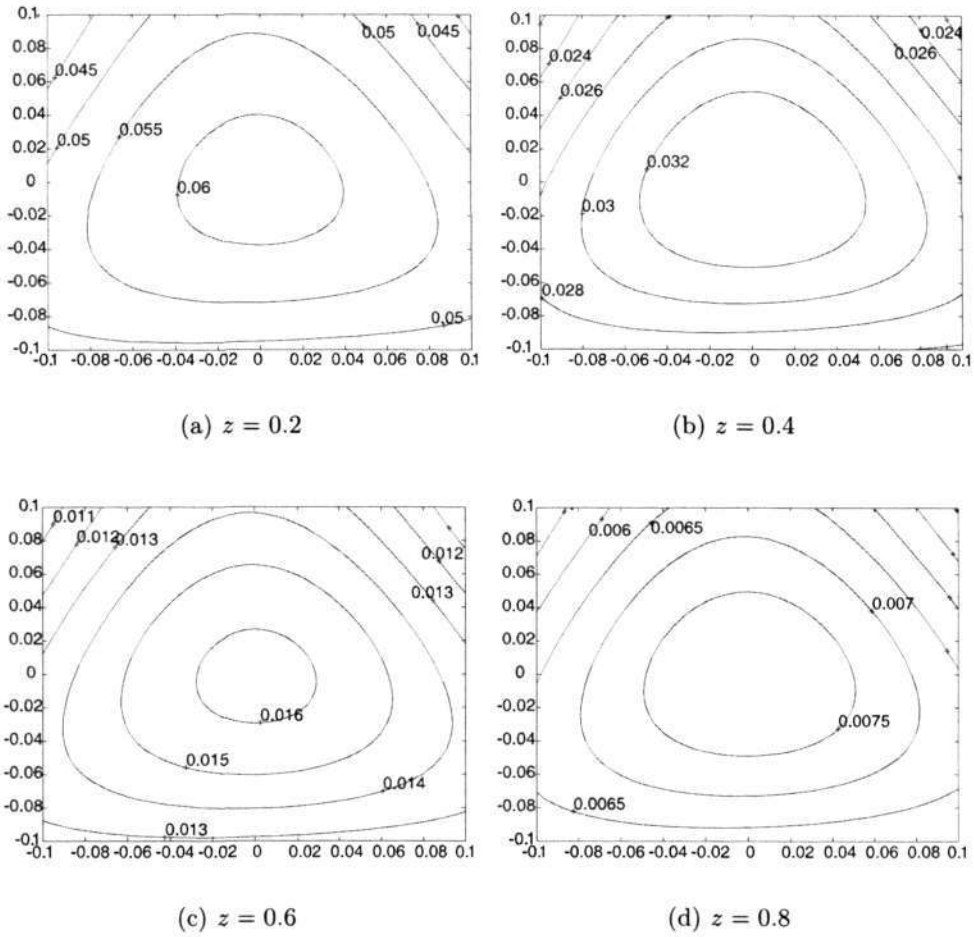

(a) $z = 0.2$ (b) $z = 0.4$

(c) $z = 0.6$ (d) $z = 0.8$

Figure 6.7: Stiffness contours 3RPPS PM in translation workspace (R_2)

6.4 Summary

In this chapter, both static characteristics and stiffness properties of two types of decoupled PMs are studied. It was shown that the end-effector force/moment can also be decoupled to a certain extent due to the decoupling motion structure. This will reduce the complexity and computation time for calculating the forces/moments and stiffness of the manipulator. The maximal generalized force at the GIP are obtained. The stiffness mapping for both the SA-PM and the 3RPPS PM are formulated. As a result, the torsional and translational stiffness of the SA-PM can be decoupled because the translation and rotation of the end-effector are independently controlled. The torsional and translational

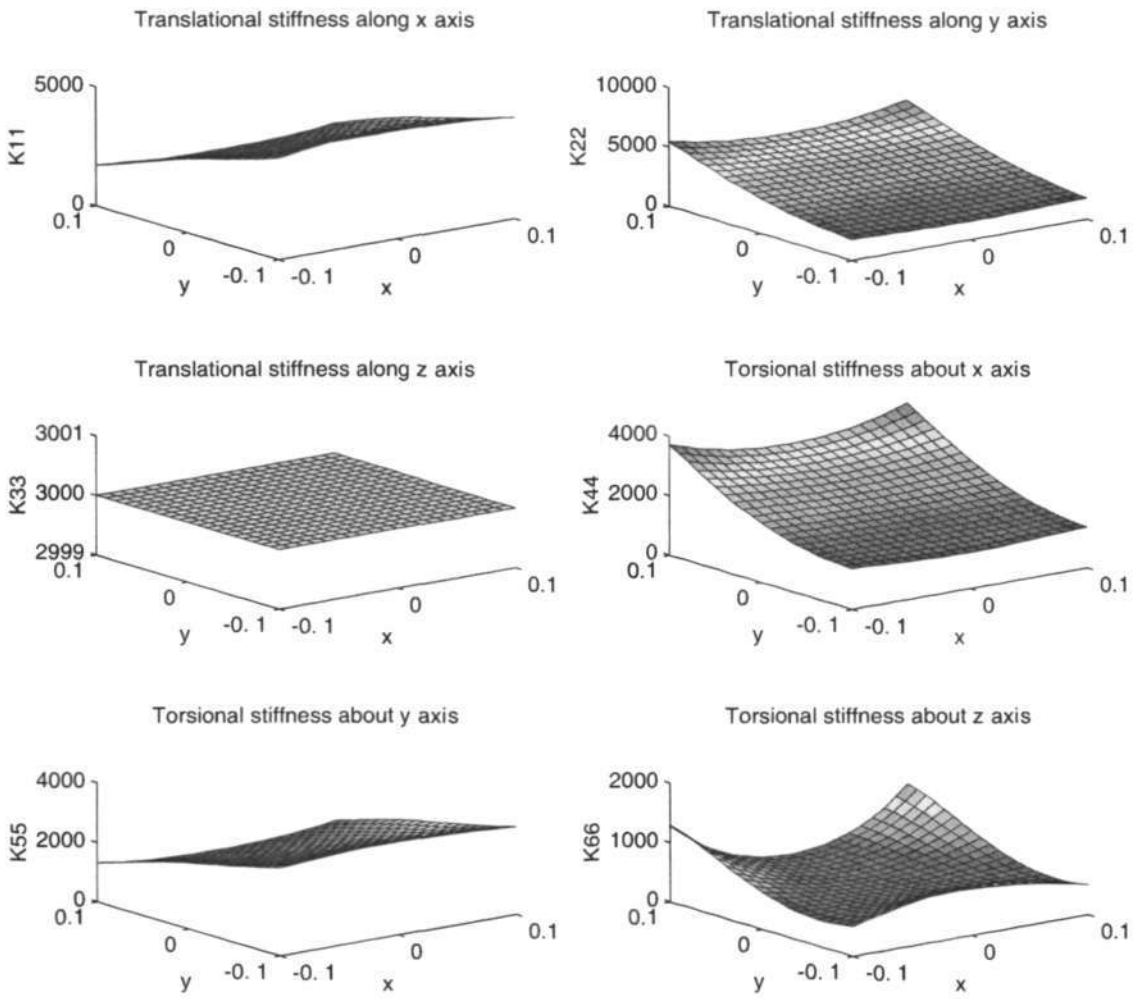

Figure 6.8: Stiffness mappings of the 3RPPS PM (R_1, z=0.4)

stiffnesses cannot be decoupled because the two moments (n_1 and n_2) will be contributed by all actuators. The stiffness contours based on the condition index of stiffness matrix are obtained for both the SA-PM and the 3RPPS PM, which reveal the regions with the best uniform stiffness properties in the workspace.

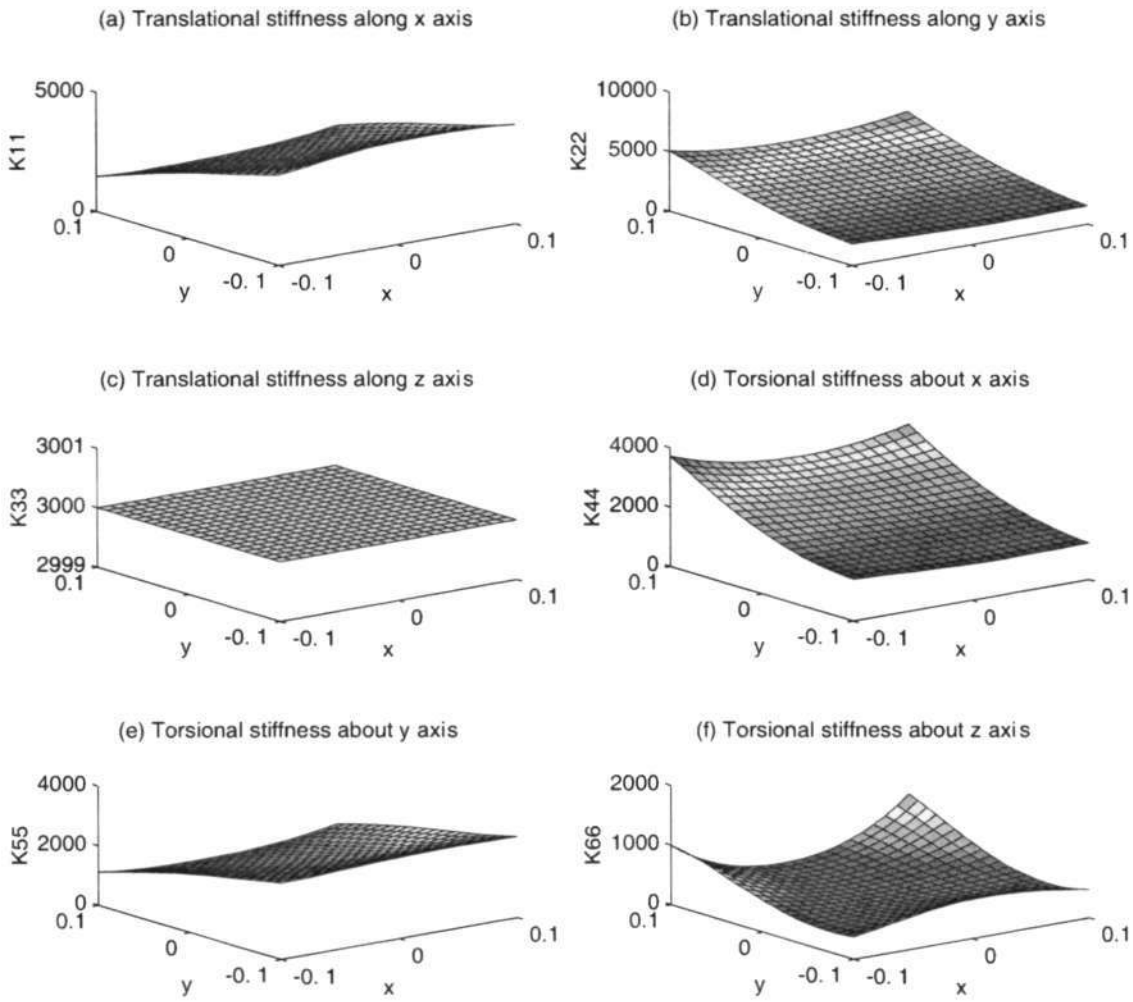

Figure 6.9: Stiffness mappings of the 3RPPS PM (R_2, z=0.4)

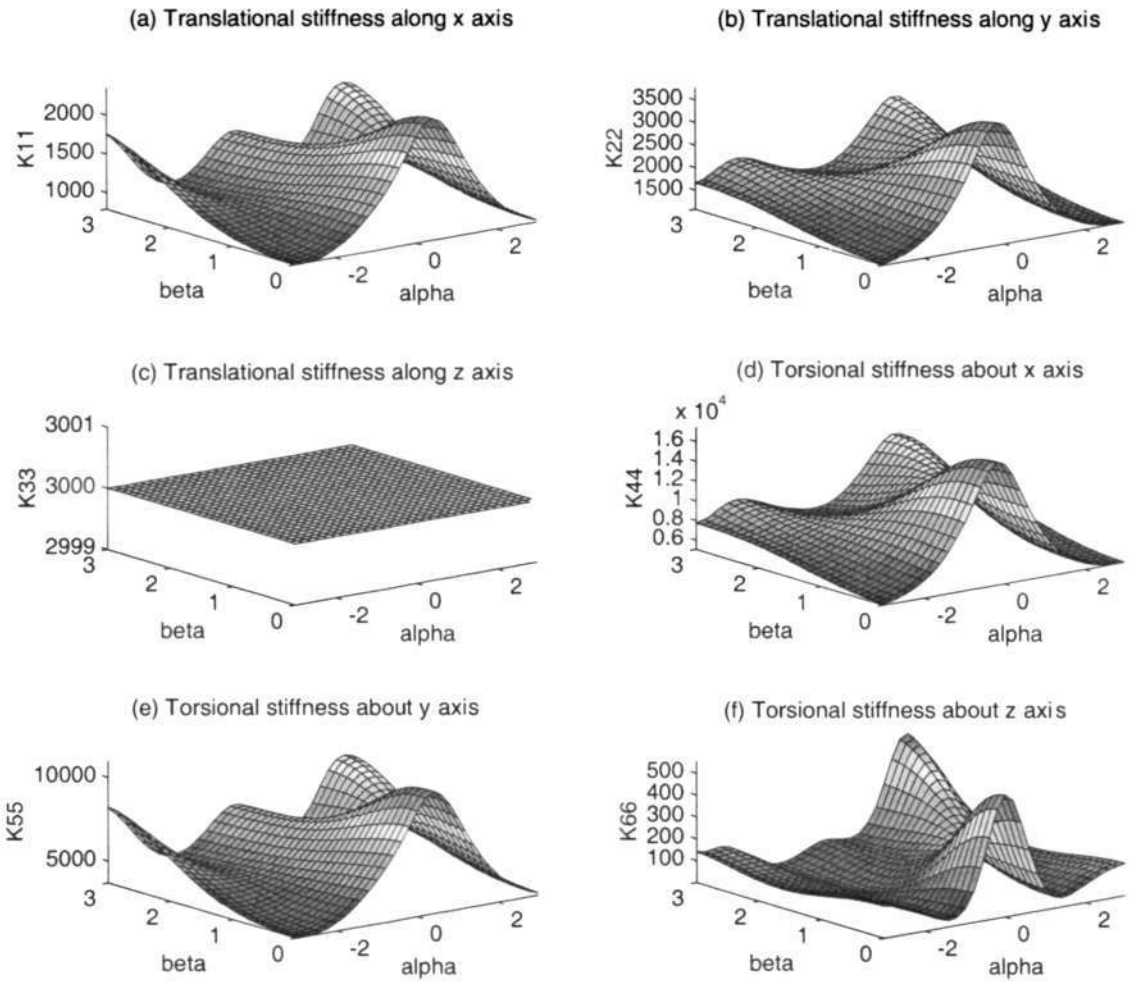

Figure 6.10: Stiffness mappings of the 3RPPS PM with constant position, (p=(-0.05,0.05,1.07), $\gamma = 0$)

Chapter 7

Study on Constraint Errors

From perspective of structure synthesis, some special geometric constraints are unavoidable in order to realize the decoupled end-effector motion of kinematically decoupled parallel manipulators (PMs), such as joint axes intersecting at one point or perpendicular to each other. These constraints are difficult to achieve in the actual system due to the assembly errors and manufacturing tolerances. These errors caused by the violation of the geometric constraint requirements are termed "constraint errors". The constraint errors are usually more harmful than conventional errors because the decoupling characteristics of the manipulator may no longer exist and the kinematic models will be rendered useless due to these constraint errors. Therefore, identification and prevention of these constraint errors in the initial design stage are of great significance.

This chapter is organized as follows. Section 7.2 introduces three basic types of geometric errors from commonly seen joint arrangements of decoupled PMs. A general procedure to evaluate the constraint errors on decoupling characteristics of PMs is proposed in Section 7.3. This approach is illustrated by the SA-PM in Section 7.4.

7.1 Introduction

PMs featuring decoupled motion usually need to satisfy certain critical geometrical constraints, for example, the axes of revolute (R) joints intersecting at one common point and the moving direction of the passive prismatic (P) joint being perpendicular to the related actuator axis [55], the axis of the rotary actuator aligning with the moving direction of the prismatic actuator in each limb, and the axes of passive R-joint and rotary actuator being parallel [113], the three passive R-joints being in one plane and each of them perpendicular to the related hydraulic actuator [5]. When manufacturing tolerances and assembly errors are considered, the actual manipulator motion may not be decoupled as stated in the design. Although these manufacturing errors may be compensated through the kinematic calibration [86, 107, 111, 116], it is still not possible to know the effects of the errors on the manipulator kinematics. Hence, it is difficult for engineers to identify the source of the geometrical errors and minimize them in the initial manufacturing stage. For PMs with less than six DOFs, kinematic errors may not even be recovered through calibration. Parenti-Castelli and Di Gregorio studied the error effects on the kinematic performance of PMs with three DOFs [35, 90], and found that some errors satisfying the DOF requirements of the end-effector can be calibrated while other errors cannot be calibrated. The effects of these errors should be analyzed in the initial design stage as a preventive measure and guideline for the manufacturing of the PM.

7.2 Basic Types of Constraint Errors

In topological design of decoupled PMs, certain geometric constraints on the layout of the joints are usually required. When these geometric requirements cannot be met, the end-effector of the PM will not have the desired decoupled motion. Three types of geometric requirements on the joint arrangement can be commonly seen: two adjacent revolute (R) joints are either intersecting (Fig. 7.1) or in parallel (Fig. 7.2), or an R-joint and a

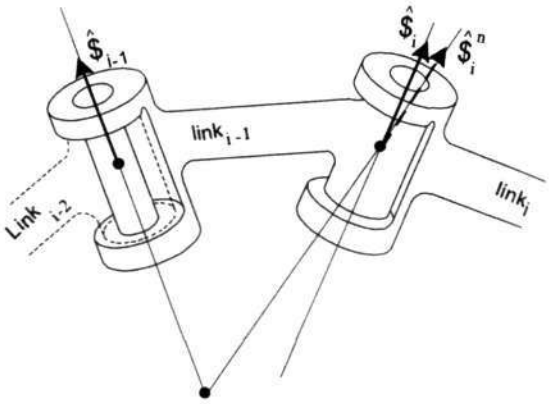

Figure 7.1: Nominally intersecting

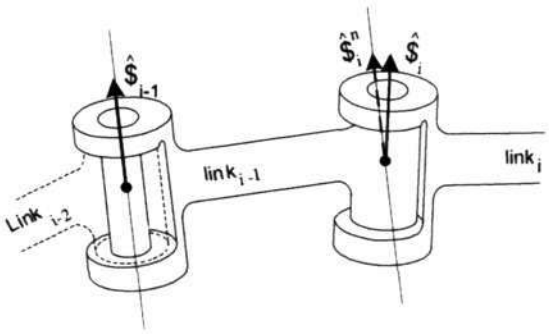

Figure 7.2: Nominally parallel

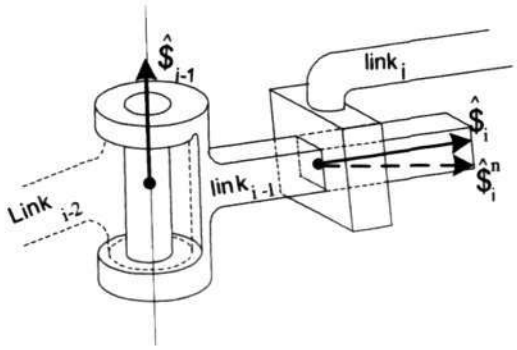

Figure 7.3: Nominally perpendicular

prismatic (P) joint are mutually perpendicular (Fig. 7.3). It is difficult to meet these geometric constraints exactly due to the manufacturing tolerances and assembly errors. Therefore, the motion of the end-effector due to these errors needs to be studied. The possible geometric constraint errors of the joint axes that violate the basic geometric requirements are shown respectively as Figures 7.1, 7.2 and 7.3, in which $\hat{\$}_i^n$ and $\hat{\$}_i$ represent the nominal and actual poses of the i^{th} joint axis respectively. Figure 7.1 shows that two nominally intersecting R-joint axes may not be intersected at time. Figure 7.2 shows that two nominally parallel R-joints are not in parallel in the actual situation. Figure 7.3 shows that the P-joint and the R-joint are not mutually perpendicular. The geometry of a decoupled PM that violate the constraints are very often the combination of the three basic types of geometric errors.

7.3 Evaluation of Constraint Errors on End-effector Motion

A systematic procedure is proposed here to determine how the constraint errors affect the motion of a PM with decoupled kinematic structure. This procedure consists of four steps as shown in Fig. 7.4:

- **Step 1 (Error Identification)**: This is to determine types of errors violating the stringent geometric constraints, which will be the combination of the three basic types of errors. For example, three nominally intersecting R-joint axes can be regarded as one type of errors in a PM.

- **Step 2 (Error Jacobian Analysis)**: This is to determine how the end-effector motion can be affected by different types of errors obtained in Step 1. In this way, we can find which type of errors will carry more weight to the end-effector motion. Depending on the manipulator structure, the characteristic length may be found as a measure of average errors of the end-effector.

- **Step 3 (Motion Evaluation)**: First, a geometric error model is required to be developed for assigning the constant errors. A general forward kinematic model is required in simulation for calculating the actual poses of the end-effector, in which the Jacobian model under constraint errors obtained in Step 2 will be used. Then the motion error of the end-effector can be calculated by comparing with the nominal pose. Several trajectories away from singularities in the workspace are randomly chosen for evaluating the motion errors. The motion errors due to each type of constraint errors can be obtained subsequently.

- **Step 4 (Comparison of Errors)**: Based on the results obtained in Step 3, the motion errors of the end-effector due to different types of constraint errors are compared, and the influences of each type of errors are obtained.

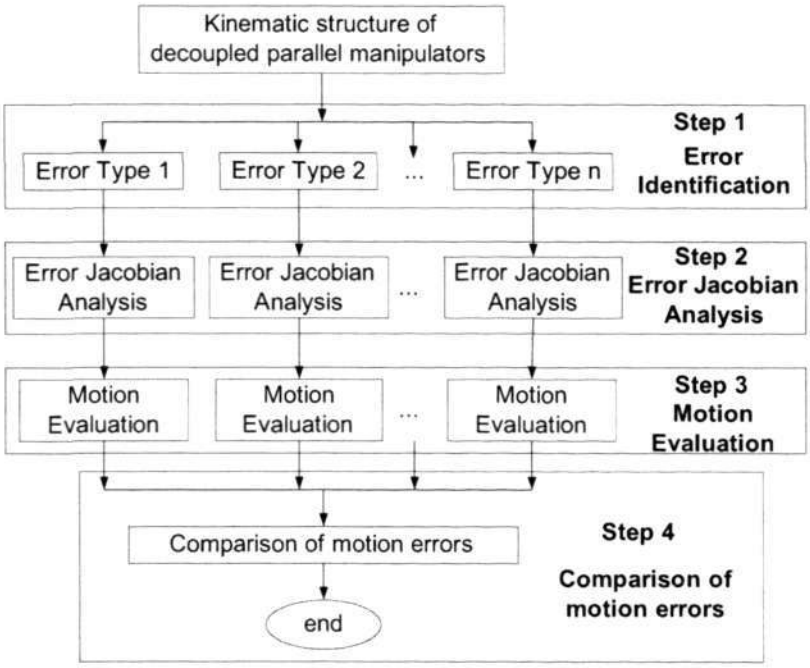

Figure 7.4: General procedure for decoupled motion evaluation

7.4 An Example: Selectively Actuated Parallel Manipulator

The SA-PM is taken as an example to illustrate the approach in this section. As shown in Section 3.2.1, the SA-PM is required to satisfy two geometry constraints: 1) the two passive P-joint axes are perpendicular to the actuator axis in each limb; 2) the six passive R-joints must intersect at one common point O'.

7.4.1 Identification of Error

When the manufacturing and assembly errors are considered, three kinds of constraint errors violating the geometrical requirements of the PM can be identified. If these errors occur, the decoupling characteristics of the PM may not exist. The three types of errors are stated as follows.

- Error Type I: The two passive R-joint axes of each limb are intersecting at one

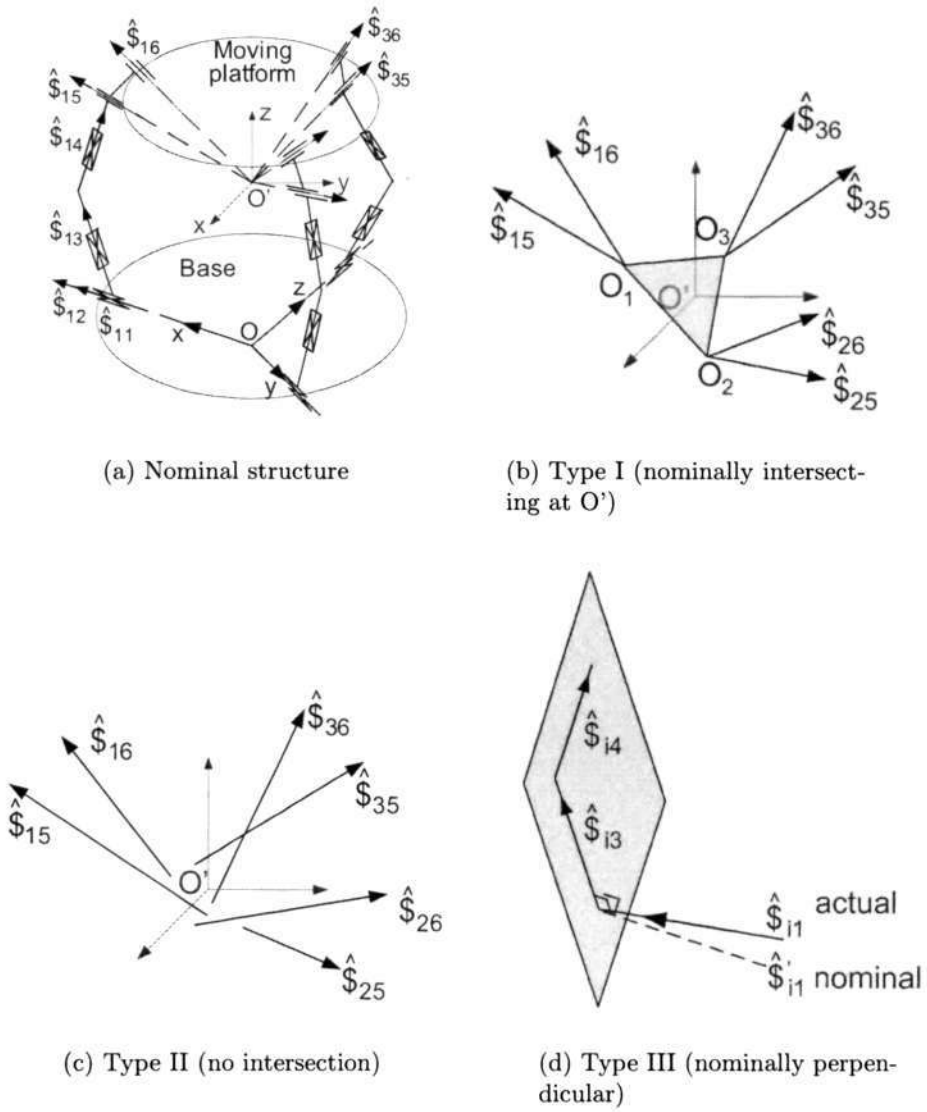

(a) Nominal structure

(b) Type I (nominally intersecting at O')

(c) Type II (no intersection)

(d) Type III (nominally perpendicular)

Figure 7.5: Nominal structure and three types of constraint errors SA-PM

point, but the three intersecting points for three limbs are not coincident as shown in Fig. 7.5(b). In this way, the three force wrench associated with each limb will not intersect at one common point, and there is no pure orientation for the end-effector.

- Error Type II: The two passive R-joint axes are not intersecting at one point as shown in Fig. 7.5(c). In this case, there will be no force wrench to constraint the end-effector [55], and there is no pure orientation for the end-effector.

- Error Type III: The plane determined by the two passive P-joint axes of each limb is

not perpendicular to the related actuator axis as shown in Fig. 7.5(d). In this case, there will be no force wrench imposed on the end-effector, and the pure orientation for the end-effector cannot be obtained.

7.4.2 Error Jacobian Analysis for Kinematic Decoupling Characteristics

Referring to the nominal Jacobian of the SA-PM eqn. (3.8), the Jacobian matrices with errors can be studied using the following method. Under the three types of errors, the manipulator still has six DOFs as computed using Grübler-Kutzbach criterion.

Error Type I: As shown in Fig. 7.5(b), the three intersecting points O_1, O_2 and O_3 may not coincide at a common point O', i.e., $O'O_1, O'O_2$ and $O'O_3$ are three alignment errors. This kind of errors may occur in the manufacturing or assembly process. In this case, the three force constraints of the joints will not intersect at one common point. The end-effector will have complex three DOFs when all three actuators act in the rotary mode. As there are four passive joints in each limb forming a 4-system, two reciprocal screws (or wrenches) for each limb are needed for formulating Jacobian matrix of the PM [102]. Under alignment errors mentioned above, a screw that is reciprocal to all the passive joint screws is

$$\$_{ir1} = \begin{bmatrix} 0 \\ \boldsymbol{s}_{5,i} \times \boldsymbol{s}_{6,i} \end{bmatrix} \qquad i=1,2,3. \tag{7.1}$$

and the other reciprocal screw is:

$$\$_{ir2} = \begin{bmatrix} \boldsymbol{s}_{i1} \\ \boldsymbol{O'O_i} \times \boldsymbol{s}_{i1} \end{bmatrix} \qquad i=1,2,3. \tag{7.2}$$

Taking the orthogonal product of both sides of instantaneous kinematics eqn. (3.4) with $\$_{ir1}$ and $\$_{ir2}$, we have

$$J_x \dot{\mathbf{x}} = J_\theta \dot{\boldsymbol{\theta}}, \tag{7.3}$$

where $J_x = \begin{bmatrix} A & 0 \\ B & C \end{bmatrix}$, $J_\theta = \begin{bmatrix} D & 0 \\ 0 & I \end{bmatrix}$,

$A = [\, \boldsymbol{s}_{15} \times \boldsymbol{s}_{16} \quad \boldsymbol{s}_{25} \times \boldsymbol{s}_{26} \quad \boldsymbol{s}_{35} \times \boldsymbol{s}_{36} \,]^T$,

$B = [\boldsymbol{O'O}_1 \times \boldsymbol{s}_{11} \quad \boldsymbol{O'O}_2 \times \boldsymbol{s}_{21} \quad \boldsymbol{O'O}_3 \times \boldsymbol{s}_{31}]^T$,

$C = [\boldsymbol{s}_{11} \quad \boldsymbol{s}_{21} \quad \boldsymbol{s}_{31}]^T$,

$D = diag[(\boldsymbol{s}_{15} \times \boldsymbol{s}_{16}) \cdot \boldsymbol{s}_{11}, (\boldsymbol{s}_{25} \times \boldsymbol{s}_{26}) \cdot \boldsymbol{s}_{21}, (\boldsymbol{s}_{35} \times \boldsymbol{s}_{36}) \cdot \boldsymbol{s}_{31}]$,

$\dot{\mathbf{x}} = [\boldsymbol{w}, \boldsymbol{v}]$, $\dot{\boldsymbol{\theta}} = \left[\dot{\theta}_{11}, \dot{\theta}_{21}, \dot{\theta}_{31}; \dot{\theta}_{12}, \dot{\theta}_{22}, \dot{\theta}_{32}\right]$. A, B, C, D are all 3×3 sub-matrices, and I is a 3×3 identity matrix.

Expanding eqn. (7.3), we have

$$\begin{cases} A\boldsymbol{w} = D\dot{\boldsymbol{\theta}}_1 \\ B\boldsymbol{w} + C\boldsymbol{v} = \dot{\boldsymbol{\theta}}_2 \end{cases}. \tag{7.4}$$

The major difference between eqn. (7.4) and the nominal equation (3.8) is the existence of the error matrix B. It shows that the translation is coupled with the orientation of the PM. The rotary velocity of the end-effector $\boldsymbol{w}$ may contribute to the linear velocity of the end-effector $\boldsymbol{v}$.

Error Type II: Under this type of errors, the end-effector still has 3-DOF spatial translations when all three actuators run in the linear mode. However, the end-effector will have hybrid 3-DOF motion, not pure orientation when all three actuators run in the rotary mode. In order to formulate Jacobian matrix of the manipulator under these errors, two reciprocal screws associated with the four passive joints are required for each limb. Let the reciprocal screw be in the following form,

$$\$_{ir} = \begin{bmatrix} \boldsymbol{s}_{ir} \\ \boldsymbol{h}_i \end{bmatrix} = \begin{bmatrix} a \\ b \\ c \\ d \\ e \\ f \end{bmatrix}, \qquad i=1,2,3, \tag{7.5}$$

where $\boldsymbol{s}_{ir}$ and $\boldsymbol{h}_i$ represent vectors of the first three elements and the last three elements respectively. We have

$$\boldsymbol{s}_{i3} \cdot \boldsymbol{s}_{ir} = 0 \qquad i=1,2,3. \tag{7.6}$$

$$\boldsymbol{s}_{i4} \cdot \boldsymbol{s}_{ir} = 0 \qquad i=1,2,3. \tag{7.7}$$

$$(\boldsymbol{O'A}_{i5} \times \boldsymbol{s}_{i5}) \cdot \boldsymbol{s}_{ir} + \boldsymbol{s}_{i5} \cdot \boldsymbol{h}_i = 0 \qquad i=1,2,3. \tag{7.8}$$

$$(\boldsymbol{O'A}_{i6} \times \boldsymbol{s}_{i6}) \cdot \boldsymbol{s}_{ir} + \boldsymbol{s}_{i6} \cdot \boldsymbol{h}_i = 0 \qquad i=1,2,3. \tag{7.9}$$

Based on eqn. (7.6) and eqn. (7.7), $\boldsymbol{s}_{ir}$ can be directly computed as follows

$$\boldsymbol{s}_{ir1} = \boldsymbol{0} \quad \text{or} \quad \boldsymbol{s}_{ir2} = \boldsymbol{s}_{i3} \times \boldsymbol{s}_{i4}, \qquad i=1,2,3. \tag{7.10}$$

Substituting $\boldsymbol{s}_{ir1}$ into eqn. (7.8) and eqn. (7.9), we have

$$\boldsymbol{h}_{i1} = \boldsymbol{s}_{i5} \times \boldsymbol{s}_{i6}, \qquad i=1,2,3. \tag{7.11}$$

Similarly, substituting $\boldsymbol{s}_{ir2}$ into eqn. (7.8) and eqn. (7.9) and denoting $\boldsymbol{s}_{i5} = [s_{i51}\ s_{i52}\ s_{i53}]^T$ and $\boldsymbol{s}_{i6} = [s_{i61}\ s_{i62}\ s_{i63}]^T$, we have

$$\boldsymbol{h}_{i2} = [\,d_i \quad e_i \quad f_i\,]^T, \qquad i=1,2,3. \tag{7.12}$$

where

d_i is an arbitrary scalar,

$e_i = (\rho_i \cdot t_{i6} - t_{i5} + d_i(\rho_i \cdot s_{i61} - s_{i51}))/(s_{i52} - \rho_i \cdot s_{i62})$,

$\rho_i = s_{i53}/s_{i63}$,

$f_i = (-t_6 - s_{i61} \cdot d_i - s_{i62} \cdot e_i)/s_{i63}$,

$t_{i5} = (\boldsymbol{O'A}_{i5} \times \boldsymbol{s}_{i5}) \cdot \boldsymbol{s}_{i1}$,

$t_{i6} = (\boldsymbol{O'A}_{i6} \times \boldsymbol{s}_{i6}) \cdot \boldsymbol{s}_{i1}$,

$\boldsymbol{s}_{i1} = \boldsymbol{s}_{i3} \times \boldsymbol{s}_{i4}$, $i=1,2,3$.

Without loss of generality, let $d_i = 0$, $\boldsymbol{h}_{i2}$ can be easily calculated and the second reciprocal screw is obtained. Taking the orthogonal product of both sides of instantaneous kinematics eqn. (3.4) with $\$_{ir1}$ and $\$_{ir2}$, we have

$$J_x \dot{\mathbf{x}} = J_\theta \dot{\boldsymbol{\theta}}, \tag{7.13}$$

where $J_x = \begin{bmatrix} A & 0 \\ B & C \end{bmatrix}$, $J_\theta = \begin{bmatrix} D & 0 \\ E & I \end{bmatrix}$,

$A = [\,\boldsymbol{s}_{15} \times \boldsymbol{s}_{16} \quad \boldsymbol{s}_{25} \times \boldsymbol{s}_{26} \quad \boldsymbol{s}_{35} \times \boldsymbol{s}_{36}\,]^T$,

$B = [\,\boldsymbol{h}_{12} \quad \boldsymbol{h}_{22} \quad \boldsymbol{h}_{32}\,]^T$,

$C = [\,\boldsymbol{s}_{11} \quad \boldsymbol{s}_{21} \quad \boldsymbol{s}_{31}\,]^T$,

$D = diag\,[(\boldsymbol{s}_{15} \times \boldsymbol{s}_{16}) \cdot \boldsymbol{s}_{11}, (\boldsymbol{s}_{25} \times \boldsymbol{s}_{26}) \cdot \boldsymbol{s}_{21}, (\boldsymbol{s}_{35} \times \boldsymbol{s}_{36}) \cdot \boldsymbol{s}_{31}]$,

$E = diag\,[e_1, e_2, e_3]$,

$e_i = \boldsymbol{s}_{i1} \cdot \boldsymbol{h}_{i2}$, $(i$=1,2,3),

$\dot{\mathbf{x}} = [\boldsymbol{w}, \boldsymbol{v}]$, $\dot{\boldsymbol{\theta}} = \left[\dot{\theta}_{11}, \dot{\theta}_{21}, \dot{\theta}_{31}; \dot{\theta}_{12}, \dot{\theta}_{22}, \dot{\theta}_{32}\right]$.

Expanding eqn. (7.13), we have

$$\begin{cases} A\boldsymbol{w} = D\dot{\boldsymbol{\theta}}_1 \\ B\boldsymbol{w} + C\boldsymbol{v} = \dot{\boldsymbol{\theta}}_2 + E\dot{\boldsymbol{\theta}}_1 \end{cases}. \tag{7.14}$$

Equation (7.14) shows that the translation is coupled with the orientation of the PM. The linear velocity of the end-effector $\boldsymbol{v}$ will have contributions from the rotation of the actuators due to the error matrices B and E.

Error Type III: Type III errors occur when the plane determined by two passive P-joint axes is not normal to the actuator axis in each limb. Let $\boldsymbol{s}'_{i1}$ represents the ideal direction of the actuator axis and $\boldsymbol{s}_{i1}$ represents the actual direction with errors. According to screw theory [102], the first reciprocal screw will be the same for each limb as in Section 7.4.2. The second one is

$$\hat{\$}_{ir2} = \begin{bmatrix} \boldsymbol{s}'_{i1} \\ \mathbf{0} \end{bmatrix} \qquad i$=1,2,3. \tag{7.15}$$

where $\boldsymbol{s}'_{i1}$ is normal to the plane determined by two vectors $\boldsymbol{s}_{i3}$ and $\boldsymbol{s}_{i4}$.

Taking the orthogonal product of both sides of instantaneous kinematics eqn. (3.4) with the two reciprocal screw for each limb, we have

$$J_x\dot{\mathbf{x}} = J_\theta\dot{\boldsymbol{\theta}}, \tag{7.16}$$

where $J_x = \begin{bmatrix} A & 0 \\ 0 & C \end{bmatrix}$, $J_\theta = \begin{bmatrix} D & 0 \\ E & F \end{bmatrix}$,

$A = [\,\boldsymbol{s}_{15} \times \boldsymbol{s}_{16} \quad \boldsymbol{s}_{25} \times \boldsymbol{s}_{26} \quad \boldsymbol{s}_{35} \times \boldsymbol{s}_{36}\,]^T$,

$C = [\,\boldsymbol{s}'_{11} \quad \boldsymbol{s}'_{21} \quad \boldsymbol{s}'_{31}\,]^T$,

$D = diag\,[(\boldsymbol{s}_{15} \times \boldsymbol{s}_{16}) \cdot \boldsymbol{s}_{11}, (\boldsymbol{s}_{25} \times \boldsymbol{s}_{26}) \cdot \boldsymbol{s}_{21}, (\boldsymbol{s}_{35} \times \boldsymbol{s}_{36}) \cdot \boldsymbol{s}_{31}]$,

$E = diag\,[(\boldsymbol{s}_{11} \times \boldsymbol{s}'_{11}) \cdot \boldsymbol{O'A}_{11}, (\boldsymbol{s}_{21} \times \boldsymbol{s}'_{21}) \cdot \boldsymbol{O'A}_{21}, (\boldsymbol{s}_{31} \times \boldsymbol{s}'_{31}) \cdot \boldsymbol{O'A}_{31}]$,

$F = diag\,[\,\boldsymbol{s}_{11} \cdot \boldsymbol{s}'_{11} \quad \boldsymbol{s}_{21} \cdot \boldsymbol{s}'_{21} \quad \boldsymbol{s}_{31} \cdot \boldsymbol{s}'_{31}\,]^T$,

$\dot{\mathbf{x}} = [\boldsymbol{w}, \boldsymbol{v}]$, $\dot{\boldsymbol{\theta}} = \left[\dot{\theta}_{11}, \dot{\theta}_{21}, \dot{\theta}_{31}; \dot{\theta}_{12}, \dot{\theta}_{22}, \dot{\theta}_{32}\right]$. A, C, D, E, F are all 3×3 sub-matrices.

Expanding eqn. (7.16), we have

$$\begin{cases} A\boldsymbol{w} = D\dot{\boldsymbol{\theta}}_1 \\ C\boldsymbol{v} = \dot{\boldsymbol{\theta}}_2 + E\dot{\boldsymbol{\theta}}_1 + (F-I)\dot{\boldsymbol{\theta}}_2 \end{cases}, \tag{7.17}$$

where I represents the 3×3 identity matrix. Equation (7.17) shows that the translation is not decoupled with the orientation of the PM. The linear velocity of the end-effector will have contribution from the rotation of the actuators multiplied by the error matrix E and an error from the linear velocities of actuators multiplied by the error matrix $(F-I)$. Specially, the errors in $(\boldsymbol{s}_{i1} \times \boldsymbol{s}'_{i1})$ can be magnified proportionally by $\|\boldsymbol{O'A}_{i1}\|$, which can have large values. For each non-zero element in the matrix E, we have

$$(\boldsymbol{s}_{i1} \times \boldsymbol{s}'_{i1}) \cdot \boldsymbol{O'A}_{i1} = (\boldsymbol{s}'_{i1} \times \boldsymbol{O'A}_{i1}) \cdot \boldsymbol{s}_{i1} \doteq (\boldsymbol{s}'_{i1} \times \boldsymbol{O'O}) \cdot \boldsymbol{s}_{i1} = (\boldsymbol{s}_{i1} \times \boldsymbol{s}'_{i1}) \cdot \boldsymbol{O'O} \tag{7.18}$$

When $O'O$ is very large, the contribution to the motion error from matrix E will be far more than that from the matrix $(F-I)$. In order to quantify the linear error, the term, *Characteristic Length* (CL) of the parallel manipulator is introduced as an evaluation criteria. CL is defined as the distance from the origin of the base frame to the origin of the end-effector frame

$$l = \|\boldsymbol{OO}'\|, \tag{7.19}$$

which is a measure of the average positional error of the end-effector. Note that the CL here is different from the CL defined in [7] which is used to resolve the dimensional inhomogeneity in computing the condition number of a Jacobian matrix.

7.4.3 Error on End-effector Motion

Geometric Description of Link Errors

As shown in Fig. 7.6, due to geometry errors, the actual frame i^a will be different from the nominal frame i of link i. Let $T_{i-1,i}(0)$ and $T^a_{i-1,i}(0)$ be the initial pose of the nominal link frame i and the actual link frame i^a with respect to the frame $i-1$. Based on differential transformation theory [86, 93], the geometrical errors can be represented

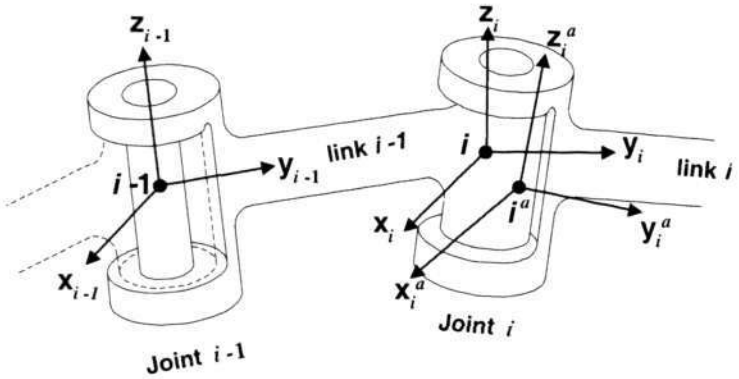

Figure 7.6: Coordinate frames in a dyad

by an infinitesimal translation $\mathbf{Trans}(\delta x_i, \delta y_i, \delta z_i)$, followed by an infinitesimal rotation $\mathbf{Rot}(\delta\alpha_i, \delta\beta_i, \delta\gamma_i)$, where $\delta x_i, \delta y_i, \delta z_i$ are infinitesimal displacements along x, y, z axis of frame i and $\delta\alpha_i$, $\delta\beta_i$, $\delta\gamma_i$ are infinitesimal rotations about the x, y, z axes of frame i respectively. Then we have

$$T^a_{i-1,i}(0) = (I + \delta\hat{t}_i)T_{i-1,i}(0), \tag{7.20}$$

where

$$\delta\hat{t}_i = \begin{bmatrix} 0 & -\delta\gamma_i & \delta\beta_i & \delta x_i \\ \delta\gamma_i & 0 & -\delta\alpha_i & \delta y_i \\ -\delta\beta_i & \delta\alpha_i & 0 & \delta z_i \\ 0 & 0 & 0 & 0 \end{bmatrix}. \tag{7.21}$$

As shown in Section 5.2, $\delta\hat{t}_i$ ($\in se(3)$ can be represented by a twist $\delta t_i = (\delta\alpha_i, \delta\beta_i, \delta\gamma_i, \delta x_i, \delta y_i, \delta z_i)^T$, which is used for describing the errors.

Actual Model of Forward Kinematics

In order to calculate the end-effector errors, an actual model of forward kinematics is required. Although the nominal forward kinematics has close-form solutions [53], the actual forward kinematics is very complicated because it is no longer a decoupled motion structure. Hence, a numerical approach is needed to compute the actual pose of the end-effector as shown in Fig. 7.7.

Given actuator displacements $\boldsymbol{\theta}^a_a$, by using the nominal kinematics model, all solutions

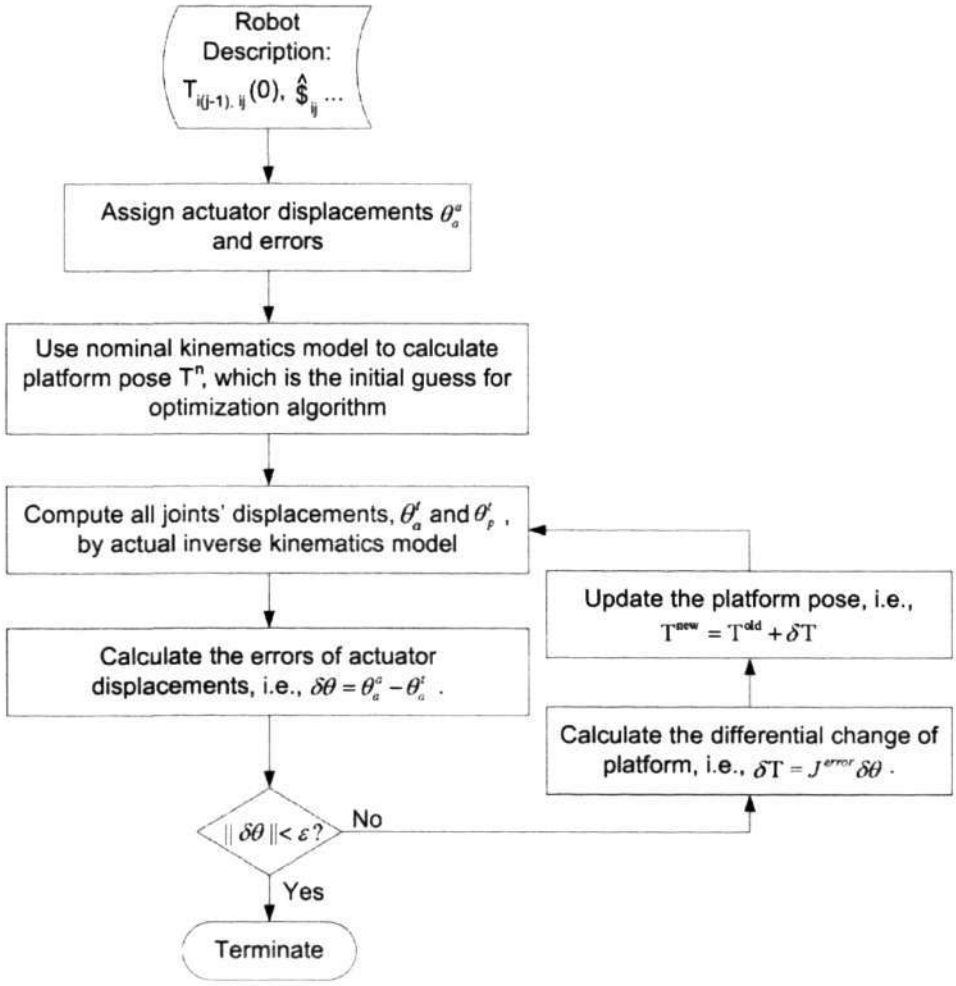

Figure 7.7: Actual model of forward kinematics

of the forward kinematics can be obtained [53], which is used for the initial guess of the actual pose of the end-effector in the iterative-loop computation. Then, the displacements of all active and passive joints can be calculated using the actual inverse kinematics, which employs the same approach as the nominal inverse kinematics [53] except for those errors. After the calculated values of actuator displacements $\boldsymbol{\theta}_a^t$ are obtained, the difference between the actual actuator displacements and the calculated ones can be computed. The difference is compared with a given infinitesimal value ε to determine if the loop can be terminated. If the magnitude of the difference vector is larger than ε, the difference will be multiplied by the actual Jacobian matrix to calculate the current differential change of the end-effector. The resultant differential change will be used to modify the end-effector

pose to approach the actual pose of the end-effector. The computation loop will stop if the difference vector is smaller than ε. The actual pose, i.e., the last platform pose, is then obtained. Note that all the solutions of the actual forward kinematics can be obtained as we have close-form solutions in the nominal forward kinematics.

Numerical Evaluation

Generally, tight manufacturing tolerances will lead to high fabrication cost. To assign reasonable tolerances in manufacturing is a very important work in mechanical design. However, it is not an easy task to assign reasonable tolerances to links and joints because some geometrical parameters may be more critical on the performance than others. Here we use a numerical approach, implemented in Matlab, for evaluating the error effects on the end-effector of the PM. The evaluation procedure is as follows.

- **Step 1**: Six trajectories away from singularity in the workspace are selected as sample trajectories, and each sample point on the trajectory represents an ideal pose of the end-effector. The trajectories are random selected based on the decoupled motion characteristics of the PM.
- **Step 2**: All joints' displacements are calculated based on the nominal kinematics model.
- **Step 3**: The critical geometrical errors are assigned to the geometrical parameters.
- **Step 4**: The actual pose of the end-effector is calculated.
- **Step 5**: Both the ideal and actual pose of the end-effector are transformed into the form of 6×1 vectors, i.e., twists.
- **Step 6**: The error of the end-effector pose, which is the difference between the actual pose and the ideal pose, is calculated.

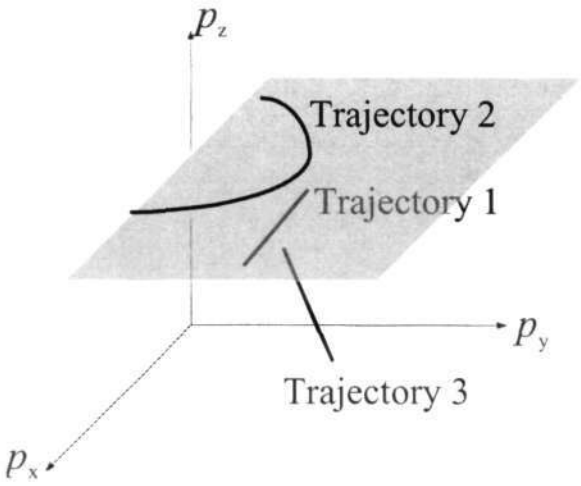

Figure 7.8: Trajectories in translational workspace

According to Error-Jacobian analysis, the orientation of the end-effector is only controlled by rotary displacements of the three actuators, and the position of the end-effector is only determined by three linear displacements of the actuators if rotary motion of the 2-DOF actuators is locked. Hence, the position errors and orientation errors can be evaluated separately. Note that the passive prismatic joint limits are not considered here. The geometrical dimensions of the SA-PM are shown in Table 7.1. Generally speaking, the entire workspace needs to evaluate to find the maximum error effects. However, this required lots of computation which is not practical. Therefore, many researchers used several sample trajectories in the workspace to see the error effects of the end-effector of PMs [35, 90]. To evaluate the position errors, three trajectories in translational workspace with a constant orientation $\boldsymbol{w} = [0\ 0\ 0]^T$ (home pose) are defined here as follows (see Fig. 7.8).

- **Trajectory 1**: $p_x = 45 + t, p_y = 45 + t, p_z = 45 + t; (t \in [0.0\ 10.0]$, step=1.0)
- **Trajectory 2**: $p_x = 45 + 10 * \cos(t), p_y = 45 + 10 * \sin(t), p_z = 60; (t \in [0.0\ 3.0]$, step=0.3)
- **Trajectory 3**: $p_x = 30 + t, p_y = 60 - t, p_z = 45 + 0.5 * t; (t \in [0.0\ 10.0]$, step=1.0).

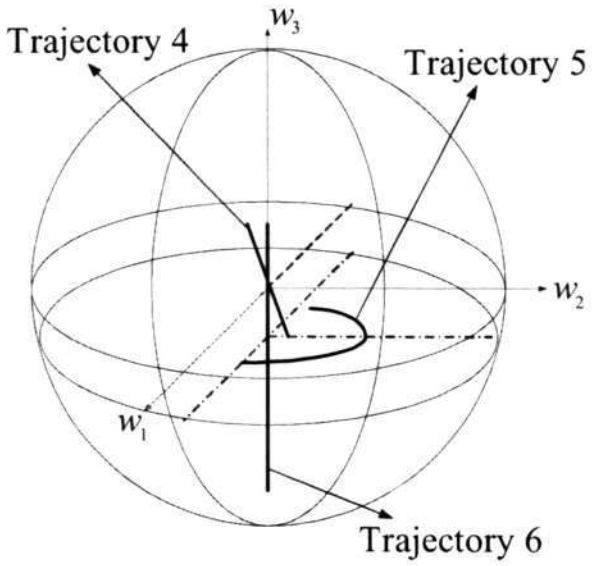

Figure 7.9: Trajectories in orientational workspace

Table 7.1: Geometric data of SA-PM

L_1	L_2	L_3	L_5	L_6	α	β_1	β_2	β_3	γ
30	30	30	30	30	$\pi/2$	0.0468	0.7261	3.8127	1.5519

To evaluate the orientation errors, three other trajectories in the orientational workspace with a constant position $\boldsymbol{p}_1 = [60\ 60\ 60]^T$ are defined as follows (see Fig. 7.9):

- **Trajectory 4**: $w_1 = 0.6 * t, w_2 = 0.8 * t, w_3 = 0.0; (t \in [-1.5\ 1.5]$, step=0.3)
- **Trajectory 5**: $w_1 = \cos(t), w_2 = \sin(t), w_3 = -0.1; (t \in [0.0\ 3.0]$, step=0.3)
- **Trajectory 6**: $w_1 = 0.0, w_2 = 0.0, w_3 = t; (t \in [-2.4\ 0.6]$, step=0.3).

The geometric errors are represented by twists assigned as follows,

- **Type I**: $\boldsymbol{\delta t}_{i67} = [0.0050 \quad 0.0050 \quad 0.0050 \quad 0.1000 \quad 0.1000 \quad 0.1000]^T, (i = 1, 2, 3);$
- **Type I.1**: $\boldsymbol{\delta t}_{167} = [0.0050 \quad 0.0050 \quad 0.0050 \quad 0.1000 \quad 0.1000 \quad 0.1000]^T$, (limb 1 only);
- **Type II**: $\boldsymbol{\delta t}_{i56} = [0.0050 \quad 0.0050 \quad 0.0050 \quad 0.1000 \quad 0.1000 \quad 0.1000]^T, (i = 1, 2, 3);$

- **Type II.1**: $\boldsymbol{\delta t}_{156} = [0.0050 \quad 0.0050 \quad 0.0050 \quad 0.1000 \quad 0.1000 \quad 0.1000]^T$, (limb 1 only);
- **Type III**: $\boldsymbol{\delta t}_{i23} = [0.0050 \quad 0.0050 \quad 0.0050 \quad 0.0000 \quad 0.0000 \quad 0.0000]^T, (i = 1, 2, 3)$;
- **Type III.1**: $\boldsymbol{\delta t}_{123} = [0.0050 \quad 0.0050 \quad 0.0050 \quad 0.0000 \quad 0.0000 \quad 0.0000]^T$, (limb 1 only).

Note that the first three elements represent orientational errors with the unit in radian; the last three elements represent positional error in centimeter.

Based on the numerical results, the position and orientation errors along each trajectory are shown in Fig. 7.10 and Fig. 7.11 respectively. As shown in Fig. 7.10, Type III and Type III.1 errors always have the most effects on the position error of the end-effector. This is because the position error contributed by the two types of errors needs to be magnified by the length from the end-effector origin to the error associated joints. Comparing to other types of errors, the magnified length for both Type III and Type III.1 errors are the largest. Therefore, Type III and Type III.1 errors dominate the position error of the end-effector. For the orientation error of the end-effector, it will be stable in the translations as shown in Fig. 7.11(a, b, c). This is because the error matrices associated with orientation (B in eqn. (7.4), B and E in eqn. (7.14), and E in eqn. (7.17)) will not change when the end-effector orientation keeps fixed, so that the error contributions to the end-effector orientation will not change based on equations (7.4), (7.14) and (7.17). When the end-effector orientation changes, the error matrices will have related changes, which will contribute to the orientation error of the end-effector, as shown in Fig. 7.11(d, e, f). By analyzing the numerical results, following conclusions are obtained:

- Error Type I: The maximal magnitude of orientational errors is 0.0247rad, which is 2.8480 times of the errors we assigned. The maximal magnitude of positional error is 0.2510cm, which is 1.4492 times as the assigned errors.

- Error Type II: The maximal magnitude of orientational errors is 0.0262rad, which is 3.0238 times as the errors we assigned. The maximal magnitude of positional errors is 0.2554cm, which is 1.4746 times of the assigned errors.

- Error Type III: The maximal magnitude of orientational error of end-effector is 0.0187rad, which is 2.1570 times as the errors we assigned. The maximal magnitude of positional error of the end-effector is 1.0295cm although we have not assigned position errors.

- For any type of the constraint error, a single limb error is much less critical than simultaneous errors in all three limbs. However, motion error of the end-effector resulting from simultaneous errors in all three limbs is less than three times of that from the error of a single limb. For example, the largest norm of the position error of Type I resulting from all three limbs is 1.4492 times of the assigned value while the corresponding error resulting from error in only one limb is 0.9512 times of the assigned value. This shows that the parallel kinematic structure of the manipulator can "average" out the errors in individual limbs though it has decoupled kinematic structure.

- Orientational errors of all the three types are about the same on the end-effector. For position of the end-effector, Type III errors dominate because these errors will be magnified by the distance $\|\boldsymbol{OO'}\|$ as shown in Section 7.4.2.

  In order to verify the effectiveness of the CL, we also evaluated the pose error under trajectories 4, 5 and 6 at the other two positions, i.e., $\boldsymbol{p}_2 = [30\ 30\ 30]^T$ and $\boldsymbol{p}_3 = [30\ 30\ 60]^T$. As a result, the largest relative positional error $\boldsymbol{\delta p}_i$ becomes

$$\begin{aligned} \boldsymbol{\delta p}_1 &= 1.0295/\|p_1\| \doteq 0.0099, \\ \boldsymbol{\delta p}_2 &= 0.5727/\|p_2\| \doteq 0.0110, \\ \boldsymbol{\delta p}_3 &= 0.6975/\|p_3\| \doteq 0.0095. \end{aligned} \tag{7.22}$$

  Hence, the CL is a suitable measure for average positional errors of the end-effector.

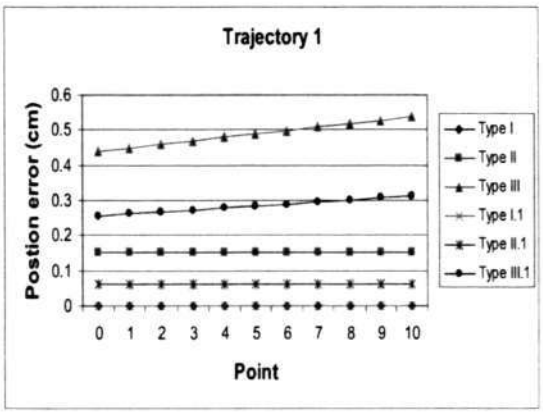

(a)

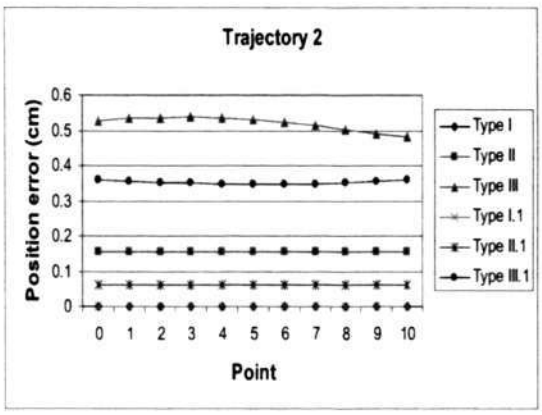

(b)

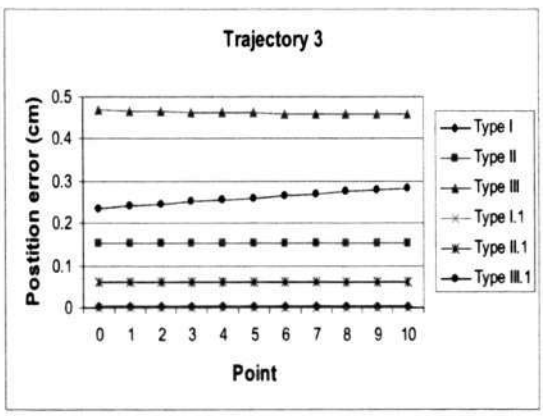

(c)

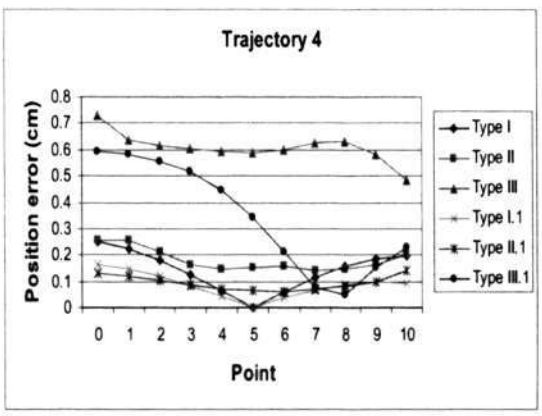

(d)

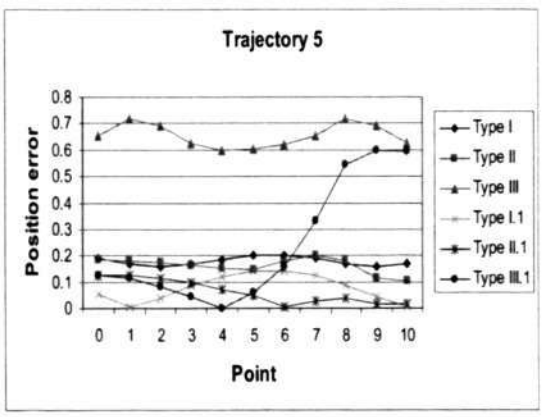

(e)

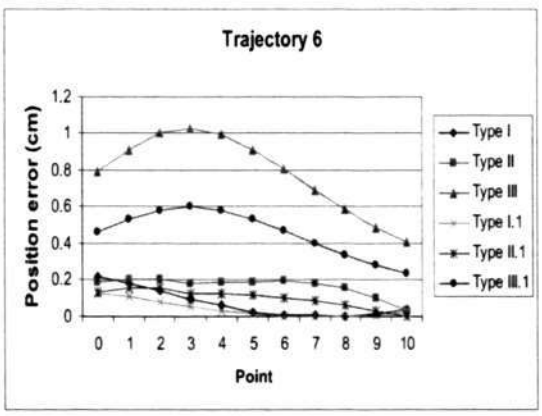

(f)

Figure 7.10: Position error of the task trajectories

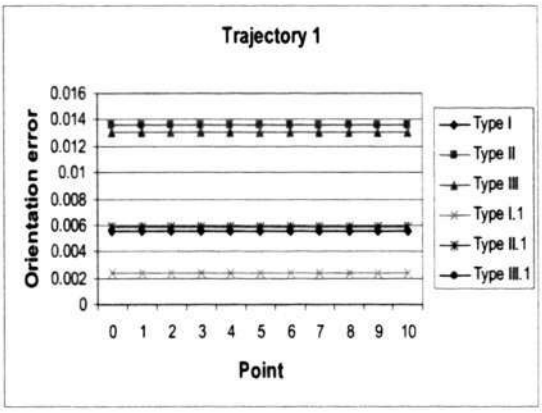

(a)

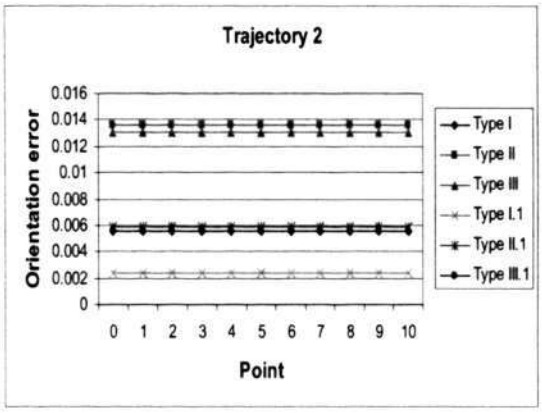

(b)

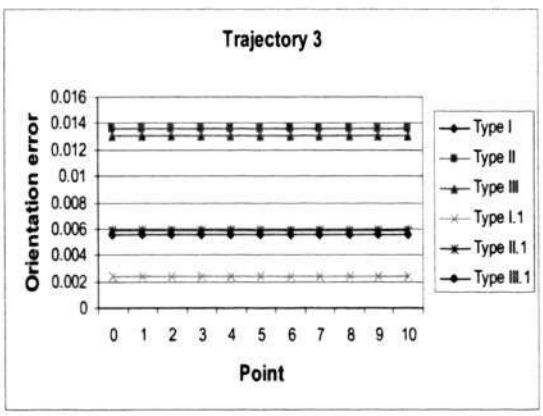

(c)

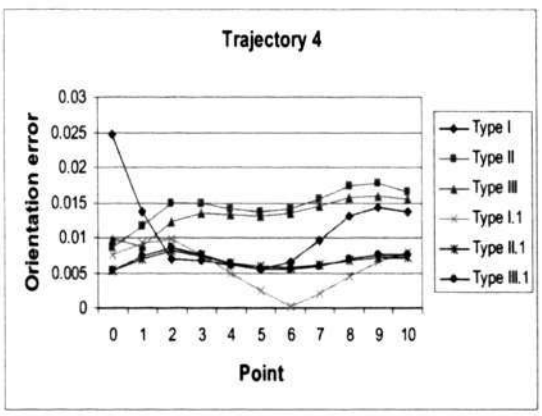

(d)

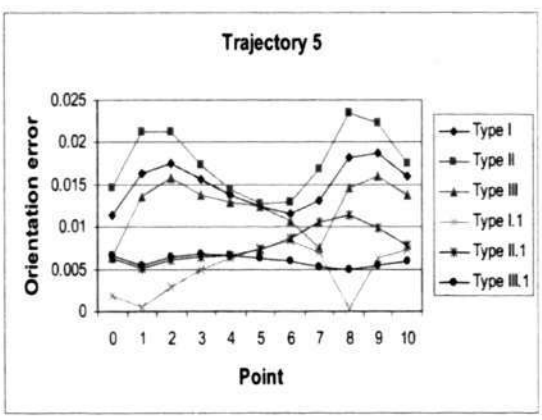

(e)

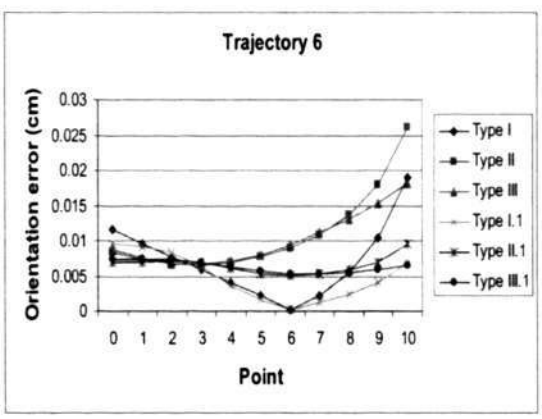

(f)

Figure 7.11: Orientation error of the task trajectories

Based on the above conclusions, four main guidelines are obtained as follows.

- The links related to Type III constraint error are suggested to assign tight tolerances in the manufacturing process. Caution has to be taken for these links during assembly.
- As the CL is configuration dependent, these points with small CL value in the position workspace are preferable to be chosen for certain tasks.
- Averaged by the CL, the position influences from different types of constraint errors are about the same magnitude. Thus identical weighting factors multiplied by the related CL are suggested to be assigned for the position parts of the constraint errors in calibration or compensation.
- As the orientation influences from different types of constraint errors are about the same magnitude, identical weighting factors can be assigned for the orientation parts of the constraint errors in calibration or compensation.

7.5 Summary

A procedure is proposed for analyzing the error effects on decoupling characteristics of PMs. This procedure includes error identification, error Jacobian analysis, motion error evaluation and comparison of motion from different types of constraint errors. A class of PMs with decoupled translation and rotation is employed as an example, which shows that different types of errors will have different effects on the decoupling characteristics of the end-effector motion. A characteristic length is defined as a measure of average positional errors of the end-effector for this class of PMs, and the dominating errors are obtained. Design guidelines are obtained. The result shows the feasibility of the evaluation procedure on decoupled motion PMs. This approach can also be used for PMs with lower mobility (less than six).

Chapter 8

Conclusions and Future Directions

In this thesis, I have studied the fundamental research issues of decoupled parallel manipulators including design approaches for structure synthesis, workspace optimization and constraint error evaluation, and modelings of singularity, kinematics and statics as shown in Fig. 8.1. In this chapter, the conclusions and main contributions are summarized, and the future research directions are then outlined.

8.1 Conclusions

Structure synthesis

The concept of group decoupling is introduced. Based on this concept, the decoupled parallel manipulators have been classified according to the end-effector motion. An idea of sharing sub-chain with only passive joints is disclosed. Based on this idea, a systematic approach is proposed for structure synthesis of 3-limb symmetrical 6-DOF PMs with 3-3 decoupled motion. A search space including limb serial chains with at least one zero-pitch wrench is developed based on the line geometry method. Two classes of 3-3 decoupled parallel manipulators are obtained, in which seven structures are new.

Kinematic models and singularity analysis

Kinematic modelling and singularity analysis are the basis of workspace evaluation, error

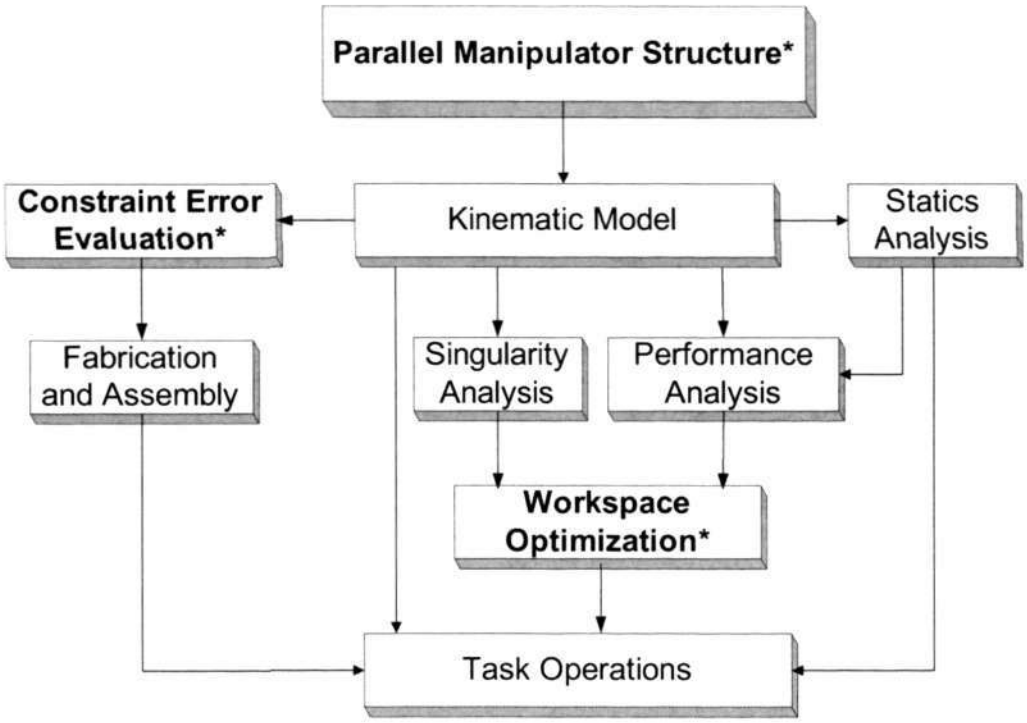

Figure 8.1: Kinematic design issues discussed in this thesis (*major contributions)

analysis and static investigation. The formulation of instantaneous kinematics shows that the decoupled motion properties can be directly identified by suitably choosing the reference frame and velocity representation method. As a result, the two manipulator Jacobian matrices (both inverse and forward Jacobian) of rank six can be converted into four Jacobian matrices of rank three for these 3-3 decoupled PMs. Due to decoupled motion, the kinematics analysis is also significantly simplified. As a result, closed-form solutions of both inverse and forward kinematics are obtained.

Workspace evaluation through finite-partition of $SE(3)$

A finite-partition approach for parametrical and proportional partition of the rigid motion group $SE(3)$ is introduced based on its topology, which is the product of $\mathbb{R}^3$ and $SO(3)$. The basis volume elements of $\mathbb{R}^3$ and $SO(3)$ are obtained. The product of two basis volume elements of $\mathbb{R}^3$ and $SO(3)$ respectively will produce a basis volume element of $SE(3)$. By this way, the integration of the complete 6-D workspace volume is transformed into the simple summation of the basis volume elements of $SE(3)$. Based on this finite-partition

method, two performance indices and three optimal points are defined in the complete 6-D workspace. Several algorithms for the dimension optimization and performance evaluation of the SA-PM and the 3RPPS-PM are developed to illustrate the effectiveness of the approach. The results show that the finite-partition approach is valid and the global properties of PMs can be objectively evaluated by these performance indices.

Statics and stiffness analysis

Both the static and stiffness models of two types of decoupled PMs are established. It is shown that the end-effector force/moment can be decoupled to some extent due to the decoupling motion structure. This will reduce the complexity and computation time for calculating the forces/moments and stiffness. The maximal generalized force at the GIP are obtained. The stiffness contours of both the SA-PM and the 3RPPS PM are obtained, which reveal the manipulator stiffness behavior in the workspace.

Constraint error evaluation

An approach for analyzing the constraint error effects on decoupling characteristics of PMs is proposed. Three basic types of constraint errors are identified. One example is used to illustrate the validity of this approach. As a result, the weight of each type of constraint error are obtained, and the dominating error has been found.

8.2 Contributions

This research work contributes towards the design methodology of decoupled PMs. This research work is important since more and more parallel manipulators are required for applications with high speed and high accuracy. To summarize, the contributions are:

Classification and structure synthesis of decoupled PMs

The classification of decoupled PMs is necessary and useful for reducing the complexity of structure synthesis since there is no generic method for synthesizing decoupled PMs. The idea for sharing sub-chain composed by only passive joints can also be applied for

synthesizing other decoupled PMs or the manipulators with redundant actuation. Due to the decoupled translation and rotation, the structure of SA-PM has high potential for micro or nano applications, such as fibre alignments. A flexure micro manipulator based on this structure has been designed [94]. With high stiffness in vertical direction, these 3P3S PMs are the suitable mechanisms for machining tasks with high payload in the vertical direction.

Workspace evaluation through finite-partition of $SE(3)$

The important function of the finite-partition approach is to makes the numerical computation of 6-D manipulator workspace possible. It is shown that various workspace measures such as workspace volume and the global condition index can be readily incorporated in the partition scheme. As the proposed finite-partition scheme can cope with any solid sphere or cube, it can be applied to not only $SE(3)$-related issues such as workspace analysis, path planing, sampling and control of robot manipulators but also other areas like computer graphics. Based on similar idea, other types of geometry, such as torus, can also be partitioned into a number of elements.

Constraint error evaluation

The approach for evaluating constraint errors of decoupled PMs can be used to objectively describe the importance of difficult design constraints, which provides the guidelines for fabrication, assembly and calibration. This approach can be applied for both decoupled PMs and PMs with lower mobility. It also serves as the preliminary study of machine errors, which is necessary for assigning reasonable tolerances for specific tasks.

8.3 Future Directions

The future direction of this project will include following issues:

1. General design methodology of decoupled PMs

A structure synthesis method for 3-3 decoupled 6-DOF PMs is proposed. However it is not

a general approach for synthesizing decoupled PMs. It is well accepted that structure synthesis is a big challenge, and a generic synthesis approach cannot be available. Although some approaches are available for certain PMs, there is no general design methodology for synthesizing a PM to fulfill some tasks optimally. For the structure design of decoupled PMs, new structure synthesis methods are required for other types of decoupled PMs. In addition, a generic design environment for PMs, including structure synthesis, dimension optimization, and performance evaluation, is required urgently, which will be very helpful for a designer to design a task based PM, or for a customer to select optimal ones.

2. Improvement on workspace computation

The proposed workspace evaluation algorithm based on the finite-partition approach of $SE(3)$ is computationally intensive, which will influence the accuracy of the results. Our results show that the computation time can be reduced by resorting to lessen the reachable workspace volume based on the manipulator structure properties. Another suitable method to this problem is to use parallel processing to increase the resolution of the workspace. This will need us to redesign the program structure, and recoding the algorithm with communications in multiple processors. In addition, code optimization will also be helpful to decrease the computation time.

3. Motion planning algorithm and control

The advantages of decoupling characteristics of PMs need to be investigated in the motion planning and control. The problems include that how fast the control algorithm can be realized, and how much the computation time can be reduced by the decoupling characteristics, and how to make use of the decoupling properties to realize the closed-loop control. Another interesting issue is: what is the the shortest path between two feature points of $SE(3)$, and how to find the path geometrically. The solution to this problem will be very helpful for trajectory planning and control.

4. Error bound for manufacturing with specific requirements

We have proposed an approach to evaluate the constraint error effects on the decoupling

characteristics. The next step is to define a reasonable measure, which should be an error bound, to judge the manipulator decoupling properties. The measure is used to protect the adaptability of the nominal kinematic models. A complete kinematic error model, including both constraint and non-constraint errors is also required. The mapping between the errors in joint (link) space and those of the end-effector is needed to formulated, which is useful to assign tolerances of each joint (link) with given accuracy requirements of task space, or to find the accuracy of the end-effector with given errors in the joint space. The results will also be helpful for calibration.

5. From rigid mechanisms to flexure mechanisms

Precision positioning devices having resolution of sub-microns to some nanometers have attracted many attention both from university scholars and from industry. The advantages of PMs, i.e., high stiffness and high accuracy, make them suitable candidates for precision positioning mechanism with flexure joints instead of rigid joints. Furthermore, the PM structure make it feasible to mount all actuators immediately on the base so as to reduce the weights of moving parts and increase the dynamic behavior. In addition, the decoupling properties are preferred to simplify the control. Therefore, the design of flexure mechanisms based on the newly designed PM structures is also an interesting and significant issue. Specially, based on the SA-PM proposed in this thesis, one flexure PM has been designed [94].

6. Potential applications of these decoupled PMs

The design and analysis of the two novel classes of 6-DOF decoupled PMs clearly show that these decoupled PMs are the best candidates for conquering the disadvantages of conventional PMs while keeping the advantages of general PMs, such as low moment of inertia, high speed, high acceleration, high accuracy and high stiffness. More over, the augmented advantages of these 3-3 decoupled PMs are as follows.

- Larger workspace due to the 3-limb design comparing with usual hexpod PMs.

- Energy efficient due to decoupled motion, so that different motion of end-effector is only controlled by certain actuators rather than the coordination of all actuators.
- Ease of motion planning and control because close-form solutions are obtained for both inverse and forward kinematics.

The limitations of the 6-DOF 3-3 decoupled PMs are as follows.

- There are many links and joints in the PMs with decoupled translation and rotation, so that the workspace of the end-effector is very small mainly due to leg interferences. Therefore, the PMs with decoupled translation and rotation are much applicable for micro- or nano- applications.
- Geometrical constraints for achieving decoupled motion are difficult to be realized in real applications. Therefore, in the initial design stage, careful consideration, such as assigning tight tolerances and making the CL small, needs to be taken for these critical constraints.

As to the application, these decoupled PMs are ideal for the fibre alignment since it is easy to set the position point of the fibre to prevent its movement when orientation of the fibre is optimized. Specially, the SA-PM can be used to firstly locate the positioning point of the fibre at the rotation centre, and then adjust the angular alignment to optimum. Due to the dextrous motion ability of these 6-DOF decoupled PMs, they are suitable for light machining tools for deburring, polishing, and grinding of curved surfaces. In addition, as the stiffness along vertical direction (or z-direction) of these 3P3S PMs is very high, they are very useful for precision assembly tasks of heavy parts. Other possible applications include: motion simulator for virtual reality, laser beam steering, and fast micro-manipulation.

Bibliography

[1] Hexapod-telescope. http://www.astro.ruhr-uni-bochum.de/astro/hpt/index.html.

[2] Six dof hexapod. http://biotsavart.tripod.com/hexapod.htm.

[3] K. Abdel-Malek and B. Paul. The dexterous solid angle for manipulators with a spherical wrist. In *Proceedings of the 23rd ASME Mechanisms Conference*, pages 341–350, Minneapolis, MN, 1994.

[4] S.K. Agrawal and B. Roth. Statics of in-parallel manipualator systems. *ASME Journal of Mechanical Design*, 114:564–568, 1992.

[5] R.I. Alizade, N.R. Tagiyev, and J. Duffy. A forward and reverse displacement analysis of a 6-dof in-parallel manipulator. *Mechanism and Machine Theory*, 29(1):115–124, 1994.

[6] J. Angeles. On twist and wrench generators and annihilators. In *Computer aided analysis of rigid and flexible mechanical systems*, pages 379–411. M. Pereira and J. Ambrosio (editors), Kluwer Academic Publishers, Netherlands, 1994.

[7] J. Angeles. *Fundamentals of Robotic Mechanical Systems: Theory, Methods and Algorithms*. Springer, 1997.

[8] M. Badescu and C. Mavroidis. New performance indices and workspace analysis of reconfigurable hyper-redundant robotic arms. *International Journal of Robotics Research*, 23(6):643–659, 2004.

[9] M. Badescu and C. Mavroidis. Workspace optimization of 3-legged upu and ups parallel platforms with joint constraints. *ASME Journal of Mechanical Design*, 126:291–300, March 2004.

[10] S. Bai, M.Y. Teo, W.S. Ng, and C. Sim. Workspace analysis of a parallel manipulator with one redundant dof for skull-base surgery. In *Proceedings of IEEE/RSJ International Conference on Intelligent Robots and Systems*, pages 1694–1699, Maui, Hawaii, USA, 2001.

[11] L. Baron and J. Angeles. The direct kinematics of parallel manipulators under joint-sensor redundancy. *IEEE Transactions on Robotics and Automation*, 16(1):12–19, 2000.

[12] F. Bulca, J. Angeles, and P.J. Zsombor-Murray. On the workspace determination of spherical serial and platform mechanisms. *Mechanism and Machine Theory*, 34:497–512, 1999.

[13] M. Sorli N. Zhmud C. Ferraresi, S. Pastorelli. Static and dynamic behavior of a high stiffness stewart platform-based force/torque sensor. *Journal of Robotic Systems*, 12(12):883–893, 1995.

[14] M. Ceccarelli and G. Carbone. A stiffness analysis for capaman (Cassino Parallel Manipulator). *Mechanism and Machine Theory*, 37(1):427–439, 2002.

[15] G.S. Chirikjian and A.B. Kyatkin. *Engineering Applications of Noncommutative Harmonic Analysis*. CRC Press LLC, USA, 2001.

[16] Y. Chiu and M. Perng. Forward kinematics of a general fully parallel manipulator with auxiliary sensors. *International Journal of Robotics Research*, 20(5):401–414, 2001.

[17] R. Clavel and S.A. Sogeva. Device for the movement and positioning of an element in space, US patent, US4976582. 1990.

[18] C. Collins. On the duality of twist/wrench in serial and parallel chain robot manipulators. In *Proceedings of IEEE Conference on Robotics and Automation*, pages 526–531, Nagoya, Aichi, Japan, 1995.

[19] N.G. Dagalakis, J.S. Albus, B.L. Wang, J. Unger, and J.D. Lee. Stiffness study of a parallel link robot crane for shipbuilding applications. *ASME Journal of Offshore Mechanics and Arctic Engineering*, (111):183–193, 1989.

[20] Y. Fang and L.W. Tsai. Structure synthesis of a class of 4-dof and 5-dof parallel manipulators with identical limb structures. *International Journal of Robotics Research*, 21(9), 2002.

[21] Y. Fang and L.W. Tsai. Structure synthesis of a class of 3-dof rotational parallel manipulators. *IEEE Transactions on Robotics and Automation*, 20(1):117–121, 2004.

[22] Haptic Interfaces for Spatial Learning. http://www.colorado.edu/ATconference/PaoLawrenceKramer_files/frame.htm.

[23] Y. Gao. *Decomposable closed-form inverse kinematics for reconfigurable robots using product-of-exponentials formula.* M.Eng. Thesis, School of Mechanical and Production Engineering, Nanyang Technological University, Singapore, 2000.

[24] Peter B. Goldsmith. Kinematics and stiffness of a symmetrical 3-upu translational parallel manipulator. In *Proceedings of IEEE Conference on Robotics and Automation*, pages 4102–4107, Washington, DC, USA, May 2002.

[25] C. Gosselin. Determination of the workspace of 6-DOF parallel manipulators. *ASME Journal of Mechanical Design*, 112:331–336, 1990.

[26] C. Gosselin and J. Angeles. Singularity analysis of closed-loop kinematic chains. *IEEE Journal on Robotics and Automation*, 6(3):281–290, 1990.

[27] C. Gosselin and J. Angeles. A global performance index for the kinematic optimization of robotic manipulators. *ASME Journal of Mechanical Design*, 113:220–226, 1991.

[28] C. Gosselin, J. Sefrioui, and M. Richard. On the direct kinematics of spherical three-degree-of-freedom parallel manipulators of general architecture. *ASME Journal of Mechanical Design*, 116:594–598, 1994.

[29] C.M. Gosselin. Stiffness mapping for parallel manipulators. *IEEE Transactions on Robotics and Automation*, 6(3):377–382, 1990.

[30] C.M. Gosselin, E.Pierre, and M.Gagne. On the development of the agile eye. *IEEE Transactions on Robotics and Automation*, 3(4):29–37, 1996.

[31] C.M. Gosselin and D. Zhang. Stiffness analysis of parallel mechanisms using a lumped medel. *International Journal of Robotics and Automation*, 17(1):17–27, 2002.

[32] R. Di Gregorio. Kinematics of a new spherical parallel manipulator with three equal legs: 3-URC wrist. *Journal of Robotic Systems*, 18:213–219, 2001.

[33] R. Di Gregorio. A new parallel wrist using only revolute pairs: the 3-RUU wrist. *Robotica*, 19:305–309, 2001.

[34] R. Di Gregorio and V. Parenti-Castelli. Kinematics of a six-dof fixation device for long-bone fracture reduction. *Journal of Robotic Systems*, 18(12):715–722, 2001.

[35] R. Di Gregorio and V. Parenti-Castelli. Geometric error effects on the performances of a parallel wrist. In *Proceedings of 3rd Chemnitz Parallel Kinematics Seminar*, pages 1011–1024, Chemnitz, Germany, April 23–25 2002.

[36] M. Griffis and J. Duffy. Global stiffness modeling of a class of simple compliant couplings. *Mechanism and Machine Theory*, 28(2):207–224, 1993.

[37] J.M. Hervé. The Lie group of rigid body displacements, a fundamental tool for mechanism design. *Mechanism and Machine Theory*, 34(8):719–730, 1991.

[38] J.M. Hervé and F. Sparacino. Structural synthesis of parallel robots generating spatial translation. In *Proceedings of the Fifth IEEE International Conference on Advanced Robotics*, pages 808–813, Pisa, Italy, 1991.

[39] Parallel Kinematics. http://www.iwu.fraunhofer.de/english/service/projects/parallel/.

[40] Urane SX. http://www.lirmm.fr/rdc/pm/uranesx.html.

[41] S. Huang and J.M. Schimmels. Minimal realizations of spatial stiffnesses with parallel or serial mechanisms having concurrent axes. *Journal of Robotics Systems*, 18(3):135–146, 2001.

[42] T. Huang, X. Zhao, and D.J. Whitehouse. Stiffness estimation of a tripod-based parallel kinematic machine. *IEEE Transactions on Robotics and Automation*, 18(1):50–58, 2002.

[43] Z. Huang and Q.C. Li. General methodology for type synthesis of symmetrical lower-mobility parallel manipulators and several novel manipulators. *International Journal of Robotics Research*, 21(2):131–145, 2002.

[44] Z. Huang and Q.C. Li. Type synthesis of symmetrical lower-mobility parallel manipulators using the constraint-synthesis method. *International Journal of Robotics Research*, 22(1):59–79, 2003.

[45] K.H. Hunt. *Kinematic Geometry of Mechanisms*. Oxford University Press, UK, 1978.

[46] M.L. Husty. An algorithm for solving the direct kinematics of general Stewart-Gough platforms. *Mechanism and Machine Theory*, 31(4):365–379, 1996.

[47] INDEX. http://www.index werke.de/en/index/produkte/verticalline/v100/.

[48] C. Innocenti and V. Parenti-Castelli. Direct position analysis of the stewart platform mechanism. *Mechanism and Machine Theory*, 25(6):611–621, 1990.

[49] C. Innocenti and V. Parenti-Castelli. Direct kinematics of the 6-4 fully parallel manipulator with position and orientation uncoupled. In *Proceedings of European Robotics and Intelligent Systems Conference*, Corfu, June 23–28 1991.

[50] Q. Jin and T. Yang. Synthesis and analysis of a group of 3-degree-of-freedom partially decoupled parallel manipulators. *ASME Journal of Mechanical Design*, 126:301–306, 2004.

[51] Y. Jin and I.M. Chen. On the performance of a class of parallel manipulators with decoupled kinematic structure with stringent geometric constraints. In *Proceedings of International Workshop on Computational Kinematics (CK2005)*, Cassino, Italy, May 4-6 2005.

[52] Y. Jin and I.M. Chen. Effects of constraint errors on parallel manipulators with decoupled motion. *Mechanism and Machine Theory*, 41:912–928, 2006.

[53] Y. Jin, I.M. Chen, and G. Yang. Kinematics analysis of a 6-dof selectively actuated parallel manipulator. In *Proceedings of IEEE Conference on Robotics, Automation and Mechatronics*, pages 231–236, Singapore, Dec. 1–3 2004.

[54] Y. Jin, I.M. Chen, and G. Yang. Mobility and singularity analysis of a selectively actuated parallel mechanism. In *Proceedings of 15th CISM-IFToMM Symposium Robot Design, Dynamics and Control (ROMANSY)*, pages 359–368, Montreal, Canada, June 14–18 2004.

[55] Y. Jin, I.M. Chen, and G. Yang. Structure synthesis and singularity analysis of a parallel manipulator based on selective actuation. In *Proceedings of IEEE Conference on Robotics and Automation*, pages 4533–4538, New Orleans, LA, USA, April 26–May 1 2004.

[56] Y. Jin, I.M. Chen, and G. Yang. Finite-partition of $SE(3)$ and its applications on workspace optimization of parallel manipulators. In *Proceedings of IEEE/RSJ International Conference on Intelligent Robots and Systems*, pages 2133–2138, Beijing, China, 2006.

[57] Y. Jin, I.M. Chen, and G. Yang. Kinematic design of a 6-dof parallel manipulator with decoupled translation and rotation. *IEEE Transactions on Robotics*, 22(3):545–561, 2006.

[58] M. Karouia and J.M. Hervé. A three-dof tripod for generating spherical rotation. In *Proceedings of Advances in Robot Kinematics*, pages 395–402. London: Kluwer Academic Publishers, 2000.

[59] D.I. Kim, W.K. Chung, and Y. Youm. Geometrical approach for the workspace of 6-dof parallel manipulators. In *Proceedings of IEEE Conference on Robotics and Automation*, pages 2986–2991, Albuquerque, New Mexico, April 1997.

[60] X. Kong and C.M. Gosselin. Generation of parallel manipulators with three translational degrees of freedom based on screw theory. In *Proceedings of 2001 CCToMM Symposium on Mechanisms, Machines and Mechatronics*, Saint-Hubert, Montreal, Canada, 2001.

[61] X. Kong and C.M. Gosselin. A class of 3-dof translational parallel manipulators with linear input-output equations. In *Proceedings of the Workshop on Fundamental Issues and Future Research Directions for Parallel Mechanisms and Manipulators*, pages 25–32, Quebec City, Quebec, Canada, 2002.

[62] X. Kong and C.M. Gosselin. Type synthesis of 3-dof spherical parallel manipulators based on screw theory. *ASME Journal of Mechanical Design*, 126(1):101–108, 2004.

[63] X. Kong and C.M. Gosselin. Type synthesis of 3t1r 4-dof parallel manipulators based on screw theory. *IEEE Transactions on Robotics and Automation*, 20(2):181–190, 2004.

[64] X. Kong and C.M. Gosselin. Type synthesis of 4-dof sp-equivalent parallel manipulators: A virtual-chain approach. In *Proceedings of International Workshop on Computational Kinematics (CK2005)*, Cassino, Italy, May 4-6 2005.

[65] V. Kumar. Characterization of worspaces of parallel manipulators. *ASME Journal of Mechanical Design*, 114:368–375, 1992.

[66] V. Kumar. Instantaneous kinematics of parallel chain robotic mechanisms. *ASME Journal of Mechanical Design*, 114:349–358, 1992.

[67] J.P. Lallemand, A. Goudali, and S. Zeghloul. The 6-Dof 2-Delta parallel robot. *Robotica*, 15:407–416, 1997.

[68] J.C. Latombe. *Robot Motion Planning*. Kluwer Academic Publishers, MA, USA, 1991.

[69] J. Lee, J. Duffy, and K.H. Hunt. A practical quality index based on the octahedral manipulator. *International Journal of Robotics Research*, 17(10):1081–1090, 1998.

[70] J-H. Lee and K-S. Hong. Kinematic optimal design of a paramill: a multi-sp device. *Journal of Robotic Systems*, 21(6):345–359, 2004.

[71] M.K. Lee and K.W. Park. Workspace and singularity analysis of a double parallel manipulator. *IEEE/ASME Transactions on Mechatronics*, 5(4):367–375, 2000.

[72] Q. Li, Z. Huang, and J.M. Hervé. Type synthesis of 3r2t 5-dof parallel mechanisms using the lie group of displacements. *IEEE Transactions on Robotics and Automation*, 20(2):173–180, 2004.

[73] G. Liu, Y. Lou, and Z. Li. Singularities of parallel manipulators: A geometric treatment. *IEEE Transactions on Robotics and Automation*, 19(4):579–594, 2003.

[74] X.J. Liu, Z.L. Jin, and F. Gao. Optimum design of 3-dof spherical parallel manipulators with respect to the conditioning and stiffness indices. *Mechanism and Machine Theory*, 35:1257–1267, 2000.

[75] Y. Lou, G. Liu, J. Xu, and Z. Li. A general approach for optimal kinematic design of parallel manipulators. In *Proceedings of IEEE Conference on Robotics and Automation*, pages 3659–3664, New Orleans, LA, USA, April 26–May 1 2004.

[76] A.K. Low. *Design and development of 2-DOF module and calibration fixture for modular robots.* Final year project, School of Meachanical and Production Engineering, Nanyang Technological University, Singapore, 2002.

[77] O. Masory and J. Wang. Workspace evalution of stewart platform. In *Proceedings of ASME Conference on Robotics, Spatial Mechanisms, and Mechanical Systems*, pages 337–346, De-Vol. 45, ASME Press, New York 1992.

[78] J. Meng and Z. Li. A general approach for accuracy analysis of parallel manipulators with joint clearance. In *Proceedings of IEEE/RSJ International Conference on Intelligent Robots and Systems*, pages 790–795, Edmonton, Alberta, Canada, Aug.2–6 2005.

[79] J.P. Merlet. Singular configurations of parallel manipulators and grassman geometry. *International Journal of Robotics Research*, 8(5):45–56, 1989.

[80] J.P. Merlet. Efficient estimation of the extremal articular forces of a parallel manipulator in a translation workspace. In *Proceedings of IEEE Conference on Robotics and Automation*, pages 1982–1987, Leuven, Belgium, May 1998.

[81] J.P. Merlet. *Parallel Robots.* Kluwer Academic Publishers, Netherlands, 2000.

[82] J.P. Merlet. Solving the forward kinematics of a gough-type parallel manipulator with interval analysis. *International Journal of Robotics Research*, 23(3):221–235, 2004.

[83] J.P. Merlet, C.M. Gosselin, and N. Mouly. Workspaces of planar parallel manipulators. *Mechanism and Machine Theory*, 33(1):7–20, 1998.

[84] M.G. Mohammed and J. Duffy. A direct determination of the instantaneous kinematics of fully parallel manipulators. *ASME Journal of Mechanisms, Transmission, and Automation in Design*, 107:226–229, 1985.

[85] B. Monsarrat and C.M. Gosselin. Workspace analysis and optimal design of a 3-leg 6-dof parallel platform mechanism. *IEEE Transactions on Robotics and Automation*, 19(6):954–966, 2003.

[86] B.W. Mooring, Z.S. Roth, and M.R. Driels. *Fundamentals of Manipulator Calibration*. John Wiley and Sons, 1991.

[87] R. Murray, Z. Li, and S.S. Sastry. *A Mathematical Introduction to Robotic Manipulation*. CRC Press, USA, 1994.

[88] K. Neumann. Robot, US patent, US4732525. 1988.

[89] L. Notash and R.P. Podhorodeski. On the forward displacement problem of three-branch parallel manipulators. *Mechanism and Machine Theory*, 30(3):391–404, 1995.

[90] V. Parenti-Castelli and R. Di Gregorio. Influence of manufacturing errors on the kinematic performances of the 3-upu parallel mechanism. In *Proceedings of 2rd Chemnitz Parallel Kinematics Seminar*, pages 85–100, Chemnitz, Germany, April 12–13 2000.

[91] F.C. Park and J.M. Kim. Singularity analysis of closed kinematic chains. *ASME Journal of Mechanical Design*, 121(1):32–38, 1999.

[92] F.C. Park and B. Ravani. Bézier curves on Riemannian manifolds and Lie Groups with kinematics applications. *ASME Journal of Mechanical Design*, 117(1):36–40, 1995.

[93] R.P. Paul. *Robot Manipulators: Mathematics, Programming, and Control*. MIT Press, Cambridge, MA, 1981.

[94] H.H. Pham. *Selective-Actuation Micro-Positioning Systems Based on Flexure Parallel Mechanisms.* PhD thesis, Nanyang Technological Unversity, Singapore, 2005.

[95] M. Raghavan. The stewart platform of general geometry has 40 configurations. *ASME Journal of Mechanical Design*, 115:277–282, 1993.

[96] R. Ranganath, P.S. Nair, T.S. Mruthyunjaya, and A. Ghosal. Studies on a stewart platform based force-torque sensor in a near-singular configuration. In *Proceedings of the 11th World Congress in Mechanism and Machine Science*, Tianjin, China, 2004.

[97] J.K. Salisbury and J.J. Craig. Articulated hands: force control and kinematics issues. *International Journal of Robotics Research*, 1(1):4–12, 1982.

[98] J.H. Shim, D.S. Kwon, and H.S. Cho. Kinematic analysis and design of a six D.O.F. 3-PRPS in-parallel manipulator. *Robotica*, 17:269–281, 1999.

[99] D. Stewart. A platform with six degrees of freedom. In *Proceedings of Institution of Mechanical Engineers*, volume 180 (15), pages 371–386, 1965.

[100] L.J. Stocco, S.E. Sacudean, and F. Sassani. On the use of scaling matrices for task-specific robot design. *IEEE Transactions on Robotics and Automation*, 15(5):958–965, 1999.

[101] M. Tandirci, J. Angeles, and F. Ranjbaran. The characteristic point and the characteristic length of robotic manipulators. In *Proceedings of ASME 22nd Biennial conference on Robotics, Spatial Mechanisms, and Mechanical Systems*, pages 203–208, Scottsdale, AZ, Sept. 13–16 1992.

[102] L.W. Tsai. *Robot Analysis.* John Wiley & Sons, New York, 1999.

[103] L.W. Tsai. *Mechanism Design: Enumeration of Kinematic Structures According to Function.* CRC Press, USA, 2001.

[104] L.W. Tsai and S. Joshi. Kinematics and optimization of a spatial 3-UPU parallel manipulator. *ASME Journal of Mechanical Design*, 122:439–446, 2000.

[105] L.W. Tsai, G.C. Walsh, and R.E. Stamper. Kinematics and workspace of a novel three dof translational platform. Technical report, University of Maryland, USA, 1996.

[106] J. Unger, N.G. Dagalakis, T. Tsai, and J.D. Lee. Optimum stiffness study for a parallel link robot crane under horizontal force. In *Robotics and Manufacturing (edited by Jamshidi, Luh, Seraji and Starr), ASME Press*, pages 1037–1046, 1988.

[107] C.W. Wampler, J.M. Hollerbach, and T. Arai. An implicit loop method for kinematic calibration and its application to closed-chain mechanisms. *IEEE Transactions on Robotics and Automation*, 11(5):710–724, 1995.

[108] L.T. Wang and C.C. Chen. On the numerical kinematic analysis of general parallel robotic manipulators. *IEEE Transactions on Robotics and Automation*, 9(3):272–285, 1993.

[109] L.T. Wang and J. Hsieh. Extreme reaches and reachable workspace analysis of general parallel robotic manipulators. *Journal of Robotic Systems*, 15(3):145–159, 1998.

[110] G. Yang, I.M. Chen, W. Chen, and W. Lin. Kinematic design of a six-dof parallel-kinematics machine with decoupled-motion architecture. *IEEE Transactions on Robotics and Automation*, 20(5):876–884, 2004.

[111] G. Yang, I.M. Chen, W.K. Lim, and J. Angeles. Singularity analysis of three-legged parallel robots based on passive joint velocities. *IEEE Transactions on Robotics and Automation*, 17(4):413–422, 2001.

[112] G. Yang, I.M. Chen, W.K. Lim, and S.H. Yeo. Kinematic design of modualr reconfigurable in-parallel robots. *Autonomous Robots*, 10(1):83–89, 2001.

[113] G. Yang, E. Ho, W. Lin, and I.M. Chen. A differential geometry approach for the workspace analysis of spherical parallel manipulators. In *Proceedings of the 11th World Congress in Mechanism and Machine Science*, pages 2060–2065, Tianjin, China, 2004.

[114] J. Yang and Z. Geng. Closed form forward kinematics solution to a class of hexapod robots. *IEEE Transactions on Robotics and Automation*, 14(3):503–508, 1998.

[115] I. Zabalza, J. Ros, J.J. Gil, J.M. Pintor, and J.M. Jimenez. Tri-scott.a new kinematic structure for a 6-dof decoupled parallel manipulator. In *Proceedings of the Workshop on Fundamental Issues and Future Research Directions for Parallel Mechanisms and Manipulators*, pages 12–15, Quebec City, Quebec, Canada, 2002.

[116] H. Zhuang. Self-calibration of parallel mechanisms with a case study on stewart platform. *IEEE Transactions on Robotics and Automation*, 13(3):387–397, 1997.